2012

Nonlinear modeling and h-infinity model reference control of pneumatic suspension system

Jia Wang
Iowa State University

Nonlinear modeling and h-infinity model reference control of pneumatic suspension system

by

Jia Wang

A thesis submitted to the graduate faculty

in partial fulfillment of the requirements for the degree of

DOCTOR OF PHILOSOPHY

Major: Mechanical Engineering

Program of Study Committee:

Atul G. Kelkar, Major Professor

Jerald M. Vogel

Qinze Zou

Greg R. Luecke

Gap-Yong Kim

Iowa State University

Ames, Iowa

2012

DEDICATION

I would like to dedicate this thesis to my wife Hui Wang and to my son Terry T. Wang for their unlimited support and love during my graduate study. Hui's words of encouragement often help me to relieve the stress and to regenerate the hope for completing my graduate study.

I would also like to thank my father Zhiyuan Wang, my mother Zhengqun Han, my father-in-law Tingfa Wang, and my mother-in-law, Lihua Zhu. I appreciate them for their great support during the writing of this thesis.

TABLE OF CONTENTS

LIST OF TABLES vii

LIST OF FIGURES viii

ACKNOWLEDGEMENTS xiii

ABSTRACT xiv

CHAPTER 1. Introduction 1

1.1 Background of Automotive Suspension System 1

1.1.1 Historical Perspective 1

1.2 Motivation 2

1.2.1 Advantages of the Pneumatic Suspension System 3

1.2.2 Control Considerations in Suspension 4

1.2.3 Limitations of the State-of-the-Art Vibration Isolation Systems 9

1.2.4 Proposed Pneumatic Suspension System 10

1.2.5 Modeling of Pneumatic Suspension Systems 10

1.3 Outline of the Thesis 14

CHAPTER 2. Static and Dynamic Characteristics of the Pneumatic Suspension Systems 16

2.1 Concepts of the Air Spring 16

2.1.1 Isothermal Process 16

2.1.2 Adiabatic Process 17

2.1.3 Polytropic Process 17

2.1.4 Effective Area 18

2.2 Static Stiffness of the Air Spring 21

2.2.1 Static Stiffness of the Air Spring for Isothermal Process 21
2.2.2 Static Stiffness of the Air Spring for Adiabatic Process 22
2.2.3 Static Stiffness of the Air Spring for Polytropic Process 23
2.2.4 Summary of the Air Spring Static Stiffness Analysis 23
2.3 Dynamic Stiffness of the Air Spring 24
2.4 Summary 29

CHAPTER 3. Nonlinear Modeling of the Pneumatic Suspension System . . 31

3.1 Nonlinear Modeling 31
3.2 Validation of the Nonlinear Model for Pneumatic Suspension System 38
3.2.1 Results for K_{cr} 39
3.2.2 Results for K_{amp} 40
3.3 Linearized Model of the Pneumatic Suspension System 45
3.4 Summary 47

CHAPTER 4. Experimental Set-up and System Identification 50

4.1 Introduction 50
4.2 Laboratory Facility and Experimental Testing 50
4.2.1 Experimental Test Rig 50
4.2.2 System Identification 53
4.2.3 System Identification Test Results 54
4.3 Simple Analytical Model of the Pneumatic Suspension System 58
4.4 Verification of the System-ID Models 62

CHAPTER 5. H-Infinity Controller Design for Pneumatic Suspension System 64

5.1 H-Infinity Robust Controller Design 64
5.1.1 Determination of Nominal Model G_n and Uncertainties 68
5.1.2 Determination of Weighting Function $W_1(s)$ 69
5.1.3 Determination of Weighting Function $W_2(s)$ 72
5.1.4 Determination of G_d 74
5.2 H-Infinity Controller Performance 79

5.2.1 Frequency Response Analysis 79
5.2.2 Transient Response Analysis 80
5.2.3 Summary 80

CHAPTER 6. Model-Reference Sliding Mode Control 82

6.1 Fundamentals of Sliding Mode Control 83
6.1.1 Sliding Surface 83
6.1.2 Sliding Mode Condition 84
6.2 State Space Representation of the Suspension System and Its Reference Model 84
6.3 Error Dynamics and Sliding Surface Design 86
6.4 Simulation Study about Reference Tracking Performances 89
6.4.1 Sutdy on the Effects of m 90
6.4.2 Study on the Effects of ρ 91
6.4.3 Study on the Effects of ϕ 93
6.4.4 Simulation Study on Multiple Stiffness Conditions 94
6.5 Summary 95

CHAPTER 7. Experimental Validation of Controller Designs 97

7.1 Determination of Mapping Functions between V and C 98
7.2 Closed-Loop Analysis of the Nonlinear Pneumatic Suspension System 101
7.3 Experimental Validation 103
7.3.1 Vibration Isolation Performance and Controller Bandwidth 107

CHAPTER 8. Conclusions and Future Work 112

APPENDIX A. Simulink Diagram for Nonlinear Model of the Pneumatic Suspension System 114

APPENDIX B. RMS Values of the Pneumatic Suspension System for Multiple Gds 115

APPENDIX C. Simulink Diagram of the Sliding Mode Reference Control . . 116

APPENDIX D. Summary of Fitting Functions: V = f(C) 117

APPENDIX E. Simulink Diagram for Sliding Mode Reference H infinity Control:Part A 118

APPENDIX F. Simulink Diagram for Sliding Mode Reference H infinity Control: Part B 119

BIBLIOGRAPHY 120

LIST OF TABLES

Table 2.1 Initial Conditions for Static Test 18

Table 2.2 Parameter Values for Calculating Static Stiffness of Air Spring 24

Table 2.3 Theoretical Stiffness Vs Experimental Stiffness 24

Table 3.1 Parameter Values for Nonlinear Model Simulation 40

Table 3.2 Summary of Adjusting Parameter Values for K_{amp} 40

Table 5.1 Parameters of Sinusoidal Excitations for H-Infinity Control 74

Table 5.2 Summary of Step Response Results 76

Table 6.1 Parameters of Sinusoidal Excitations for Sliding Mode Control 90

Table 7.1 Summary of Functions $V = f(t)$, $K_{cr} = g(V)$, and $K_{cr} = h(t)$ 102

Table 7.2 Parameters for Sinusoidal Excitations in Experiment 104

Table 7.3 Coefficients of Experimental Test 111

LIST OF FIGURES

Figure 1.1 Plots for Passive Suspension System 5

Figure 1.2 Fully Active Suspension 6

Figure 1.3 Bose Ride System and Its Performance (http://www.bose.com) 7

Figure 1.4 Semi-Active Suspension 8

Figure 1.5 Transmissibility Plots for Sprung Mass 9

Figure 1.6 Diagram of Proposed Pneumatic Suspension System (Courtesy of IVS) 11

Figure 1.7 Pneumatic Isolator Suspension System-Case 1 (Erin, C. and Wilson, B.) 12

Figure 1.8 Pneumatic Isolator Suspension System-Case 2 (Quaglia, G. and Guala, A.) 13

Figure 2.1 Effective Area Vs Deformation 19

Figure 2.2 Fitted Functions $A_{eff}=f(x_r)$ 20

Figure 2.3 Static Stiffness (P_{s0}=71.2 psi) 24

Figure 2.4 Force Vs Deformation (0.15 inch Sinusoidal): Part 1 25

Figure 2.5 Force Vs Deformation (0.15 inch Sinusoidal): Part 2 25

Figure 2.6 Force Vs Deformation (0.3 inch Sinusoidal): Part 1 26

Figure 2.7 Force Vs Deformation (0.3 inch Sinusoidal): Part 2 26

Figure 2.8 Force Vs Deformation (0.5 inch Sinusoidal): Part 1 27

Figure 2.9 Force Vs Deformation (0.5 inch Sinusoidal): Part 2 27

Figure 2.10 Dynamic Stiffnesses for Various Excitation Amplitudes 28

Figure 2.11 Dynamic Stiffnesses for Various Excitations: Part 1 28

Figure 2.12 Dynamic Stiffnesses for Various Excitations: Part 2 29

Figure 2.13 Static Stiffness Values with P_{s0}=84.2 psi 30

Figure 3.1 Diagram of a Control Volume 32
Figure 3.2 Diagram of Pipe Flow 34
Figure 3.3 Flow Chart of Nonlinear Model Simulation 39
Figure 3.4 Simulation Vs Experiment for 0.15 inch: 7 rad/s and 10 rad/s 41
Figure 3.5 Simulation Vs Experiment for 0.15 inch: 15 rad/s and 30 rad/s 41
Figure 3.6 Simulation Vs Experiment for 0.3 inch: 7 rad/s and 10 rad/s 42
Figure 3.7 Simulation Vs Experiment for 0.3 inch: 15 rad/s and 30 rad/s 42
Figure 3.8 Simulation Vs Experiment for 0.5 inch: 7 rad/s and 10 rad/s 43
Figure 3.9 Simulation Vs Experiment for 0.5 inch: 15 rad/s and 30 rad/s 43
Figure 3.10 Kcr Vs Orifice Voltage for 0.15 inch 44
Figure 3.11 Kcr Vs Orifice Voltage for 0.3 inch 44
Figure 3.12 Kcr Vs Orifice Voltage for 0.5 inch 45
Figure 3.13 Stiffness at 0.15 inch, 6 volt and Kcr=1.8 47
Figure 3.14 Stiffness at 0.3 inch, 7 volt and Kcr=2.5 47
Figure 3.15 Stiffness at 0.5 inch, 8 volt and Kcr=2.3 48
Figure 3.16 Bode Plots (Simulation Vs Experiment) 48

Figure 4.1 Pneumatic Suspension Test Rig 51
Figure 4.2 Pneumatic Suspension Shaker 51
Figure 4.3 Stanford Spectrum Analyzer 53
Figure 4.4 1105 Dspace Board 53
Figure 4.5 Bode Plots for Various Orifice Voltages (0.2 inch) 56
Figure 4.6 Bode Plots for Various Orifice Voltages (0.4 inch) 56
Figure 4.7 Bode Plots for Various Orifice Voltages (0.6 inch) 56
Figure 4.8 Bode Plots for Various Disturbance Amplitudes (6 volt) 57
Figure 4.9 Bode Plots for Various Disturbance Amplitudes (7 volt) 57
Figure 4.10 Bode Plots for Various Disturbance Amplitudes (8 volt) 57
Figure 4.11 Natural Frequencies of System-ID Models 59
Figure 4.12 Damping Ratios of System-ID Models 59

Figure 4.13 Schematics of the Pneumatic Suspension System 60
Figure 4.14 Step Responses (Experiment Vs Simulation): Part 1 63
Figure 4.15 Step Responses (Experiment Vs Simulation): Part 2 63
Figure 4.16 Sinusoidal Responses (Experiment Vs Simulation) 63

Figure 5.1 Feedback Control System 65
Figure 5.2 Generalized Plant and P-K Configuration (Skogestad, S and Postlethwaite, 2005) 67
Figure 5.3 Magnitude Plots of Experimental and System-ID Models 70
Figure 5.4 Nominal Model and Boundary Models 70
Figure 5.5 Feedback Control Diagram with Multiplicative Uncertainty (Skogestad, S and Postlethwaite, 2005) 71
Figure 5.6 Step Response Plots for the Weighting Functions with Various Orders 73
Figure 5.7 Step Response Plots for the Weighting Functions with Multiple M and A Values 73
Figure 5.8 Optimization Results 73
Figure 5.9 Relative Velocity for Multiple Sinusoidal Excitations 75
Figure 5.10 Damping Force for Multiple Excitations and Orifice Voltages 75
Figure 5.11 Step Responses for Multiple Amplitudes (Closed Valve) 77
Figure 5.12 Relative Velocity for Multiple Sinusoidal Excitations: Part 1 78
Figure 5.13 Relative Velocity for Multiple Sinusoidal Excitations: Part 2 78
Figure 5.14 Vibration Isolation Rates of Closed-Loop Performances 79
Figure 5.15 Frequency Response Plots 81
Figure 5.16 Step Response Plots 81
Figure 5.17 Sinusoidal Responses: Part 1 81
Figure 5.18 Sinusoidal Responses: Part 2 81

Figure 6.1 The Sliding Conditions (Jean J, Slotine, W., Li) 83
Figure 6.2 The Sliding Surface (Jean J, Slotine, W., Li) 84
Figure 6.3 FBD of the Reference Model 85

Figure 6.4 Sample Plots: Force Input for Discontinuous and Continuous Control Law 89
Figure 6.5 Sample Plots: m Values Result in Nonconvergent Solutions 91
Figure 6.6 Excitation-1: Plots for m 92
Figure 6.7 Excitation-2: Plots for m 92
Figure 6.8 Excitation-3: Plots for m 93
Figure 6.9 Excitation-1: Plots for ρ 93
Figure 6.10 Excitation-2: Plots for ρ 94
Figure 6.11 Excitation-3: Plots for ρ 94
Figure 6.12 Excitation-3: Plots for ρ= -3000 95
Figure 6.13 Excitation-1: Plots for ϕ 95
Figure 6.14 Excitation-1: Plots for Multiple Stiffness Values 96
Figure 6.15 Excitation-2: Plots for Multiple Stiffness Values 96
Figure 6.16 Excitation-3: Plots for Multiple Stiffness Values 96

Figure 7.1 Structure of the Sliding Mode H-Infinity Robust Control 97
Figure 7.2 Damping Coefficient Vs Orifice Voltage 98
Figure 7.3 Orifice Voltage Vs Damping Coefficient for 0.2 inch Excitation Case . . 99
Figure 7.4 Curve-Fit Function $C = f(V)$ for 0.2 inch 99
Figure 7.5 Curve-Fit Function $C = f(V)$ for 0.3 inch 100
Figure 7.6 Curve-Fit Function $C = f(V)$ for 0.4 inch 100
Figure 7.7 Curve-Fit Function $C = f(V)$ for 0.5 inch 100
Figure 7.8 Curve-Fit Function $C = f(V)$ for 0.6 inch 101
Figure 7.9 Curve-Fit Function $C = f(V)$ for 0.7 inch 101
Figure 7.10 Performances for the Nonlinear Model 103
Figure 7.11 Simulation Results for Case 1: Part 1 105
Figure 7.12 Simulation Results for Case 1: Part 2 105
Figure 7.13 Simulation Results for Case 2: Part 1 105
Figure 7.14 Simulation Results for Case 2: Part 2 106

Figure 7.15 Simulation Results for Case 3: Part 1 106
Figure 7.16 Simulation Results for Case 3: Part 2 107
Figure 7.17 Experimental Results for the Sinusoidal Excitation with 5 rad/s 107
Figure 7.18 Experimental Results for the Sinusoidal Excitation with 8.5 rad/s . . . 108
Figure 7.19 Experimental Results for the Sinusoidal Excitation with 11 rad/s . . . 108
Figure 7.20 Experimental Results for the Sinusoidal Excitation with 14.1 rad/s . . 108
Figure 7.21 Experimental Results for the Sinusoidal Excitation with 25 rad/s . . . 108
Figure 7.22 Experimental Results for the Sinusoidal Excitation with 30 rad/s . . . 109
Figure 7.23 Summary for the Vibration Isolation Study 109
Figure 7.24 Closed-Loop Vs Closed Valve 111

ACKNOWLEDGEMENTS

I would like to take this opportunity to express appreciation to my advisor, Dr. Atul G. Kelkar, for his valuable guidance during my graduate research study. This research work would not get progressed without Dr. Kelkar's detailed instructions. I also appreciate his great help during this thesis writing.

I would also like to thank my committee members, Dr. Jerald M. Vogel, Dr. Qinze Zou, Dr. Greg R. Luecke, and Dr. Gap-Yong Kim, for their valuable suggestions to this research work.

ABSTRACT

The objective of this thesis research is to analyze the pneumatic suspension systems to improve their vibration isolation performance. The work presented in this thesis addresses modeling, analysis and control of the pneumatic suspension system. First, the static and dynamic characteristics of a generic pneumatic suspension system are studied, followed by the development of a nonlinear model of the pneumatic suspension system for multiple operating conditions. An air spring- accumulator system has various dynamic nonlinearities which are explored extensively through numerous simulations as well as exhaustive experimental work. One of the main objectives of this work was to better understand the physics behind the operation of air spring-accumulator system, obtain reliable math model, and develop effective control design for such systems. In terms of of the controller design, a control-oriented analytical model is obtained by the system identification techniques. Then, a model reference H-infinity controller design is presented based on the system-id where control input is the modulation of orifice opening using an electronically-controlled proportional solenoid valve. The experimental results show that the closed-loop system with designed controller significantly improved the vibration isolation performance over a wide frequency range. It is shown that the inherent vibration isolation characteristics of air spring-accumulator system can be exploited through careful modeling and advanced control design. The pneumatic system offers a much economical and easy way to maintain low weight isolation system for various applications such as over the road trucks, automobiles, gurneys. etc. Finally, potential enhancements to the system are proposed for future work.

CHAPTER 1. Introduction

This chapter gives some background of vibration isolation systems, discusses their advantages and drawbacks and provides motivation for the work presented in this thesis. The chapter first gives some historical perspective on the traditional suspension systems followed by current state of the art in pneumatic isolation systems. Subsequently, the motivation for the work presented in this thesis is given by identifying the gaps in the current isolation technologies and potential areas for improvements. Finally, the chapter concludes with the outline of the thesis.

1.1 Background of Automotive Suspension System

Automotive suspension system traditionally consists of stiffness elements such as mechanical springs and damping element such as hydraulic shock absorbers. Typically, in past, the suspension mechanisms have been provided only between wheelbase or axles and chassis. There was no vibration isolation provided between chassis and automobile body/cabin. With increasing demand for comfort in competitive market it has become common to provide some sort of vibration isolation between chassis and passenger cabin. The requirement of added isolation is becoming more of a safety requirement than comfort for off-road vehicles such as agriculture and construction machines, utility vehicles, and the over-the-road trucks. This has motivated continued research to seek better vibration isolation technologies which are economical, high performance and low maintenance.

1.1.1 Historical Perspective

The mechanical shock absorbers were first installed in automobiles by Mors of Germany in 1901 (1). The early automotive suspension typically employed leaf springs as a means for isolating vibrations because they are simple, robust and cost effective. For example, Henry

Ford's Model T employed one leaf spring at each axle (2). Even today, leaf springs are used on the suspensions of heavy vehicles and trucks (3). The passenger cars of today do not employ leaf springs as they have inherent limitations when it comes to low-weight applications. Coil springs and torsion bars are replacing the leaf springs in current passenger vehicles. The first coil spring patent was granted to R. Tredwell in 1763 (British patent No.792) (2). In 1934, most automobile manufacturing companies started using coil spring in the front wheels, and each wheel was suspended individually. After World War II, coil springs were installed for the front wheels in all automobiles, and until now coil springs are still widely used in the automotive industry due to low cost and good performance (4).

Torsion bar suspensions have advantages over coil springs when the space is limited. Torsion bars were first employed on a 1921 Leyland vehicle. After Dr. Ferdinand Porsche standardized the torsion bar suspension system, volkswagon started using torsion bar suspension in 1933 and the current Beatles are still using the torsion bar suspension systems (4).

Another important type of mechanical system that is used to arrest vibrations is the pneumatic suspension, usually called air suspension. Pneumatic suspension systems use air springs rather than the traditional mechanical coil springs or torsion bars. The idea of the air spring was first introduced in 1847. The US inventor John Lewis contributed the idea and was granted the US patent No. 4,965 for "Pneumatic Springs for Railroad Cars, Locomotives, Burden-cars, Bumpers & c" (5). With the development of rubber technology, Firestone first installed the pneumatic suspension system in an experimental car called "Stout-Scarab"(2). In 1958, GM also started to use the passive pneumatic suspensions in its vehicles. Presently, the pneumatic suspension system is widely used in the major brand of automobile industry and the truck industry such as the semi trailers and trucks. However, the pneumatic suspension in use is still very rudimentary in its form. Almost all of the pneumatic suspensions used in the vehicles consist of pressurized air bags.

1.2 Motivation

This section is aimed at describing the opportunities that exist for advancing the state-of-the-art in vibration isolation and carving out the niche which motivates the work of this

thesis. The chapter is divided into five sections. First, the advantages of the pneumatic suspension system are summarized, followed by the previous research work on the control strategies employed on the automotive suspension system. Then, the limitations of the state-of-art isolation technologies are discussed and an innovative pneumatic suspension concept is proposed. Finally, the previous work on analytical modeling of pneumatic suspensions is reviewed and objectives of this research are laid out.

1.2.1 Advantages of the Pneumatic Suspension System

Compared with the traditional mechanical suspension system, the pneumatic suspension employing air springs has certain advantages as described below:

1. Compared with the mechanical suspension, the spring rate of pneumatic suspension system is low to provide the soft and comfortable ride.

2. Variable load carrying capability: The load an air spring carries can be adjusted over a wide range simply by changing the air pressure while keeping the air spring's static height the same. Whereas the mechanical coil springs do not have that wide range of load carrying capacity. The reason being, the air spring has higher potential energy storage than a traditional mechanical spring.

3. Adjustable spring rate: For air springs, the spring rate could be adjusted by changing the air pressure while keeping the air spring height. For the mechanical suspensions, the spring rate is always a constant value.

4. User friendly height control: An air spring's desired height can be modulated by connecting the air spring to a compressed air source whereas the desired static height for mechanical spring changes with the load and cannot be modulated.

5. Quiet operation: Since the flexible rubber member of the air spring moves freely, there is not much noise coming from the pneumatic suspension system. For the mechanical suspensions, noisy operation could result due to contact between mechanical parts.

Presently, air springs are widely used in truck industry to take out the high frequency spikes in the vibration response.

1.2.2 Control Considerations in Suspension

Although the specifics of control design for typical suspension system may vary from one design to other, in general, the control strategies employed can be divided into three broad classes - passive, active, and semi-active, suspensions. Given below is background of these types and their pros and cons.

1. Passive Suspension System

Early automotive suspension study dates back to 1936 by Lanchester (6). Since then several decades of development has led to use of the passive suspension systems in various types of vehicles. Usually, a passive suspension system has a fixed stiffness and damping. An automotive suspension system is called "stiff suspension" when its stiffness value is high, and is called "soft suspension" when it has low stiffness. A soft suspension would provide good vibration isolation performance and create the comfortable ride feeling, but it is not good for vehicle handling capability, especially when the vehicle is cornering and braking. On the other hand, a stiff suspension would provide the optimal vehicle handling capability, but it is ineffective for vibration isolation during the ride. Therefore, for a passive suspension it is a natural conflict between an effective vibration isolation performance and a good handling capability. The effective vibration isolation performance means the low vibration transmissibility between the sprung mass and base, and the good handling capability can be represented as the low suspension deflection transmissibility. Figures 1.1a and 1.1b clearly show that the low vibration isolation and low suspension deflection cannot be reached simultaneously for a fixed stiffness value. The passive pneumatic suspension system with fixed stiffness and damper cannot avoid its natural conflict between the comfortable drive feeling and the suspension deflection requirement. **A soft pneumatic suspension system could easily reach its stroke limitation and generate the hard stop giving discomfort and possible injury to the driver. A harder pneumatic suspension would minimize the suspension deflection with the inefficient vibration isolation. Therefore, a control strategy is needed which can provide a ride as soft as possible when needed and can arrest the motion by providing high stiffness when needed**.

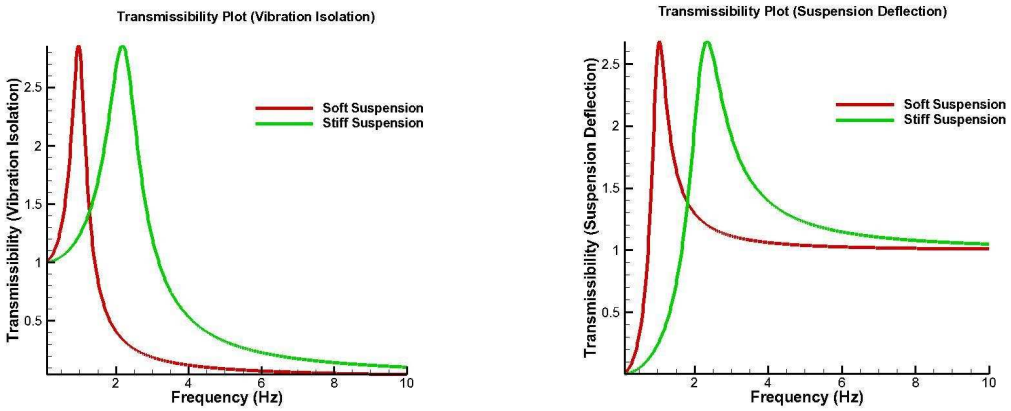

(a) Isolation Transmissibility Plot

(b) Deflection Transmissibility Plot

Figure 1.1: Plots for Passive Suspension System

2. Active Suspension System

Based on the previous study (7)-(10), the vibration isolation performance of a controlled suspension is much better than that of a passive suspension system. To overcome the drawbacks of the passive suspension design, active suspension systems have been considered and designed. The active suspension idea was first introduced by Federspiel in 1954 (11). It was later significantly developed by many other scientists (12)-(21). Typically, the active suspensions can be divided into two different types: fully active suspension and semi-active suspension.

a. Fully Active Suspension System

As shown in Fig. 1.2, the traditional spring and damper in a passive suspension are replaced by an individual force actuator to control the suspension based on the sensory feedback in a fully active suspension system. In terms of control strategies employed by the fully active suspension, many control strategies, like robust control, sliding mode control, and linear parameter varying control(LPV) have been employed in the active suspension study. Lauwerys, Swevers, and Sas (22) designed a robust controller for an active suspension in a quarter car test-rig. The linear models used in controller design were obtained by the system identification in frequency domain. The simulation results showed the improved vibration isolation performance with the designed controller based on a μ-synthesis scheme.

Yoshimura and Kume (23) proposed an active suspension system for a quarter car model

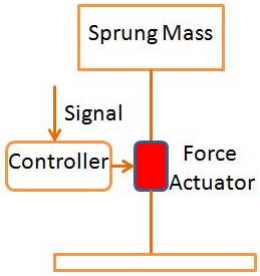

Figure 1.2: Fully Active Suspension

based on the idea of sliding model control, and the LQ control theory was used to construct the sliding surface. The results showed that the controller improved the vibration isolation of the car body more than the passive suspension system.

Kim and Ro (24) designed a sliding mode controller for the suspension of a quarter car model, and they also performed a comparative study by comparing the sliding mode controller with the alternative adaptive control strategy. They concluded that the performance of the sliding mode control is better than that of the adaptive control. The whole study was based on simulation only and the system uncertainties were assumed without experimental validation.

Although the fully active suspension systems have evolved a great deal and are actually employed in practice such as the Bose Ride System, shown in Fig. 1.3. The use of the fully active suspension is very limited except in some luxury vehicles or trucks for a couple of reasons:

1. High power consumption. A fully active control requires a significantly high power consumption for a large bandwidth control to provide the comfortable ride (25), (26).

2. The fully active suspensions requires frequent maintenances which typically will lead to high maintenance costs.

3. The performance of a fully active suspension highly depends on the road conditions and the working environment.

4. The "failure-mode" of the actuator could negatively affect the system performance significantly because the actuator is the only element in the suspension system (26).

Considering these drawbacks with fully active suspensions, a new control strategy is needed to provide better performance than the passive systems do while being cost-effective.

Figure 1.3: Bose Ride System and Its Performance (http://www.bose.com)

b. Semi-Active Suspension System

As an alternative to the fully active suspension, semi-active suspension concept started emerging to provide optimal solution in terms of cost and performance. It was first introduced by Crosby and Karnopp in 1974 (27). A schematic of the semi-active suspension is shown in Fig. 1.4a. Different from the fully active suspension, the semi-active suspension uses a controllable damper instead of the force actuator. The semi-active suspension would not have the same control performance as the fully active suspension does because it only works against the direction of the suspension movement, but it meets a good balance between the performance and affordability. Semi-active suspensions have been attractive for several years and have started finding their applications into practice, for example, Audi semi-active suspension employing MR damper as shown in Fig. 1.4b.

There are numerous research works on semi-active suspension (28)-(31). The studies have covered applications to various types of vehicles such as military tanks by Miller and Nobes (32) and off-road vehicles by Margolis and Noble (33). A variety of control schemes have been employed by semi-active suspension systems: the skyhook control (34), adaptive schemes (35),(36), H-infinity control (37), and model reference control (38).

Karnopp, Crosby, and Harwood (34) explored the possibility of using a semi-active force generator to control the vibration of a sprung mass system based on sky-hook control law instead of using the active control strategy. The simulation results illustrated that the performance

(a) Diagram (b) Audi Semi-Active Suspension (Internet)

Figure 1.4: Semi-Active Suspension

comparable to that of fully active vibration control system can be achieved with the semi-active type of device.

Hong, Sohn, and Hedrick (35) investigated a road-adaptive control scheme for the semi-active Macpherson suspension system. The actuator dynamics was incorporated during the hardware-in-the-loop simulations. The simulation results illustrated that a competitive control performance was achieved by adopting the road adaptive control laws.

Song and Ahmadian (36) developed a nonlinear adaptive semi-active control algorithm for the magnetorheological suspension systems. They designed an adaptive algorithm based on the on-line system identification technology. For both the low-damping and high-damping cases, the simulation results shown that the proposed adaptive control strategy is effective to minimize both the acceleration of the mass and the relative displacement.

Kawabe and Isobe (37) proposed a semi-active suspension control design based on the H-infinity optimized frequency shaping method. The proposed method requires the suspension stroke and its velocity signal to generate the damping force, and the effectiveness of the proposed method was verified by the computer simulation.

Dixit and Buckner (38) developed a model reference sliding mode control on the semi-active vehicle suspensions. The derived suspension models include the system nonlinearities, and the skyhook damping is employed as the nonlinear reference model. The simulation study illustrated the suspension displacement was reduced after employing the sliding mode controller.

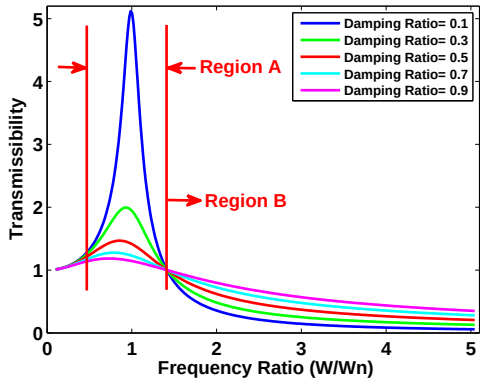

Figure 1.5: Transmissibility Plots for Sprung Mass

In summary, fully active control or semi-active control, has much better performance than a passive suspension. **Among semi-active and fully active systems semi-active offers optimal solution in terms of cost and performance considerations. This research is focused on exploring semi-active configurations of pneumatic suspension systems**.

1.2.3 Limitations of the State-of-the-Art Vibration Isolation Systems

Figure 1.5 shows a classic transmissibility plot for an isolation system with single degree of freedom as a function of the ratio of the excitation frequency to the natural frequency. The plot consists of two regions as follows along the frequency axis.

Region A: This is the region where excitation frequency is in the neighborhood of the natural frequency of the system and one's ability to damp out vibrations using some kind of effective damping dictates the isolation performance. Fully active suspensions can generate higher damping force and achieve better performance here.

Region B: This is the region away from the natural frequency of the system and better performance is actually achieved by reducing the damping and making the system really soft.

In view of this, an ideal suspension should be such that it offers no damping at all in region B and high damping in region A. These are hard to achieve with fixed parameter system; however, if one can design a system which will always try to keep the system in the region B by modulating the frequency of the system and controlling the damping at the same time that will be the best solution. The semi-active pneumatic system described in the next section has

this capability and will be the focus.

Although the semi-active suspension such as MR damper could achieve a good performance in region A due to the adjustable damping capability, such kind of system cannot provide the effective vibration isolation in region B due to the fixed natural frequency of the system. Although the fully active suspension employing the hydraulic force actuator could provide the effective vibration isolation on both the regions of A and B, the applications of such system is very limited due to the high cost, high power consumption, and so on. **Therefore, an innovative pneumatic suspension to continuously control the suspension stiffness and damping employing the solenoid valve is proposed in this thesis to address the shortcomings by both the semi-active suspension system employing MR damper and the fully active suspension system**.

1.2.4 Proposed Pneumatic Suspension System

Figure 1.6 illustrates the diagram of the proposed pneumatic suspension system. It consists of a sleeve-type air spring, an electronically controlled proportional solenoid orifice valve, the accumulator (reservoir tank), height control valve and etc.. During transient operations the air moves from air spring to accumulator and back through the orifice valve whereby flow resistance is encountered thus providing damping function. The magnitude of the damping action is set by the size of the orifice, thus enabling variable damping rate for the suspension through control of orifice size. The natural frequency of the suspension system is set by its enclosed air volume.

1.2.5 Modeling of Pneumatic Suspension Systems

As discussed above, there is a large potential for improving isolation performance of the pneumatic suspension system by employing the proposed control strategy. However, we have to face the modeling difficulty of the pneumatic suspension system because it is a highly non-linear system. Therefore, building up an accurate and control-oriented model of the pneumatic suspension system is the key for the controller design. The purpose of this subsection is to summarize the previous research work on the modeling of the pneumatic suspension and to give out the suggestion on the analytical modeling in this thesis work.

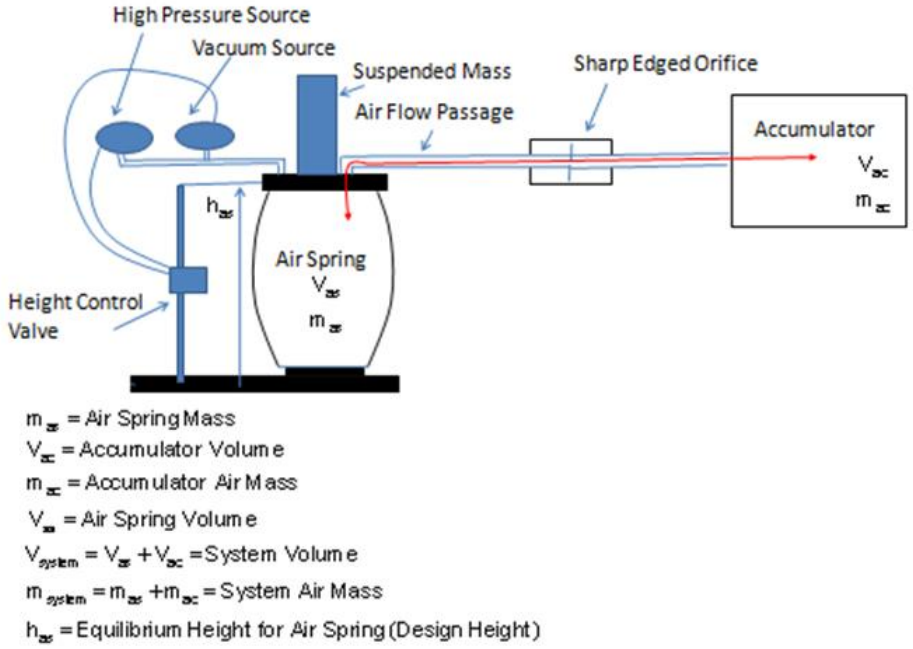

Figure 1.6: Diagram of Proposed Pneumatic Suspension System (Courtesy of IVS)

Some research works (39) to (47) have been carried out to develop the analytic model for an air spring or a pneumatic isolator involving the nonlinear characteristics. Niteo (39) employed an experimental characterization study to develop an analytical model of pneumatic suspensions. A nonlinear model and its linearized version were given. The prediction of the stiffness, damping factor, and the transmissibility were presented in their study. Erin and Wilson (40) developed a model of a pneumatic vibration isolator including the mechanism of the isolator diaphragm, and the diagram of the isolator is shown in Fig. 1.7. The proposed model includes hysteretic damping, transmissibility curves, and the stiffness elements. The validity of the derived model was verified by different operating conditions based on the simulation results. Berg (41) proposed a non-linear model for general three-dimensional motions of an air spring model used for rail road vehicles, and the hysteresis damping due to the friction behavior has been studied. Chang and Lu (42) established a dynamic model of air spring which included the heat transfer process of the air spring, and the analytical model was verified by the experimental results. Deo and Suh (43) derived a thermodynamic model to estimate the stiffness value and damping due to opening the valve to increase the volume of the air spring. However, their study

is just limited in the analytical derivation and simulation analysis, and no experimental results were provided to verify the analytical models. Berg (44) developed a one dimensional non-linear rubber spring model which is based on the combination of elastic, friction and viscous forces. Internal high computation programming is needed to apply the derived model into reality. Sayyaadi and Shokouhi (45) developed a complete nonlinear thermo-dynamical air spring model. They investigated the influences of suspension parameters on the performance of an air spring, including air accumulator volume, connecting pipe's length and diameter. Fox, Roebuck, and Cebon (46) developed a semi-empirical mathematical model of a rolling-lobe air spring, and the simulation results are provided to verify the derived model. Quaglia and Guala (47) presented an analytical model of the bellow air spring to predict the static characteristic of spring. The analyzed system is shown in Fig. 1.8. The derived model could describe the axial force and the effective area apart from its geometric size.

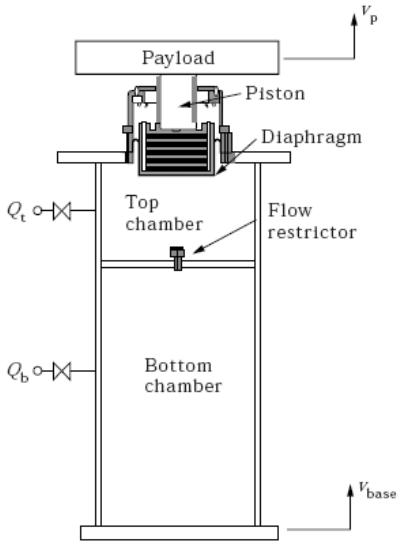

Figure 1.7: Pneumatic Isolator Suspension System-Case 1 (Erin, C. and Wilson, B.)

Besides the models developed for the air springs as above, some other research work was performed to model the orifice. A device can be used to adjust the stiffness and damping of pneumatic suspension system. Henderson and Raine (48) developed their study on a pneumatic suspension with orifice damping used in an ambulance stretcher, and a nonlinear suspension model using thermodynamic knowledge was derived. The damping effects generated by chang-

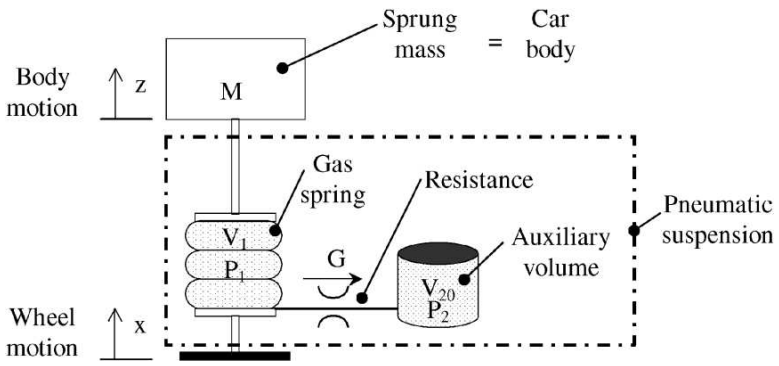

Figure 1.8: Pneumatic Isolator Suspension System-Case 2 (Quaglia, G. and Guala, A.)

ing the orifice size was studied based on the model. Popov and Sankar (49) developed a detailed non-linear damping model of orifice-type dampers which takes into account the oscillatory nature of the liquid flow and the variable hydraulic resistance of the liquid path. Their studies mainly focus on the effects of non-linear orifice type damping on the response of one and two-degree of freedom systems. Vaughan and Gamble (50) presented a nonlinear dynamic model and simulation study of a high speed direct acting solenoid valve by dividing the solenoid with two subsystems: a proportional solenoid valve and a spool assembly. Both the static and dynamic responses of the valve to voltage was studied by the simulation and were verified by the experimental reaults.

In summary, previous studies significantly contributed to modeling of pneumatic suspension system and the solenoid orifice valves respectively. However, the semi-active configuration modeling is not addressed in the literature in which air mass exchange between air spring and accumulator is controlled actively by an actuator such as solenoid valve for example.

This thesis is dedicated to expediting dynamical complexity of semi-active pneumatic suspension system by obtaining both high fidelity nonlinear dynamical model and adequate fidelity linear control design model and designing suitable control strategy for this system.

1.3 Outline of the Thesis

The principal objective of this research is to gain deeper understanding of the dynamic characteristics of the semi-active pneumatic suspension system, develop comprehensive higher fidelity dynamic model, and design controller than can provide optimal vibration isolation performance. To reach this goal, there are several specific objectives that need to be met which are given follows,

1. Understand the static and dynamic characteristics of the pneumatic suspension system.

2. Develop higher fidelity nonlinear model as the truth model of the system as well as simplified but adequate fidelity linear model for control design.

3. Design and evaluate control strategy to improve the closed-loop performance of the pneumatic suspension system.

4. Conduct extensive experimental validation of the open-loop as well as closed-loop system behavior.

5. Make conclusions and recommend future directions for the research.

Given below is the layout of each chapter:

The first chapter gives brief introduction, background of suspension technologies and motivation for the work of this thesis.

Chapter 2 deals with the modeling of static and dynamic stiffness characteristics of the system and experimental verification of these parameters. The dependence of these parameters on the excitation amplitudes and orifice voltage is thoroughly explored.

Chapter 3 gives development of complete nonlinear analytical model of the pneumatic suspension system.

Chapter 4 focuses on obtaining control design model. The linear model development is presented using both analytical and system identification methods. A comparison is presented between responses obtained from identified models and real hardware. The dependence of various system and operational parameters on the system model is also studied. The considerations for choosing appropriate system model for control design are discussed.

Chapters 5 and 6 focus on H-infinity and sliding mode controller designs. A detailed develop-

ment of the controllers with pre-requisite background of these methods is presented. Numerous simulation results are also given to check the efficacy of these controller designs.

To implement the controllers on the real suspension system, the mapping function between the damping force and orifice voltage input was first determined in chapter 7. The development of the mapping function gives the process used to obtain two different types of mappings between solenoid voltage and corresponding damping coefficient. The experimental results are presented in the latter part of chapter 7. A series of experiments were performed to validate the finding of simulation work from previous chapters. It was confirmed that the proposed control design approaches give effective control for the new pneumatic suspension concept. The advantages as well as limitations of controllers were also determined.

In chapter 8, the conclusions about the whole thesis work are made and the directions for future work are discussed.

CHAPTER 2. Static and Dynamic Characteristics of the Pneumatic Suspension Systems

This chapter is devoted to understanding the static and dynamic behavior of pneumatic suspension systems. As previously mentioned, the dynamical characteristics of pneumatic suspensions tend to have peculiar nonlinearities which need be understood properly in order to be able to take advantage of its inherent dynamics for providing better vibration isolation performance. This chapter explores various mechanical as well as thermodynamic phenomena that enter into modeling of air spring stiffness. The chapter introduces the concept of dynamic stiffness and develops mathematical relationships that describe static as well as dynamical stiffness of the air spring.

2.1 Concepts of the Air Spring

The air spring is essentially a deformable container which consists of high pressure air inside, and is varied by the volume change of the air spring. The compression and expansion of the air spring not only changes the pressure but also influences the heat exchange in and out of the air spring. Therefore, the air spring tends to be inherently nonlinear also the stiffness of the air spring depends on the level of excitation and frequency of excitation. Different thermodynamic processes involved during functioning of the pneumatic suspensions are listed below.

2.1.1 Isothermal Process

An isothermal process is the process where temperature of system is kept constant via exchanging heat with the surroundings. A necessary condition for this process is the slow deformation of the air spring. In that case, the air spring could keep the constant temperature

by fully exchanging heat with the surroundings. The ideal gas law for the isothermal process is given as,

$$P_0 V_0 = P_1 V_1 \tag{2.1}$$

where, P_0 is the initial absolute pressure of the air spring; V_0 is initial volume of the air spring; P_1 is the final absolute pressure of the air spring; and V_1 is the final volume of the air spring.

2.1.2 Adiabatic Process

An adiabatic process does not allow the system to exchange heat with its surroundings and the temperature of the system varies. A rapid oscillation of air spring is considered as an adiabatic process because very little or no heat exchange between the air spring and its surroundings. Therefore, the air spring temperature is increased during compression and reduced during expansion. The ideal gas law for adiabatic process could be written as,

$$P_0 V_0^{\gamma} = P_1 V_1^{\gamma} \tag{2.2}$$

where, $\gamma = \frac{C_p}{C_v} = 1.4$: heat capacity ratio of air; C_p: specific heat of gas at constant pressure; C_v: specific heat of gas at constant volume.

2.1.3 Polytropic Process

A polytropic process is employed when the thermal process could not be modeled as either the isothermal process or the adiabatic process, and the ideal gas law is,

$$P_0 V_0^{\kappa} = P_1 V_1^{\kappa} \tag{2.3}$$

where, κ : polytropic index, and $1 < \kappa < \gamma$

Table 2.1: Initial Conditions for Static Test

Height (m)	Load (N)	Pressure (Psi)
0.1143	2250	71.2

2.1.4 Effective Area

Since air spring diameter and height changes during its operation one has to use an "effective area" to compute the pressures and associated quantities required in assessing dynamic behavior of the air spring. Effective area, A_{eff}, is the area of the air spring considered to be a load carrying area of the air spring. It is an important parameter for air spring dynamics because both the air spring force and its stiffness depend on the A_{eff} value. Since there is no geometrical definition for A_{eff}, it is difficult to measure it directly. Therefore, a series of experimental tests were designed to determine A_{eff}. The previous studies (46) have shown that A_{eff} changes as the air spring deformation, X_r, changes. The objective of this experimental study is to obtain the relationship between A_{eff} and X_r. The initial conditions for the static tests are listed in Table 2.1.

The load an air spring can carry at equilibrium condition is given by,

$$G_{sm} = F = (P_s - P_a)A_{eff} = P_{sg}A_{eff} \tag{2.4}$$

$$A_{eff} = \frac{F}{P_{sg}} = \frac{G_{sm}}{P_{sg}} \tag{2.5}$$

where,

G_{sm}: Sprung mass load;

F: Air spring force;

P_s: Absolute pressure of air spring;

P_a: Ambient pressure;

A_{eff}: Effective area of the air spring;

P_{sg}: Gauge pressure of the air spring.

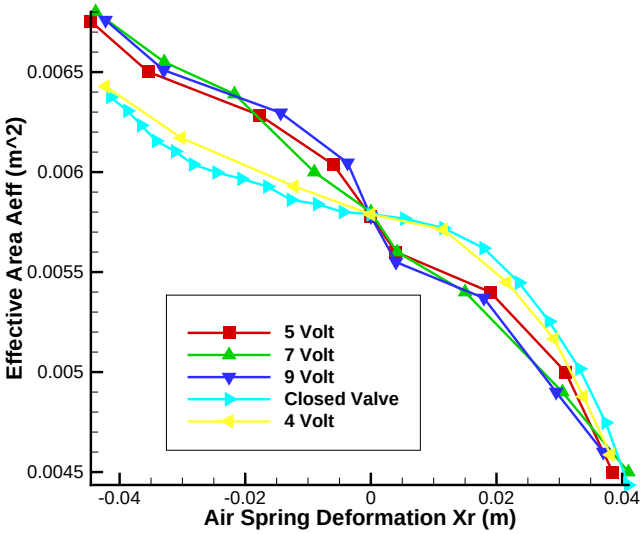

Figure 2.1: Effective Area Vs Deformation

The static tests were conducted based on Eq. (2.5), in which G_{sm} was measured by a weighing scale, and P_{sg} was recorded by a pressure transducer attached to the air spring base. Since A_{eff} is not a constant value but a function of X_r, various loads were applied within the regular air spring stroke range ($\pm$ 0.05 m) from its nominal position. A linear transducer was used to measure X_s. The absolute base displacement, X_d, is equal to zero during the static test, so X_s is equal to X_r according to Eq. (2.6). A complete set of data including G_{sm}, P_{sg}, and X_r was recorded for each load condition, and the mapping functions of $A_{eff} = f(X_r)$ can be generated in Fig. 2.1.

$$X_r = X_s - X_d \tag{2.6}$$

where,

X_r: Air spring deformation;

X_s: Absolute displacement of sprung mass;

X_d: Absolute displacement of shaker base.

The static tests of the pneumatic suspension system were performed under two different conditions:

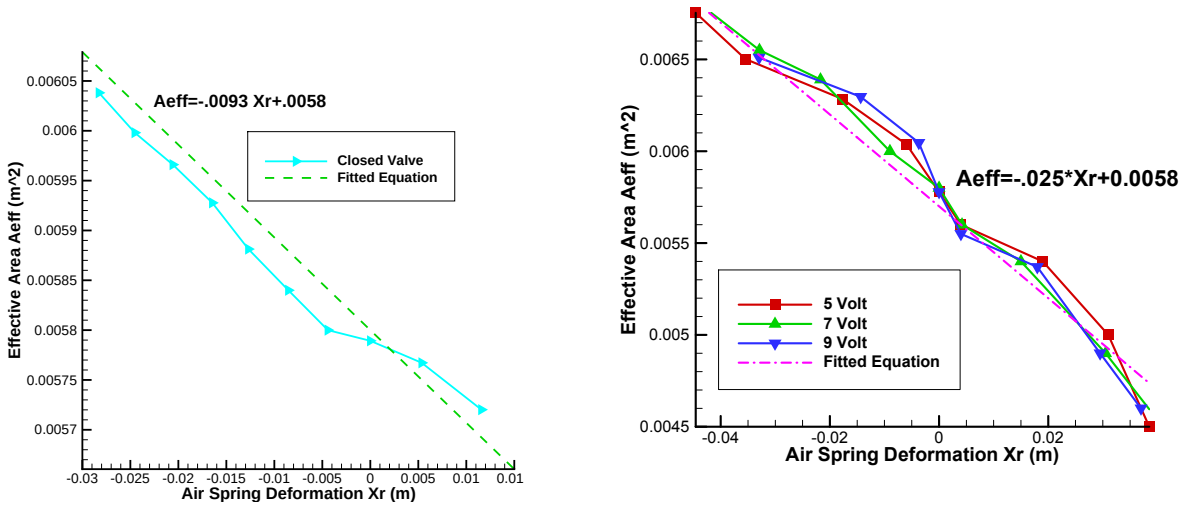

(a) Closed Valve Case

(b) Open Valve Cases

Figure 2.2: Fitted Functions A_{eff}=$f(x_r)$

a. Air spring only system (solenoid valve in closed condition);

b. Air spring + accumulator system (various solenoid orifice opening levels). The input voltage to the solenoid orifice is used to adjust the opening level. According to the manufacture's specification sheet, the valve starts to open at 4 volts and get fully opened at 9 volts. To determine $A_{eff} = f(X_r)$ for various orifice opening levels, four orifice input voltages were tested (4 volts, 5 volts, 7 volts, and 9 volts).

During this research study, the air spring extension is defined as the positive displacement. Figures 2.2a and 2.2b respectively illustrate the fitted linear functions for closed valve and open valve, in which the l_c=-.0093 and l_o =-.025 are the gains for each case.

Summary of the air spring static stiffness tests is given below:

1: A_{eff} is a function of X_r whether the orifice valve is closed or open.

2: A_{eff} for open and closed valve are different.

3: A_{eff} for 4 volts is very close to the one for fully closed valve. This means almost no air passes through the valve for 4 volts orifice input. So the valve when giving 4 volts input can be approximately considered as a closed valve.

4: l_o is steeper than l_c because the enlarging volume influences the air spring dynamics and

stiffness. Based on the Eqs. (2.1) to (2.3), pressure is inversely proportional or power inversely proportional to the system volume. To support the same weight from Eq. (2.4), a high rate of change for A_{eff} for the large volume system is necessary to compensate for its low pressure change.

5: The $A_{eff} = f(X_r)$ are relatively linear for the case of open valve condition but it is nonlinear when the valve is closed.

6: A_{eff} is independent of orifice opening levels.

2.2 Static Stiffness of the Air Spring

By taking the derivative of both sides of Eq. (2.4), one could get the static stiffness equation as follows,

$$K = -\frac{dF}{dX_r} = -\frac{dP_{sg}}{dX_r}A_{eff} - \frac{dA_{eff}}{dX_r}P_{sg} \tag{2.7}$$

2.2.1 Static Stiffness of the Air Spring for Isothermal Process

By combining Eqs. (2.1) and (2.4), and using the fact that P_a is always a constant value, two equations are generated as follows,

$$\frac{dP_{sg}}{dX_r} = \frac{dP_s}{dX_r} - \frac{dP_a}{dX_r} \tag{2.8}$$

$$\frac{dP_a}{dX_r} = 0 \tag{2.9}$$

By combining Eqs. (2.1), (2.8), and (2.9), the equation about the change rate of air spring gauge pressure to air spring deformation is given by,

$$\frac{dP_{sg}}{dX_r} = \frac{dP_s}{dX_r} = -\frac{P_{s0}V_{s0}}{V_s^2}\frac{dV_s}{X_r} = -\frac{P_s}{V_s}\frac{dV_s}{X_r} \tag{2.10}$$

$$A_b = \frac{dV_s}{dX_r} \tag{2.11}$$

where,

P_{s0}: Absolute pressure of air spring at initial state;

V_{s0}: Volume of air spring at initial state;

V_s: Volume of air spring at final state;

A_b: Bottom cylinder area of air spring.

By substituting Eqs. (2.10) and (2.11) into Eq. (2.7), one can divide Eq. (2.7) into two parts as follows,

$$K = K_{vi} + K_{eff} \tag{2.12}$$

$$\begin{cases} K_{vi} = \frac{P_s}{V_s} A_b A_{eff}; \text{ Closed Valve} \\ K_{vi} = \frac{P_s}{V_s + V_r} A_b A_{eff}; \text{ Open Valve} \end{cases} \tag{2.13}$$

$$\begin{cases} K_{eff} = -\frac{dA_{eff}}{dX_r} P_{sg} = -l_c P_{sg}; \text{ Closed Valve} \\ K_{eff} = -\frac{dA_{eff}}{dX_r} P_{sg} = -l_o P_{sg}; \text{ Open Valve} \end{cases} \tag{2.14}$$

where,

V_r: Volume of the accumulator;

K_{vi}: Air spring stiffness due to the volume change for isothermal process;

K_{eff}: Air spring stiffness due to the effective area change.

2.2.2 Static Stiffness of the Air Spring for Adiabatic Process

Similarly, the air spring static stiffness K for adiabatic process could be represented by the given equations,

$$K = K_{va} + K_{eff} \tag{2.15}$$

$$\begin{cases} K_{va} = -\frac{dP_{sg}}{dX_r} A_{eff} = \frac{\gamma P_{s0} V_{s0}^{\gamma}}{(V_s)^{\gamma+1}} \frac{dV_s}{X_r} = \frac{\gamma P_s}{V_s} A_b A_{eff}; \text{ Closed Valve} \\ K_{va} = -\frac{dP_{sg}}{dX_r} A_{eff} = \frac{\gamma P_{s0} (V_{s0} + V_r)^r}{(V_s + V_r)^{\gamma+1}} \frac{dV_s}{X_r} = \frac{\gamma P_s}{V_s + V_r} A_b A_{eff}; \text{ Open Valve} \end{cases} \tag{2.16}$$

where,

K_{eff} in Eq. (2.15) is same as the one in Eq. (2.14) and γ=1.4;

K_{va}: Air spring stiffness due to the volume change for adiabatic process.

2.2.3 Static Stiffness of the Air Spring for Polytropic Process

Similarly, the static air spring stiffness K for polytropic process can be given as follows,

$$K = K_{vp} + K_{eff} \tag{2.17}$$

$$\begin{cases} K_{vp} = -\frac{dP_{sg}}{dX_r} A_{eff} = \frac{nP_{s0}V_{s0}^n}{(V_s)^{n+1}} \frac{dV_s}{X_r} = \frac{nP_s}{V_s} A_b A_{eff}; \text{ Closed Valve} \\ K_{vp} = -\frac{dP_{sg}}{dX_r} A_{eff} = \frac{nP_{s0}V_{s0}^n}{(V_s+V_r)^{n+1}} \frac{dV_s}{X_r} = \frac{nP_s}{V_s+V_r} A_b A_{eff}; \text{ Open Valve} \end{cases} \tag{2.18}$$

where,

K_{eff} in Eq. (2.17) is same as the one of Eq. (2.14) and $1 < n < 1.4$;

K_{vp}: Air spring stiffness due to the volume change for polytropic process.

2.2.4 Summary of the Air Spring Static Stiffness Analysis

The math model of static stiffness of air spring was obtained analytically using constitutive physical relationships. Several experimental tests were conducted to validate the math models. The experiments essentially involved determination of effective area of the air spring. The sprung mass load was recorded for each load case, and X_r was recorded simultaneously. By combining F and X_r together, the experimental K values were generated as shown in Figs. 2.3a and 2.3b for the closed valve and open valve conditions respectively. To be consistent with the stiffness convention, the compressed air spring deformation is defined as positive in Figs. 2.3a and 2.3b.

The air spring stiffness K_e for the closed valve and open valve were determined by fitting a linear line in Figs. 2.3a and 2.3b respectively. K_e for the closed valve is around 2.7 times of the one for the open valve case. The parameters used to calculate the air spring stiffness for various operating conditions are included in Table 2.2. Table 2.3 summarizes the results for the theoretical and experimental stiffness values. By comparing the experimental and theoretical results, one can conclude that the static experimental test is close to the adiabatic

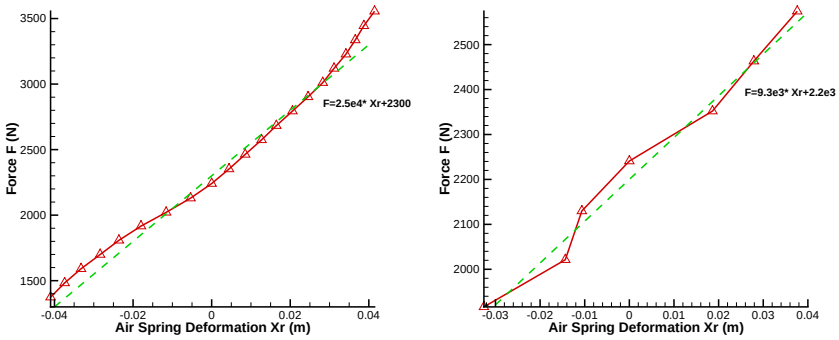

(a) Closed Valve (b) Open Valve

Figure 2.3: Static Stiffness (P_{s0}=71.2 psi)

Table 2.2: Parameter Values for Calculating Static Stiffness of Air Spring

A_b (m^2)	P_{s0} (Psi)	V_{s0} (m^3)	P_s (Psi)	V_s (m^3)	A_{eff} (m^2)	V_r (m^3)
0.0050	71.2	1.33e-3	84.7	1.19e-3	0.0058	0.0189

thermal process. Another interesting fact is that the stiffness value for the open valve case is independent of the thermodynamic processes. The reason is that K_{eff} becomes a dominant factor for the open valve cases, and K_{va} is less important because a large accumulator volume V_r is introduced into the denominator of K_{vi}, K_{va}, or K_{vp}.

2.3 Dynamic Stiffness of the Air Spring

Dynamic stiffness of air spring, K_d, is defined as the average slope of the force-displacement curve as shown in Fig. 2.4a. K_d is dependent on the excitation amplitude, A_{mp}, and frequency, f. By controlling the solenoid valve opening, the amount of air flow passing through the valve

Table 2.3: Theoretical Stiffness Vs Experimental Stiffness

Condition	K_i (N/m)	K_a(N/m)	K_p (N/m)	K_e (N/m)
Closed Valve	1.95e4	2.54e4	1.95e4 $\leq K_p \leq$ 2.54e4	2.5e4
Open Valve	1.04e4	1.07e4	1.04e4 $\leq K_p \leq$ 1.07e4	0.93e4

would be changed. Therefore, the orifice voltage, V_{in}, used to control the opening of the solenoid valve, is another factor that affects K_d. Many experimental tests were performed to study K_d values for different combinations of the excitation amplitude and frequency. The experimental results of the force-displacement relationship for 0.15 inch sinusoidal excitation are listed in Figs. 2.4a to 2.5b, which respectatively represent the results under 4 excitation frequencies (7 rad/s, 10 rad/s, 15 rad/s, and 30 rad/s). Sinusoidal excitations were given to the system as X_d, then X_r and P_s were recorded for each of the test case. To represent the different opening levels of the solenoid valve, multiple voltages were applied (4.5 volts to 9 volts with 0.5 volt increment) during testing with zero voltage corresponding to the closed condition of the valve.

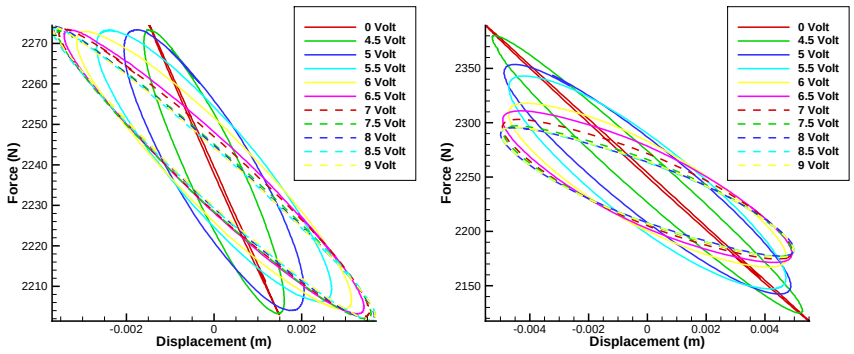

(a) 7 rad/s (b) 10 rad/s

Figure 2.4: Force Vs Deformation (0.15 inch Sinusoidal): Part 1

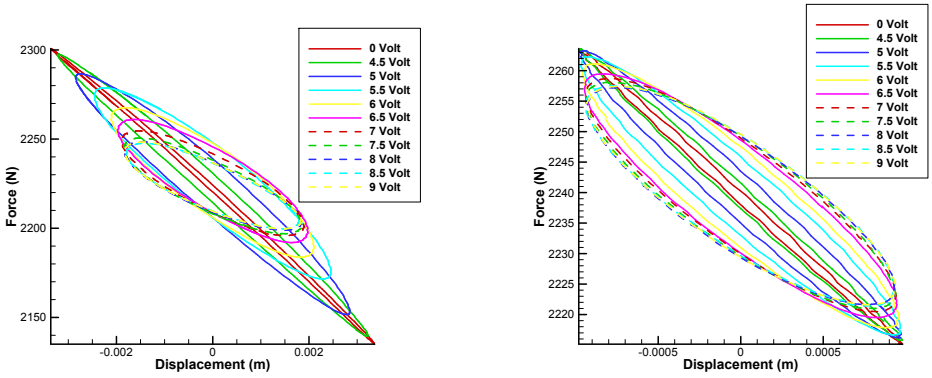

(a) 15 rad/s (b) 30 rad/s

Figure 2.5: Force Vs Deformation (0.15 inch Sinusoidal): Part 2

Figures 2.6 to 2.7 respectatively illustrate the experimental results for 0.3 inch sinusoidal

excitation cases under 4 different excitation frequencies (7 rad/s, 10 rad/s, 15 rad/s, and 30 rad/s). It is noticed that the total amount of available data for 0.3 inch excitation is less than the one for 0.15 inch excitation. The reason is that the force-displacement curve is skewed at large vibration. Therefore, there is no individual K_d for each case and the force-displacement curves were not shown in the plots.

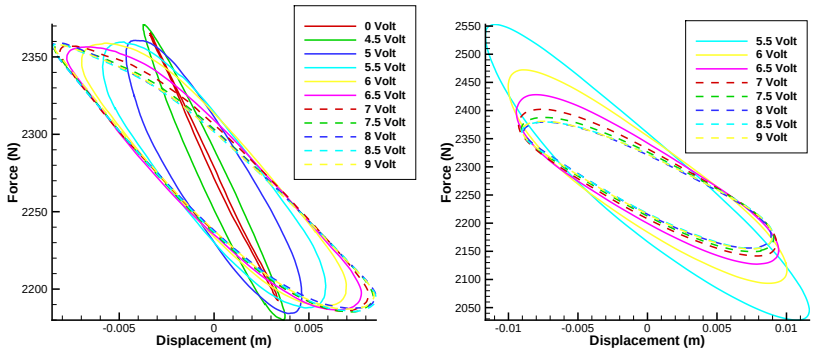

(a) 7 rad/s (b) 10 rad/s

Figure 2.6: Force Vs Deformation (0.3 inch Sinusoidal): Part 1

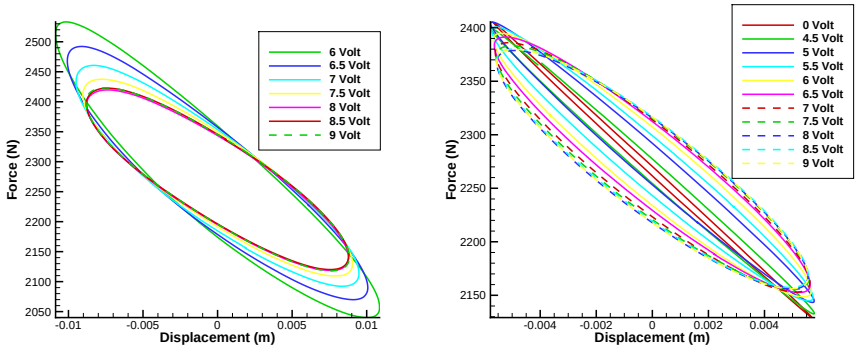

(a) 15 rad/s (b) 30 rad/s

Figure 2.7: Force Vs Deformation (0.3 inch Sinusoidal): Part 2

The experimental study were also performed on 0.5 inch sinusoidal excitation cases under 4 different excitation frequencies (7 rad/s, 10 rad/s, 15 rad/s, and 30 rad/s), and the results are listed in Figs. 2.8 to 2.9. It is observed that the available data in Figs. 2.8b and 2.9a are limited due to the large vibration close to the resonant frequency.

Figures 2.10a, 2.10b, and 2.10c illustrate the summary results for K_d under fixed amplitudes. The results show that K_d is frequency dependent. Under the same A_{mp} and V_{in}, K_d increases

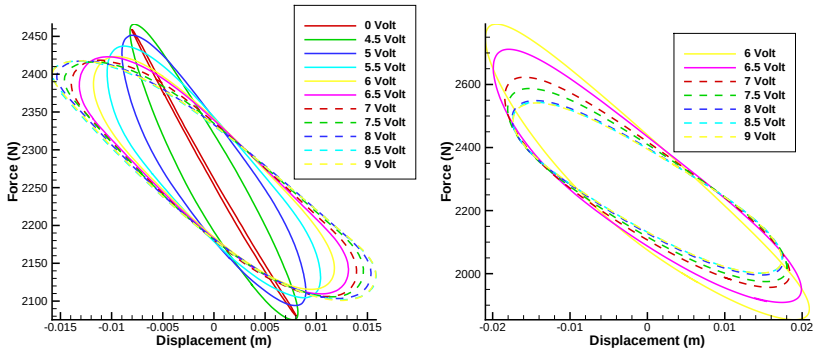

(a) 7 rad/s (b) 10 rad/s

Figure 2.8: Force Vs Deformation (0.5 inch Sinusoidal): Part 1

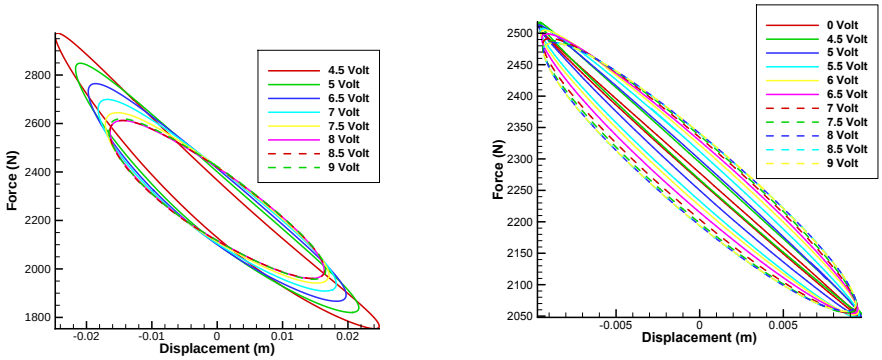

(a) 15 rad/s (b) 30 rad/s

Figure 2.9: Force Vs Deformation (0.5 inch Sinusoidal): Part 2

with increasing f. The reason is because the system does not have enough time to respond for high f. Therefore, the total amount of air flow, Q, passing through the valve reduces with increasing f. The limited air communication would make the system look more like an air spring only system with a high K_d. On the contrast, an excitation with low f would allow the system to have enough time to respond and a large amount of air flow would pass through the solenoid valve, and the system is more close to the fully open valve system with a low K_d.

Besides f, V_{in} also plays an important role to influence K_d because it directly controls the air flow passing through the solenoid valve. Obviously, K_d reduces with an increasing V_{in}.

A_{mp} is another important parameter that influences K_d. Figure 2.11a represents the plots of K_d under the frequency at 7 rad/s. The results show that K_d for each excitation amplitude is almost identical at orifice voltage below 5 volts, but it increases as the increasing f after 5.5 volts. The same trend is followed in Figs. 2.11b and 2.12a. Since those two frequencies

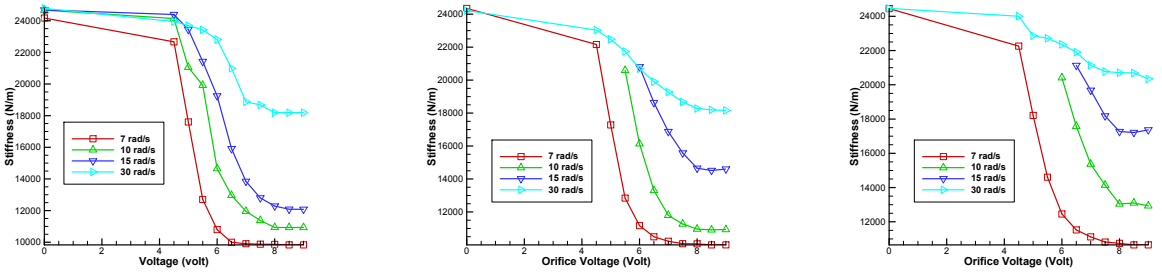

(a) 0.15 inch (b) 0.3 inch (c) 0.5 inch

Figure 2.10: Dynamic Stiffnesses for Various Excitation Amplitudes

(10 rad/s and 15 rad/s) are very close to the system's natural frequency, the available data is limited due to the aggressive vibration with low V_{in}.

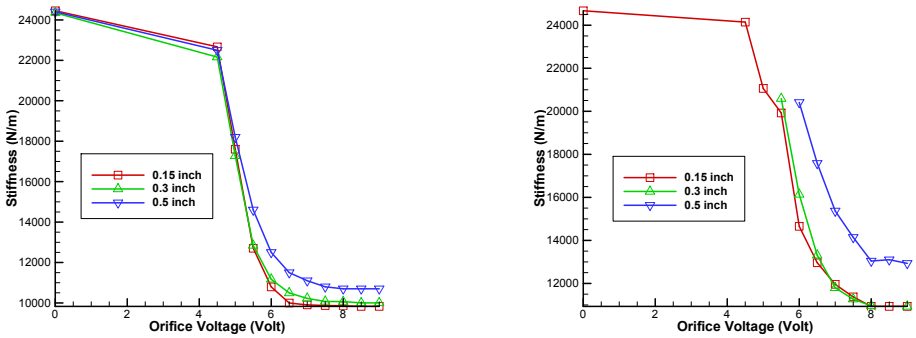

(a) 7 rad/s (b) 10 rad/s

Figure 2.11: Dynamic Stiffnesses for Various Excitations: Part 1

Figure 2.12b illustrates the K_d values for the excitation with 30 rad/s. It is not conclusive compared with the previous plots due to the high nonlinearity introduced by the large A_{mp} and f. A conclusion can be drawn that the rate of change of K_d is sharper for low A_{mp} than the one for high A_{mp}, which proves that the orifice would have very limited influence on K_d under high f.

In summary, following conclusions can be drawn with regard to dynamic stiffness of an air spring:

1: Under fixed A_{mp} and f, K_d drops with the increasing V_{in} due to the increasing air flow communication between air spring and accumulator.

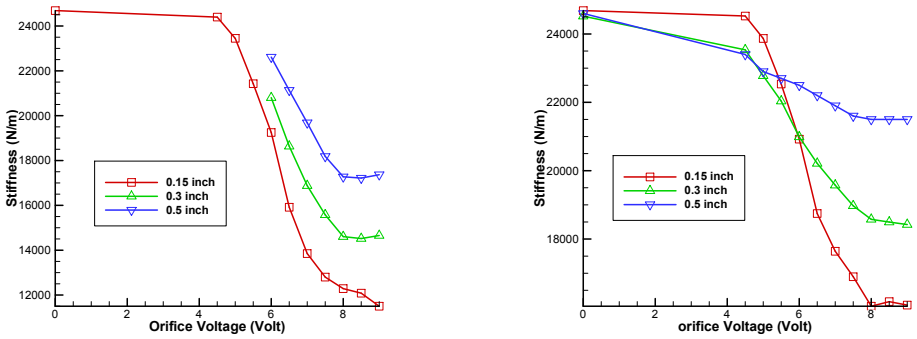

(a) 15 rad/s (b) 30 rad/s

Figure 2.12: Dynamic Stiffnesses for Various Excitations: Part 2

2: Under fixed A_{mp} and V_{in}, K_d increases with the increasing excitation frequency f because limited flow would pass through the orifice under a high f excitation.

3: Under fixed f and V_{in}, K_d increases with the increasing A_{mp}. However, under a high frequency such as 30 rad/s, the result is inconclusive due to the high nonlinearity involved in this case.

4: When f is equal to 30 rad/s, the rate of change of K_d for low A_{mp} is steeper than the one for high A_{mp}. A conclusion can be drawn that controlling the orifice would have very limited influence on K_d when A_{mp} is high.

5: When f is far away from the resonant frequency, K_d fluctuates between two static stiffness values, 9300 N/m for the closed valve and 25000 N/m for the open valve. However, when f approaches the resonant frequency area (10 rad/s or 15 rad/s) and the excitation amplitude is large, 0.3 inch or 0.5 inch, K_d seems to exceed the static stiffness value, 25000 N/m. The reason is that the adibatic process assumption is not accurate under large vibration amplitudes.

2.4 Summary

All of the theoretical and experimental studies discussed above are based on the condition that P_{s0} is 71.2 psi. In reality, in the cases such as pneumatic suspensions for seats, users usually like to adjust the air spring pressure to a level based on their individual habit. Therefore,

it is necessary to include the pressure information in the study. Rather than repeating the experimental study under multiple pressures, system-identification techniques are explored in chapter 4, and the experimental study was performed when the initial pressure of pneumatic suspension system was 84.2 psi. For maintaining the consistency between the results obtained in this chapter with the later chapters, the experimental tests were performed with the air spring static stiffness at P_{s0}=84.2 psi, and the results are shown in Fig. 2.13.

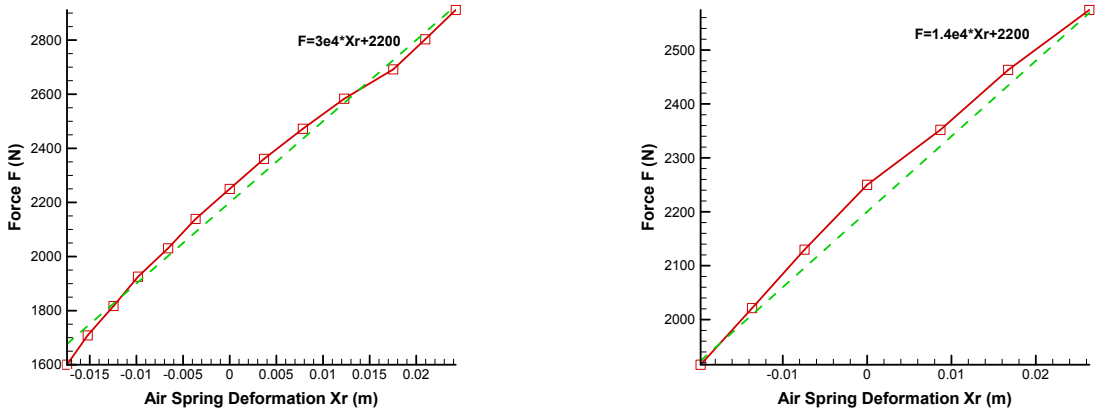

(a) Closed Valve

(b) Open Valve

Figure 2.13: Static Stiffness Values with P_{s0}=84.2 psi

In summary, this chapter presented analytical development of static spring stiffness along with validation using experimental results. A close correlation was found between the theoretical and experimental values. To assess the dynamic stiffness value K_d, multiple experiments were performed based on different combinations of the orifice voltage, excitation amplitude and excitation frequency. It was determined that K_d values depend on the orifice voltage, excitation amplitude and frequency.

CHAPTER 3. Nonlinear Modeling of the Pneumatic Suspension System

The previous chapter discussed the stiffness characteristics of a typical air spring when used in the pneumatic suspension system comprising of air spring-accumulator combination. Having explored both - static and dynamic - stiffness characteristics of the spring this chapter is focused on development of a complete nonlinear dynamic model of the pneumatic suspension system. The objective here is to obtain a nonlinear analytical model of the system which then can be used in response analysis and controller design. The modeling work presented in this chapter is motivated by the previous research work (39), which also has addressed nonlinear modeling aspect of pneumatic suspensions. The difference in the model presented in (39) and the one in this chapter is the improvement in the fidelity of the model by accounting for the effect of orifice dynamics, excitation amplitudes, and frequencies. The effect of orifice dynamics on the system's dynamic behavior is captured through a set of tuning factors K_{cr} and K_{amp} which were tuned for different combinations of excitation amplitude and frequency. A nonlinear model developed accounts for thermodynamic and fluid dynamics phenomena that occur during a typical operation of the suspension system. The modeling effort also included extensive experimental testing to determine force-displacement relationship for various test configurations and validating values of K_{cr} and K_{amp}. Finally, some concluding remarks are given at the end of the chapter.

3.1 Nonlinear Modeling

A concept of control volume is used to assist in determining the energy transfer phenomena in the dynamic behavior of the system. In thermodynamics, a control volume is defined as a fixed region in a space where one studies the masses and energies crossing the boundaries of

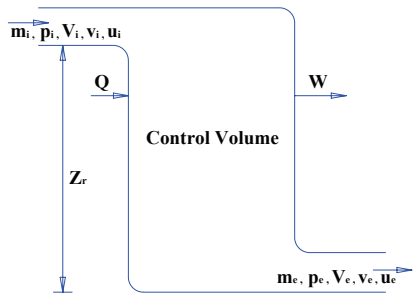

Figure 3.1: Diagram of a Control Volume

the region, as shown in Fig. 3.1. The first law of thermodynamics for a control volume could be described as follows,

$$\frac{dE_{c.v.}}{dt} = \frac{dQ}{dt} - \frac{dW}{dt} - (u_e + P_e V_e + \frac{v_e^2}{2})\dot{m}_e + (u_i + P_i V_i + \frac{v_i^2}{2} + gZ_r)\dot{m}_i \tag{3.1}$$

where,

$E_{c.v.}$: Energy inside the control volume;

Q: Heat entering the control volume;

W: Work generated by the control volume;

u_e: Internal energy at the exit area of control volume;

u_i: Internal energy at the inlet area of control volume;

v_e: Velocity of air flow at the exit area of control volume;

v_i: Velocity of air flow at the inlet area of control volume;

P_e: Pressure of the air at the exit area of control volume;

P_i: Pressure of the air at the inlet area of control volume;

V_e: Volume of the unit mass air at the exit area of control volume;

V_i: Volume of the unit mass air at the inlet area of control volume;

g: Gravity;

Z_r: Height of inlet area of control volume with the exit area as ground;

$\dot{m}_e$: Air mass flow rate exit the accumulator;

$\dot{m}_i$: Air mass flow rate at the inlet of the accumulator.

The modeling procedure is divided into several small parts for simplicity of development. The first part is to describe the filling process from air spring to the accumulator. To build a simplified and accurate model, several assumptions were made as follows,

1: Steady state flow inside the system;

2: No heat exchange and work input or output for the control volume;

3: Temperature is equal everywhere of the control volume;

4: The potential energy and kinetic energy of the air flow is disregarded.

The accumulator can be considered as the control volume in this study. Q and W are zero because no outside heat source and no work is done by the accumulator. $(u_e + P_e V_e + \frac{v_e^2}{2})\dot{m}_e$ of Eq. (3.1) is zero because the accumulator does not have exit air flow during filling process. $\frac{v_i^2}{2} + gZ_r$ is zero because the potential and kinetic energy of the air flow is disregarded. Based on the above, Eq. (3.1) can be rearranged as the equation,

$$\dot{E}_{c.v.} = (u_i + P_i V_i)\dot{m}_i \tag{3.2}$$

and,

$$\dot{m}_r C_v T = \dot{m}_i C_p T \tag{3.3}$$

where,

$\dot{m}_r$: Air mass flow rate of the accumulator;

C_v: Specific heat capacity of gas at constant volume conditions;

C_p: Specific heat capacity of gas at constant pressure conditions.

$$\dot{m}_i = \frac{\dot{m}_r}{\gamma} \tag{3.4}$$

where,

$\gamma = \frac{C_p}{C_v}$: Heat capacity ratio.

$$\dot{P}_r V_r = \dot{m}_r R T \tag{3.5}$$

where,

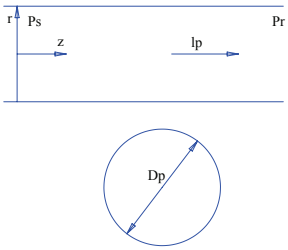

Figure 3.2: Diagram of Pipe Flow

P_r: Absolute pressure of accumulator;

V_r: Accumulator volume;

R: Specific gas constant of air;

T: Absolute temperature during the test.

The pipe flow diagram is shown in Fig. 3.2. The dynamic equation of pipe flow can be derived based on the Hegan-Poiseuille flow Eq. (3.6) with the assumptions as follows,

1. Steady state flow inside the pipe;
2. Flow is incompressible;
3. No body force;
4. No radial velocity of the air flow.

$$v_2 = -\frac{1}{4\mu}\frac{dP}{dz}(R_p^2 - r^2) \tag{3.6}$$

The mass flow rate can be calculated as,

$$\dot{m}_i = \int \rho v_2 dA = 2\pi \int_0^{R_p} \frac{-\rho}{4\mu}\frac{dP}{dz}(R_p^2 - r^2) r dr \tag{3.7}$$

where,

v_2: Mass flow velocity inside the pipe;

μ : Dynamic viscosity at fixed temperature;

R_p: Radius of the pipe;

r: Distance from the flow layer to the center axis of the pipe;

ρ: Density of the air flow.

With the assumption that the pressure drop is constant along the axial direction, the pressure varying rate can be expressed as equation,

$$\frac{dP}{dz} = \frac{P_r - P_s}{l_p} \tag{3.8}$$

where,

l_p: Length of the pipe;

P_s: Pressure of the air spring.

By combining Eqs. (3.5), (3.7) and (3.8), the rate of change of air mass flow inside the pipe can be illustrated as,

$$\dot{m}_i = -\rho \frac{\pi D_p^4}{128\mu} \frac{P_r - P_s}{l_p} = \frac{\dot{P}_r V_r}{\gamma R T} \tag{3.9}$$

where,

D_p: Diameter of the pipe.

By equalizing the Eqs. (3.7) and (3.9), the rate of change of the accumulator pressure can be expressed as,

$$\dot{P}_r = \frac{-\rho R T}{V_r} r C_r (P_r - P_s) \tag{3.10}$$

$$C_r = \frac{K_{cr} \pi D_p^4}{128 \mu l_p} \tag{3.11}$$

where,

C_r: Air flow coefficient of the pipe;

K_{cr}: Tuning factor for the orifice mechanism.

To build a simplified model without the complexity introduced by the orifice, a tuning factor K_{cr} is employed to adjust the rate of change of P_r, and would iteratively adjust the rate of change of P_s. The values for K_{cr} would be tuned by matching the simulated P_s with the experimental P_s for multiple operating conditions.

Based on the ideal gas law, we could get,

$$P = \rho RT \tag{3.12}$$

$$P = \frac{P_r + P_s}{2} \tag{3.13}$$

By combining the Eqs. (3.10), (3.12), and (3.13), the rate of change of P_r can be obtained as,

$$\dot{P}_r = \frac{-rC_r}{2V_r}(P_r^2 - P_s^2) \tag{3.14}$$

Since the derivation of the model is based on a very small deformation of the air spring from its steady state, the temperature of the whole pneumatic suspension system is assumed to be a constant value. By deriving Eq. (3.12), the rate of change of the air density inside the air spring is expressed as,

$$\dot{\rho}_s = \frac{\dot{P}_s}{RT} \tag{3.15}$$

Since the mass flow rate of the air in the air spring is contributed by the density change of the air and the volume change of the air spring, the mass flow rate coming out from the air spring can be expressed by,

$$\dot{m}_s = -\dot{\rho}_s V_s - \dot{V}_s \rho_s \tag{3.16}$$

where,

$\dot{m}_s$: Mass flow rate of the air spring;

V_s: Volume of the air spring.

By combining Eqs. (3.15) and (3.16), the rate of change of P_s is given by,

$$\dot{P}_s = -\dot{m}_s \frac{RT}{V_s} - \dot{V}_s \frac{P_s}{V_s} \tag{3.17}$$

By using the same procedures for deriving the Eq. (3.17), the rate of change of P_r is given as,

$$\dot{P}_r = \dot{m}\frac{RT}{V_r} \tag{3.18}$$

$\dot{V}_r$ does not appear in Eq. (3.18) because V_r is always at a constant value. The load an air spring can carry is simply given by,

$$F = (P_s - P_a)A_{eff} \tag{3.19}$$

By combining Newton's second law and Eq. (3.19), the air spring force equation is written as,

$$m_s\ddot{X}_s + m_s g = (P_s - P_a)A_{eff} \tag{3.20}$$

By taking the derivative of both sides of Eq. (3.20), we get,

$$m_s\dddot{X}_s = \dot{P}_s A_{eff} + (P_s - P_a)\dot{A}_{eff} \tag{3.21}$$

where, P_s is the absolute pressure inside the air spring, P_a is the ambient pressure, and A_{eff} is the effective area of the air spring.

By combining the Eqs. (3.17) and (3.18), the rate of change of P_s is given as follows,

$$\dot{P}_s = -\dot{P}_r\frac{V_r}{V_s} - \dot{V}_s\frac{P_s}{V_s} \tag{3.22}$$

It is difficult to get the rate of change of A_{eff} and V_s theoretically, but it is relatively easy to experimentally identify the rate of change of A_{eff} and V_s with respect to X_r, the rate of change of air spring effective area and volume could be written as,

$$\dot{A}_{eff} = \frac{dA_{eff}}{dX_r}\frac{dX_r}{dt} = \frac{dA_{eff}}{dX_r}v_{rd} \tag{3.23}$$

$$\dot{V}_s = \frac{dV_s}{dX_r}\frac{dX_r}{dt} = \frac{dV_s}{dX_r}v_{rd} \tag{3.24}$$

Where, v_{rd} is the relative velocity between the sprung mass and the base. By combining the Eqs. (3.14), (3.21), (3.22), (3.23), and (3.24), a set of equations is developed to describe the pneumatic suspension system as follows,

$$\begin{cases} \dot{P}_r = \frac{-rC_r}{2V_r}(P_r^2 - P_s^2) \\ \dot{P}_s = -\dot{P}_r \frac{V_r}{V_s} - \frac{P_s}{V_s}\frac{dV_s}{dX_r} v_{rd} \\ m_s \ddot{X}_s = \dot{P}_s A_{eff} + (P_{sg})\frac{dA_{eff}}{dX_r} v_{rd} \end{cases} \tag{3.25}$$

Please note that the above nonlinear model of pneumatic suspension system includes K_{cr} based on Eq. (3.11), the coefficient to represent the influence of the rate of change of pressure by solenoid orifice. In terms of K_{amp}, it is not included into the nonlinear model directly but will be the gain for excitation in the simulink model. Both the K_{cr} and K_{amp} will be tuned for each test case.

3.2 Validation of the Nonlinear Model for Pneumatic Suspension System

An extensive experimental testing was conducted to validate the values of K_{cr} and K_{amp} for each test case. The values were tuned by matching the simulation and experimental plots of P_s Vs X_r. The flow chart of the simulation study is shown in Fig. 3.3. The simulation model, built by Matlab Simulink, consists of three blocks to represent three equations of the equation set (3.25). The system input is the sinusoidal excitation with multiple amplitudes and frequencies, defined by X_d and f respectively. Three different sinusoidal excitations (Low: 0.15 inch; Medium: 0.3 inch; and High: 0.5 inch) and several excitation frequencies (7 rad/s; 10 rad/s; 15 rad/s; and 30 rad/s) were used in the tests. The system outputs, P_s, P_r, and X_s, iteratively enter the system dynamics. Besides X_d and f, the orifice input voltage, V_{in}, would influence the system dynamics because it changes the air communication between the air spring and accumulator. Therefore, the simulation study was performed based on the multiple combinations of X_d, f, and V_{in}, which is varied from 4.5 volts to 9 volts with 0.5 volt increment. The initial parameter values used in the simulation study are summarized in Table 3.1.

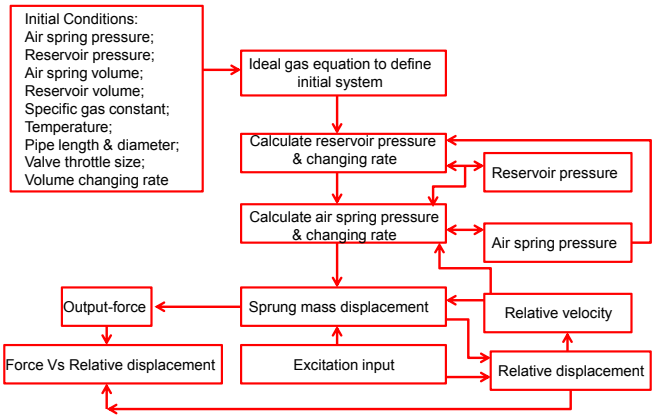

Figure 3.3: Flow Chart of Nonlinear Model Simulation

3.2.1 Results for K_{cr}

Figures 3.4a to 3.9b illustrate the simulation results and experimental results for P_s Vs X_r for various cases, with different combination of X_d, V_{in}, and f. The solid line and dashed line in each plot represent the simulation and experiment respectively. The experimental results are unavailable for certain cases, such as the large amplitudes with low orifice voltages, due to the aggressive vibration when the excitation frequency is close to the system resonant frequency. The tuning factor K_{cr}, shown in Eq. (3.11), is important to determine the rate of change of P_r. Therefore, the K_{cr} value for each test case was tuned by matching the simulation and experiment, and the results are shown in Figs. 3.10 to 3.12. Several conclusions can be drawn as follows,

(1): The experimental results have a good correlation with the simulation results based on tuning K_{cr} values. It proves that the derived nonlinear model accurately reflects the real dynamics of the pneumatic suspension system using tuning K_{cr} values.

(2): K_{cr} increases with the increasing V_{in}, as shown in Figs. 3.10 to 3.12. The observation is that the K_{cr} value is proportional to the rate of change of P_r, which is also proportional to the V_{in}. Therefore, K_{cr} is proportional to V_{in}. A few exceptions occur at the voltage above 8 volts, and it shows that V_{in} has limited influence on the system dynamics once it is above 8 volts.

Table 3.1: Parameter Values for Nonlinear Model Simulation

Parameter	Value	Unit	Description
A^o_{eff}	0.0058	m^2	Effective area of air spring at steady state
A_b	0.0042	m^2	The rate of change of air spring volume to the relative displacement
P^o_s	71.2	Psi	Absolute pressure of air spring at steady state
P^o_r	71.2	Psi	Absolute pressure of accumulator at steady state
V^o_r	0.0189	m^3	Volume of accumulator
V^o_s	1.33e-3	m^3	Volume of air spring at steady state
μ	0.17e-5	$kgfs/m^2$	Dynamic viscosity of air
D_p	0.0095	m	Diameter of the pipe
m_s	229.6	Kg	Sprung mass
l_o	-0.025	n/a	The rate of change of A_{eff} to X_r at steady state with opening valve
l_c	-0.0093	n/a	The rate of change of A_{eff} to X_r at steady state with closed valve
R	287.058	$JKg^{-1}K^{-1}$	Specific gas constant of air
T	293.15	K	Absolute temperature
P^o_{sg}	56.5	Psi	Gauge pressure of air spring at steady state

3.2.2 Results for K_{amp}

Table 3.2 summarizes the tuning parameter values for K_{amp} for each test case. The results show that an individual K_{amp} can be tuned with the fixed excitation amplitude and frequency. This means that the tuning K_{amp} value is independent of the orifice voltage for fixed excitation amplitude and frequency.

Table 3.2: Summary of Adjusting Parameter Values for K_{amp}

Sinusoidal Excitation (inch)	7 rad/s	10 rad/s	15 rad/s	30 rad/s
0.15	0.76	1.06	0.44	0.24
0.3	0.9	1.1	1	0.68
0.5	1.88	2.1	1.3	0.46

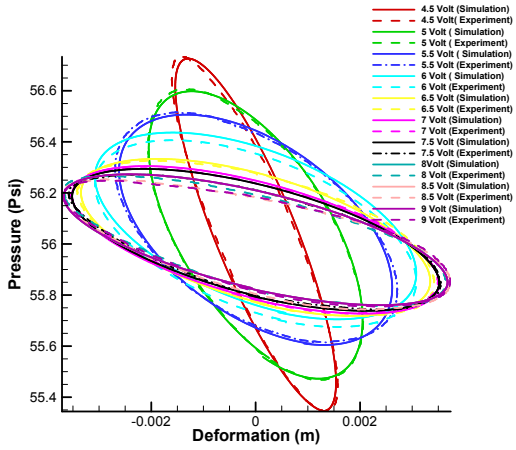

(a) 7 rad/s

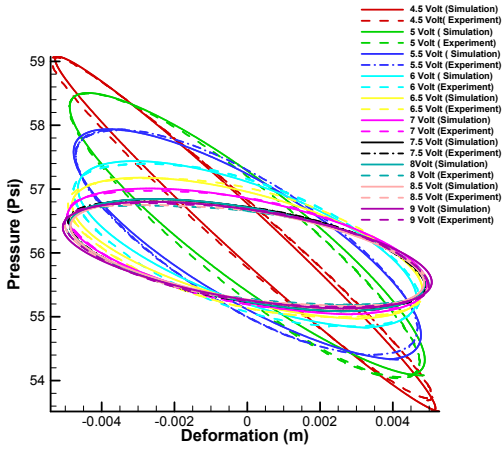

(b) 10 rad/s

Figure 3.4: Simulation Vs Experiment for 0.15 inch: 7 rad/s and 10 rad/s

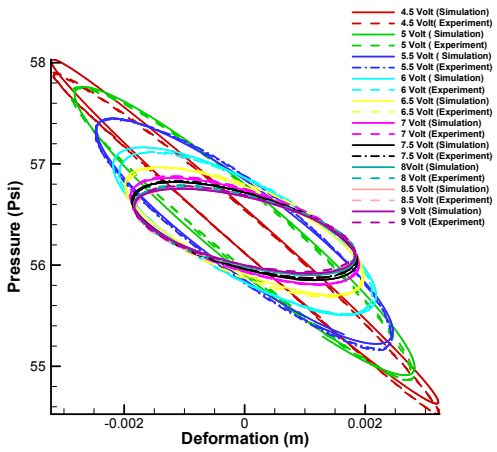

(a) 15 rad/s

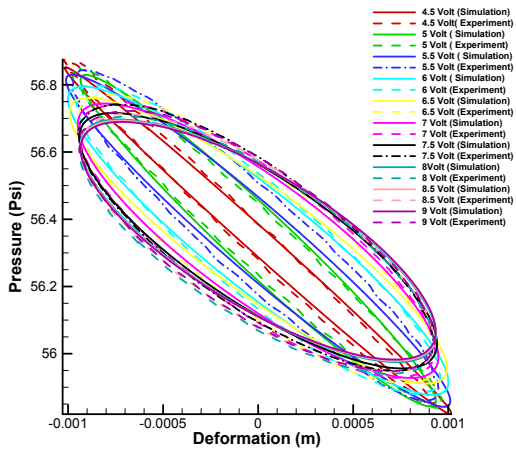

(b) 30 rad/s

Figure 3.5: Simulation Vs Experiment for 0.15 inch: 15 rad/s and 30 rad/s

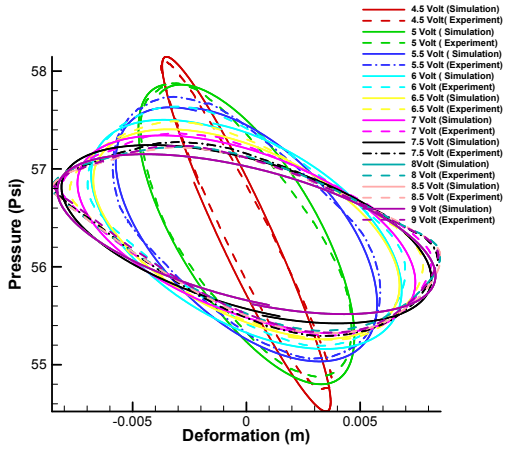

(a) 7 rad/s

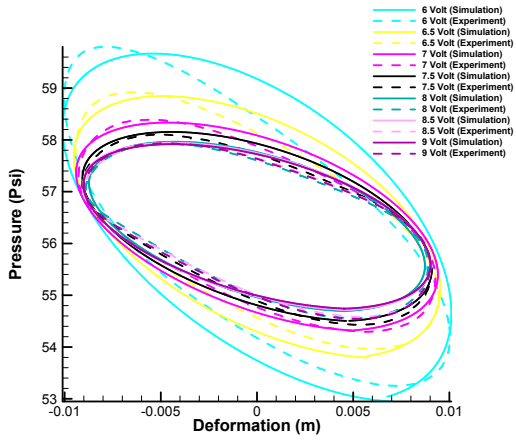

(b) 10 rad/s

Figure 3.6: Simulation Vs Experiment for 0.3 inch: 7 rad/s and 10 rad/s

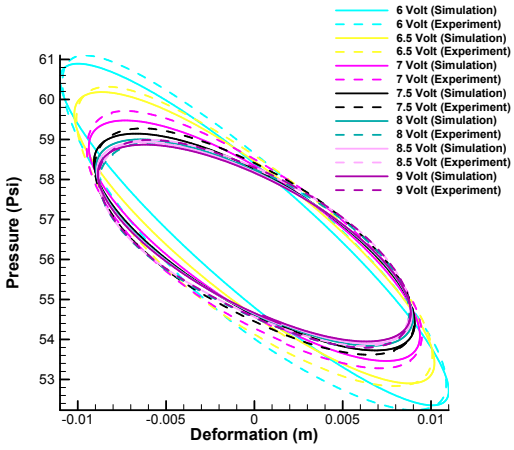

(a) 15 rad/s

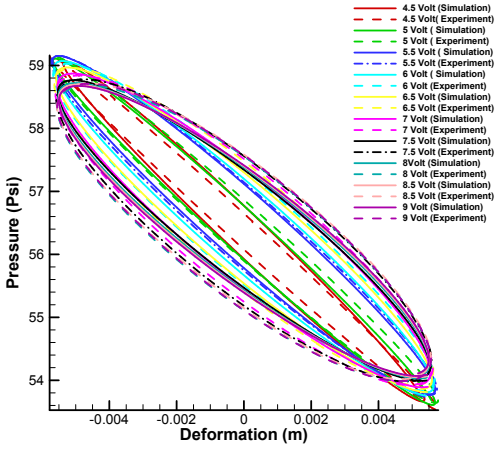

(b) 30 rad/s

Figure 3.7: Simulation Vs Experiment for 0.3 inch: 15 rad/s and 30 rad/s

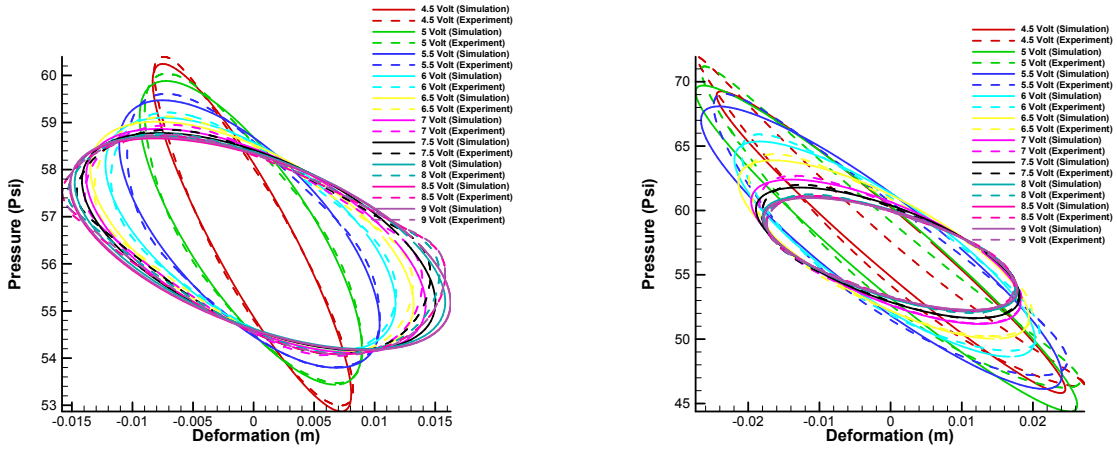

(a) 7 rad/s

(b) 10 rad/s

Figure 3.8: Simulation Vs Experiment for 0.5 inch: 7 rad/s and 10 rad/s

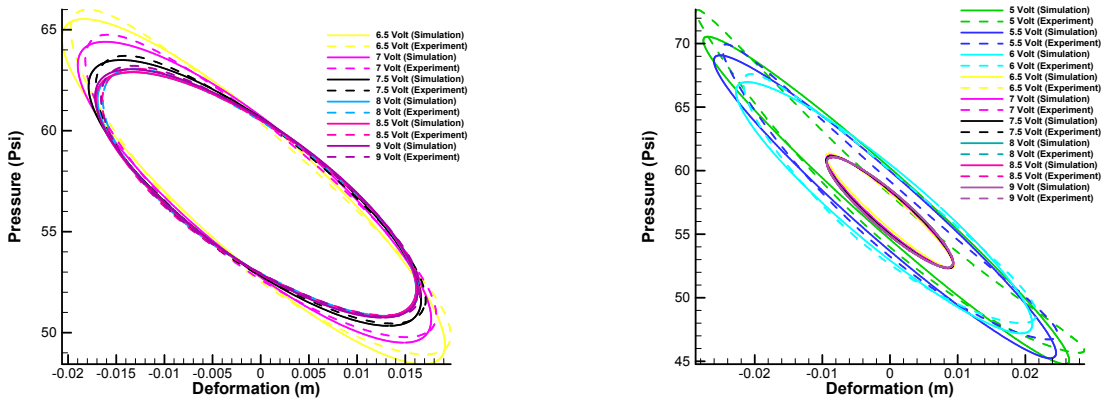

(a) 15 rad/s

(b) 30 rad/s

Figure 3.9: Simulation Vs Experiment for 0.5 inch: 15 rad/s and 30 rad/s

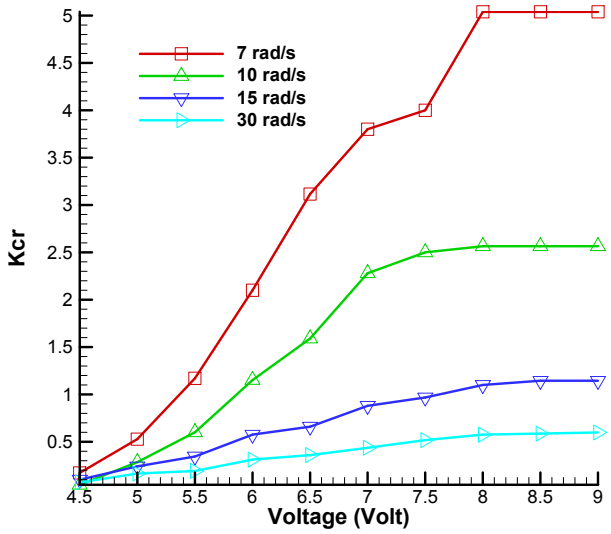

Figure 3.10: Kcr Vs Orifice Voltage for 0.15 inch

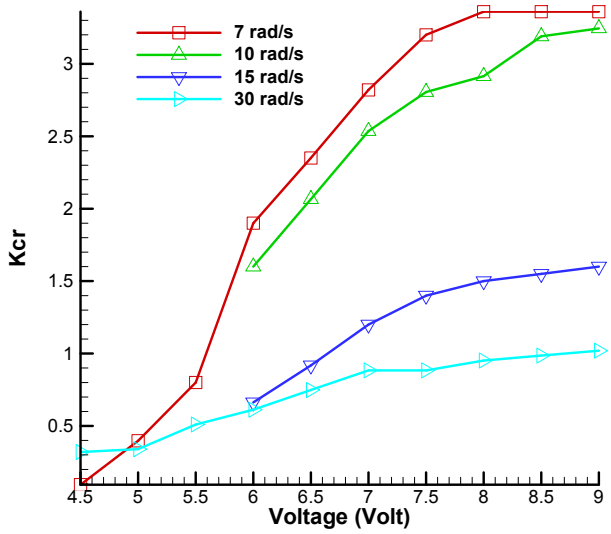

Figure 3.11: Kcr Vs Orifice Voltage for 0.3 inch

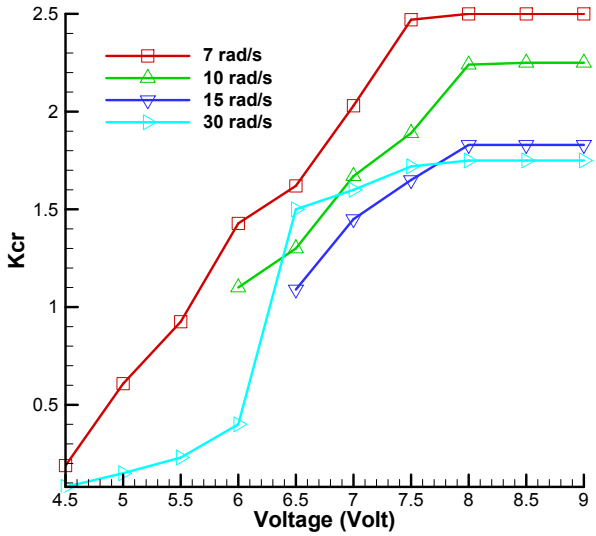

Figure 3.12: Kcr Vs Orifice Voltage for 0.5 inch

3.3 Linearized Model of the Pneumatic Suspension System

The above development showed that use of tuning factors K_{cr} and K_{amp} for each test case, allows one to predict the nonlinear dynamic behavior of the suspension system fairly accurately. This nonlinear model can now be used as "true plant model" in simulation studies. For controller design, however, one needs to obtain linearized version of this model since there are far more control design tools available for linear systems than nonlinear systems. In case the controller design based on linear model does not perform to the satisfactory level one can try to use multiple controller designs or seek nonlinear control design tools. By using the same procedures in (39), one could linearize the model and get the transfer function descriptions as shown in Eqs. (3.26) and (3.27) respectively. The linearization was performed around the operator point, which is selected as the steady state of the air spring being at the nominal height. The parameters with the superscript "o" means the parameter values at the operator

point.

$$K(S) = \frac{F(S)}{X_r(S)} = \frac{\frac{-A^o_{eff}A_bP^o_s + l_oP^o_{sg}V^o_s}{V^o_s}S + \frac{N(l_oP^o_{sg}(V^o_s+V_r) - A^o_{eff}A_bP^o_s)}{V^o_s}}{S + \frac{N(V^o_s+V_r)}{V^o_s}} \tag{3.26}$$

$$T(S) = \frac{X_s(S)}{X_d(S)} = \frac{T_n(S)}{T_d(S)} \tag{3.27}$$

where,

$T_n(S) = (A^o_{eff}A_bP^o_s - l_oP^o_{sg}V^o_s)S + A^o_{eff}A_bP^o_sN - l_oP^o_{sg}N(V^o_s + V_r)$;

$T_d(S) = m_sV^o_sS^3 + m_sN(V^o_s+V_r)S^2 + (A^o_{eff}A_bP^o_s - l_oP^o_{sg}V^o_s)S + A^o_{eff}A_bP^o_sN - l_oP^o_{sg}N(V^o_s + V_r)$;

and, $N = \frac{rC_r}{V_r}P^o_s$.

To evaluate the linearized model, several case studies for different stiffnesses were performed. Figure 3.13 illustrates the results of the case study with tuning K_{cr} as 1.8 at a 0.15 inch sinusoidal excitation and 6 volt orifice voltage. Although there are some differences between the experimental stiffness values and the stiffness values of the linearized model, the results show that the stiffness of the linearized model increases as the increasing excitation frequency. The stiffness study was also extended to other cases such as 0.3 inch and 0.5 inch excitation amplitudes as shown in Figs. 3.14 and 3.15. The results show the stiffness of the linearized model increases as the increasing excitation frequency, which follows the same trend as the experimental results. Moreover, a good correlation was found at large excitation frequency cases such as 15 rad/s and 30 rad/s.

The overall system's Bode plots for a linearized model are presented for 0.3 inch case. Figure 3.16a shows the Bode plots for the linearized model with K_{cr} along with the experimental Bode plots. Please notice that the experimental Bode plots were obtained by the system-id method, which will be discussed in the chapter 4. The peak magnitude frequencies of the Bode plots for the linearized model shift as the orifice voltage varies. However, a large amount of differences are observed between the magnitudes of the experimental Bode plots and the ones for the linearized model Bode plots due to the ignorance of K_{amp} during the linearization. Because K_{amp} is the gain of the excitation amplitude used in the simulation study, it cannot be

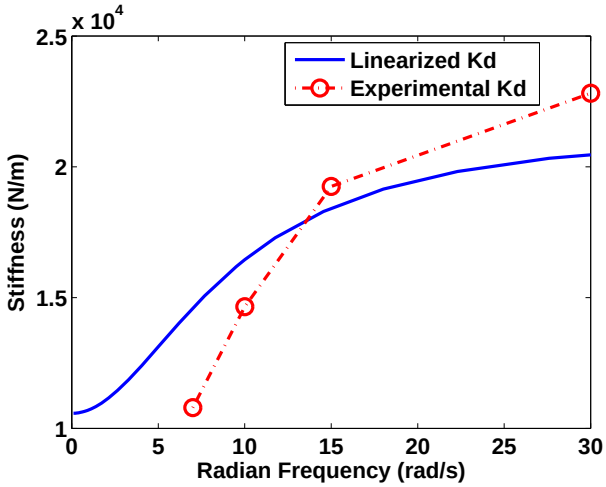

Figure 3.13: Stiffness at 0.15 inch, 6 volt and Kcr=1.8

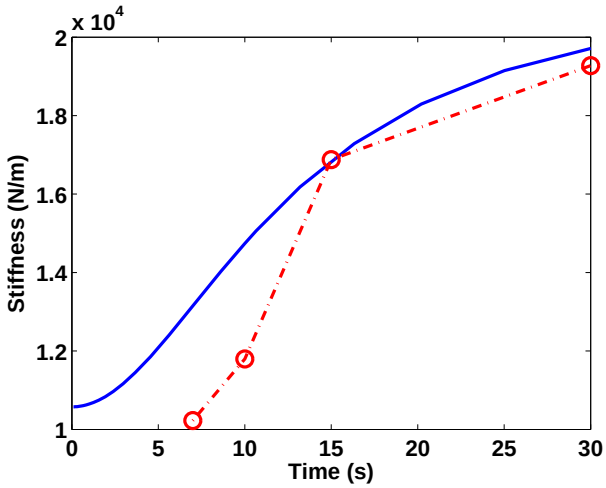

Figure 3.14: Stiffness at 0.3 inch, 7 volt and Kcr=2.5

directly included in the linearized model. Therefore, we tune other physical parameter values like air spring volume to represent the influence of K_{amp}. By tuning the parameter value for each test case, a new set of Bode plots of the linearized model was obtained to match the experimental results, and the results are shown in Fig. 3.16b.

3.4 Summary

By tuning the values for K_{cr} and K_{amp}, a good correlation was achieved between the P_s of the nonlinear model and the experimental P_s. This means that the pneumatic suspension

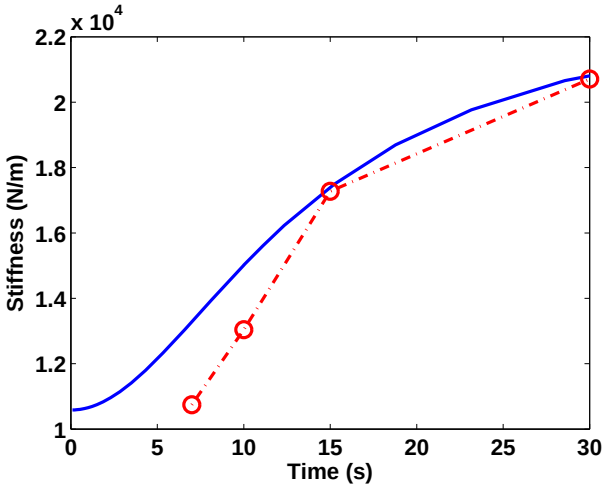

Figure 3.15: Stiffness at 0.5 inch, 8 volt and Kcr=2.3

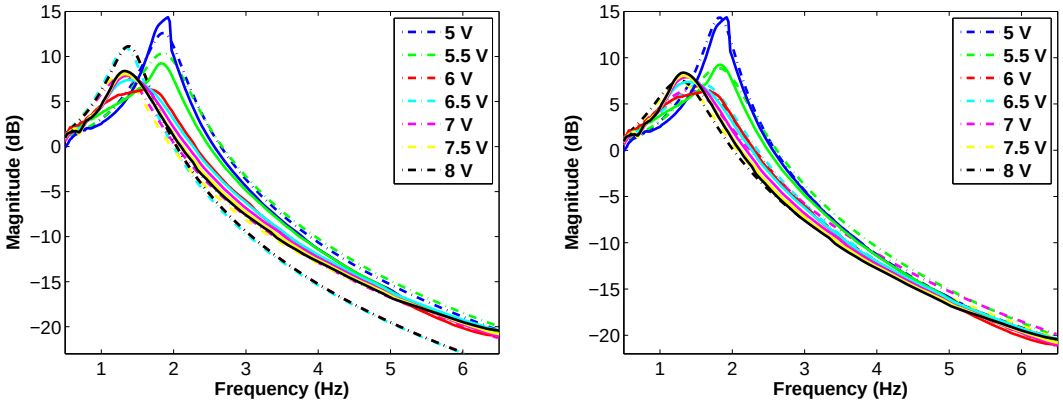

(a) Tuing K_{cr} only (b) Tuning K_{cr} and Other Parameters

Figure 3.16: Bode Plots (Simulation Vs Experiment)

system with the solenoid orifice under consideration could be described fairly accurately by the derived nonlinear model with tuned K_{cr} and K_{amp} values for each test case. The advantage of this method is to avoid the integration issues when combing the air spring model with the complicated orifice model. However, the limitation for this method is that the parameters have to be tuned for every excitation source and orifice voltage. The linearization study was performed and the results show that K_{amp} is an important parameter to correlate the analytical model with the experimental data. However, since it is challenging to include K_{amp} in the nonlinear model and its linearized model, a control-oriented model is desired and will be the topic for chapter 4.

CHAPTER 4. Experimental Set-up and System Identification

4.1 Introduction

A system identification methodology used here is the frequency domain method wherein dynamic system under consideration is excited with the sine wave signal with varying frequencies and corresponding sinusoidal output signal is recorded. Then a set of sinusoidal input and output signal pairs for varying frequencies is used to obtain Bode plots of the system. These Bode plots are then used to identify the transfer function that relates the input and output of the system.

4.2 Laboratory Facility and Experimental Testing

This section is devoted to describing the laboratory set-up designed and custom-built for conducting experimental research in the pneumatic suspension system. The proof-of-concept pneumatic suspension system is used to validate the analytical model predictions and performance of closed-loop system for candidate controller designs.

4.2.1 Experimental Test Rig

Figure 4.1 shows the experimental test rig designed and built in-house for experimental work. The main components of the test rig are described below:

- A computer-controlled hydraulic shaker system, shown by Fig. 4.2, consisting of a 4-way servo valve (MOOG G761-3005), a servo cylinder (Vickers TY01DAEAE), a gear pump (Haldex G20D2V17T1A1A61R), and an oil filter system (Mp Filtri FMP1352S AG-5A03HK82). A user defined disturbance or ride file input obtained from field testing can be given to the servo cylinder to emulate a real-life disturbance.

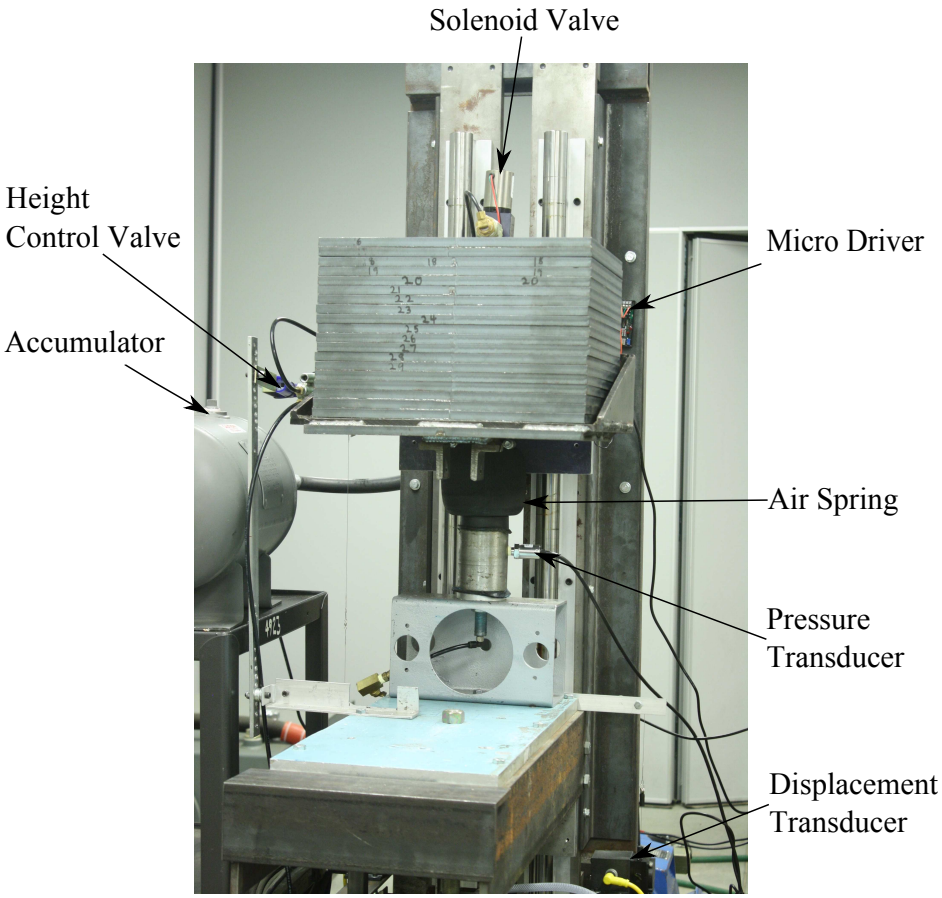

Figure 4.1: Pneumatic Suspension Test Rig

Figure 4.2: Pneumatic Suspension Shaker

- A set of vertical guides is used to constrain the motion of the suspended mass in the vertical plane and to prohibit lateral as well as longitudinal motion.

- A rectangular carrier assembly holds steel plates (dead weight) to emulate the sprung mass. The carrier is constrained to move only vertically through linear bearings mounted on vertical guides using pillow blocks. The total weight of the carrier and the plates used in the experiments is around 506 lbs.

- A sleeve type air spring (Firestone 1102-0074) whose nominal design height is 4 inches and the operating range is $\pm$ 2 inch from the nominal position. The maximum allowable pressure for the air spring without reducing its life cycle is 125 psi.

- A solenoid valve (IQ Valves 203319). The orifice size is adjusted from 0 inch to 0.375 inch. During the test, the given voltage is from 5 volts to 8 volts. The maximum operating pressure for the valve is 120 psi.

- A micro driver associated with the solenoid valve (IQ Valves B5950-10001) which controls the valve.

- Accumulator, also called reservoir, consists of a 5 gallon volume accumulator and a 47 inch length PVC pipe to connect the accumulator to the air spring via the solenoid valve.

- A height control valve which is only used to adjust the initial height of the air spring and the valve was closed during the test. Therefore, the dynamics of height control valve lies outside of the operational range of the air spring-accumulator system and hence is not accounted for in the model.

- A Stanford spectrum analyzer, which is shown in Fig. 4.3 and is used to send the swept sine wave to the shaker for the frequency response data of the pneumatic suspension system.

- A D-Space 1105 Dspace controller board, which is used to send all sensor information to the computer by the A/D channels (shown in Fig. 4.4).

- Two position transducers (Celesco Transducer PT1DC-10-UP-M0P0-MC4), which are used to measure the displacement of the sprung mass and the base. The sensitivity of the position transducers is 0.2 volt/inch.

- A pressure transducer (Measurement Specialties MSP-300-250-P-4-N-1), which is used to measure the air spring pressure during the stiffness test in chapter 2 and 3. The sensitivity of the pressure sensors is 0.016 volt/psi.

Figure 4.3: Stanford Spectrum Analyzer

Figure 4.4: 1105 Dspace Board

4.2.2 System Identification

The test rig described above was used as the focus configuration for modeling. The system identification technique was used to extract mathematical models from experimental test data. The dynamic models were obtained for various combinations of excitation amplitudes, X_d, and orifice input voltages, V_{in}. The system identification test procedure is described below.

1. A Stanford research spectrum analyzer was used to generate the sinusoidal excitation signals. The excitation amplitudes X_d was varied from 0.2 inch to 0.7 inch with 0.1 inch

interval, and the sweeping frequency was varied from 0.5 Hz to 6.5 Hz.

2. The solenoid voltage V_{in} was kept fixed at a value between 5 volts and 8 volts with 0.25 volt increments. Since the orifice opening level is controlled by the applied voltage, an orifice input voltage corresponds to an orifice opening level.

3. Data was collected for X_s and X_d using the position transducers. The data could not be collected corresponding to the cases when the excitation frequencies resonated with that of the natural frequency of the system and the levels of amplitude exceeded certain value as the system oscillations became violent and the test run had to be aborted. For all other cases the data was collected for X_s and X_d values.

4. The system-id toolbox, SOCIT, developed at NASA LaRC based on Eigensystem Realization Algorithm was used to extract the transfer function model from the frequency response data.

4.2.3 System Identification Test Results

In total, the data was collected for 63 different combinations of voltage inputs (or equivalent orifice openings) and excitation input amplitudes. The test results are explained in the following two categories,

1. **Fixed Excitation Input Case**

Figures 4.5a to 4.7b give magnitude plots and phase plots for three fixed excitation input cases, 0.2 inch, 0.4 inch, and 0.6 inch. Each figure includes the results for V_{in}, from 5 volts to 8 volts with 0.25 volt increment. The solid line in each figure represents the experimental frequency response data, and the dashed line represents the system-id result. As mentioned above, the frequency response data for some large excitation input at some small orifice voltage like 5 volts is unavailable due to the excessive vibration. Specifically, when V_{in} is less than 6 volts, the orifice opening size is too small to get much air flow from the accumulator when the excitation frequency is close to its natural frequency. Therefore, it is not possible to collect the system frequency response data for the test cases at a large X_d but a small V_{in}. For instance, 0.6 inch excitation with 5 volts orifice. As seen from Fig. 4.7a, the data is collected starting from 6 volts instead of 5 volts.

Figures 4.5a, 4.6a, and 4.7a represent the magnitude plots for fixed excitation input cases. All of those plots show the shift of peak magnitude frequency, ω_n, according to different orifice input voltages. Generally ω_n reduces as the increasing V_{in} and vice versa. Although ω_n shifts for all of the test cases, the shifting level for a large excitation input, i.e. 0.6 inch, is not as much as the one for a small excitation amplitude, for example 0.4 inch. Besides ω_n, V_{in} also influences the system damping level, indicated by ζ. However, the variance level of ζ for large excitation input, 0.6 inch, is smaller than that for small excitation inputs, 0.2 inch or 0.4 inch. Therefore, a conclusion could be drawn that the varying orifice voltage has greater effects on the small excitation input than it does for large excitation amplitudes.

Figures 4.5b, 4.6b, and 4.7b illustrate the phase plots of fixed excitation input cases. The phase plots are almost independent of the orifice voltage, especially at the large excitation case like 0.6 inch.

2. **Fixed Orifice Voltage Input Case**

Similar as the above fixed excitation input case, Figs. 4.8a to 4.10b are the magnitude plots and phase plots for the cases of fixed orifice input voltage, from 6 volts to 8 volts with 0.5 volt increments. The solid line in each plot represents the experimental data, and the dashed line represents the system-id result. The displacement data were collected from 0.2 inch to 0.7 inch with 0.1 inch increment except when orifice voltage is 6 volt, Again, the data was not collected for 0.7 inch excitation amplitude due to the excessive vibration.

Figures 4.8a, 4.9a, and 4.10a illustrate the magnitude plots for the fixed orifice input cases. Similar to the fixed excitation input cases, both the system natural frequency, ω_n, and damping ratio ζ change as the excitation input amplitude is varied. However, the effects of excitation input on the system dynamics for small orifice voltage, i.e. 6 volts, is much greater than the ones for large orifice voltage, i.e. 8 volts. It means the system has larger controllability for small orifice voltage cases than for large orifice voltage cases.

Figures 4.8b, 4.9b, and 4.10b illustrate the phase plots of fixed excitation input cases. The phase plots are almost independent to the orifice voltage, especially at the large orifice voltage case like 8 volt. Some mismatch are observed for the cases such as small orifice voltages or small excitation amplitudes.

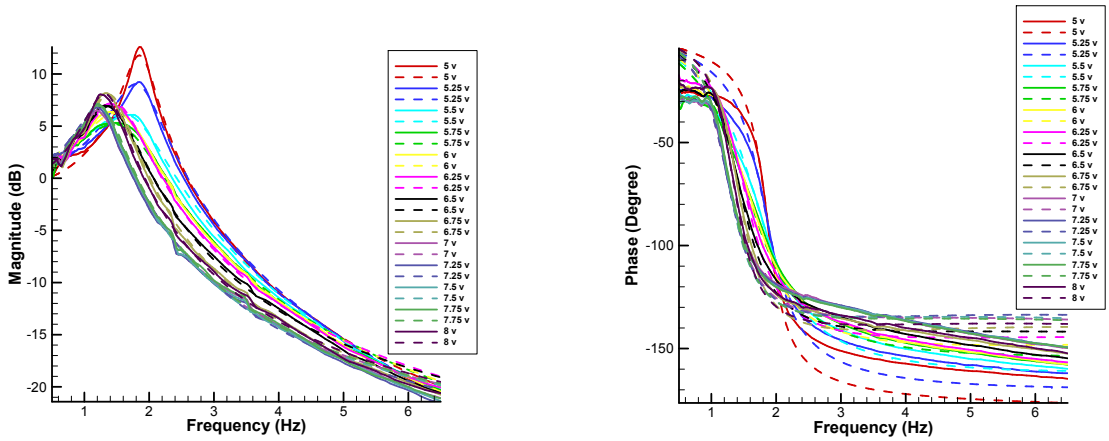

(a) Magnitude Plots (b) Phase Plots

Figure 4.5: Bode Plots for Various Orifice Voltages (0.2 inch)

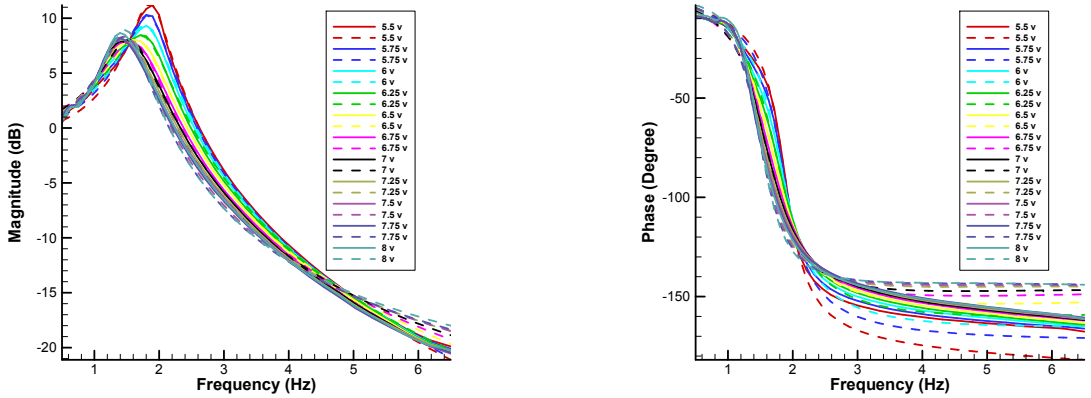

(a) Magnitude Plots (b) Phase Plots

Figure 4.6: Bode Plots for Various Orifice Voltages (0.4 inch)

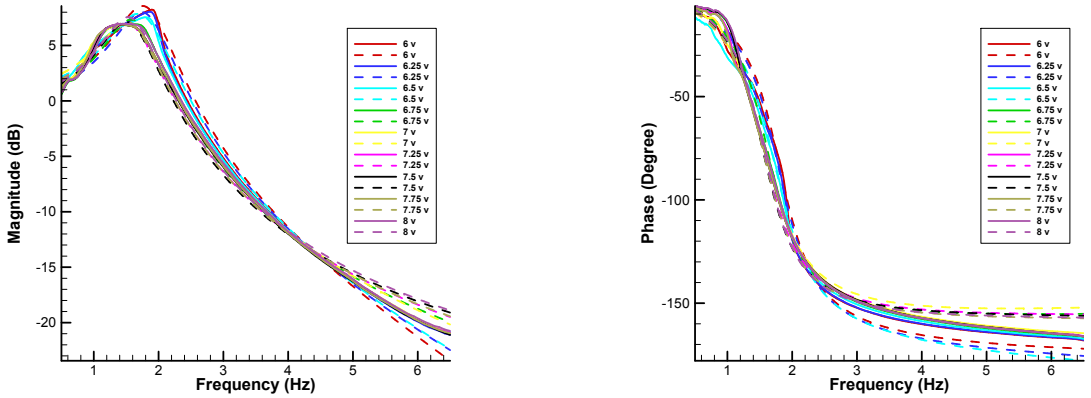

(a) Magnitude Plots (b) Phase Plots

Figure 4.7: Bode Plots for Various Orifice Voltages (0.6 inch)

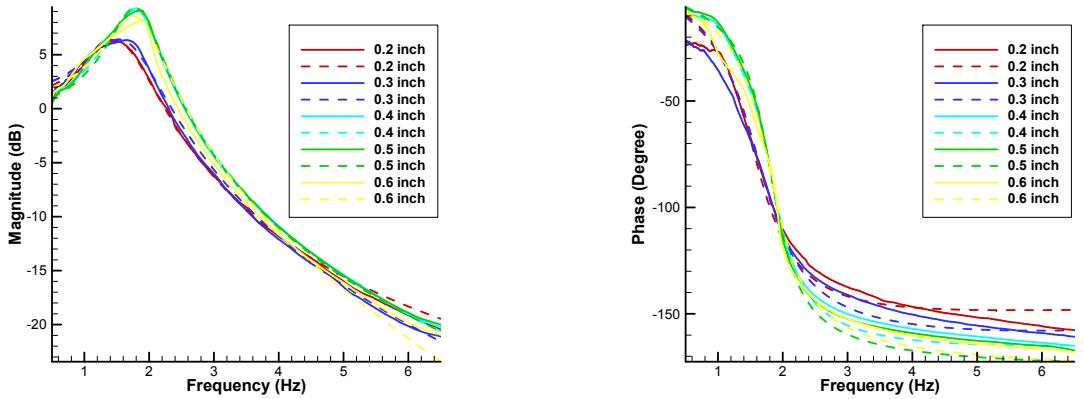

(a) Magnitude Plots (b) Phase Plots

Figure 4.8: Bode Plots for Various Disturbance Amplitudes (6 volt)

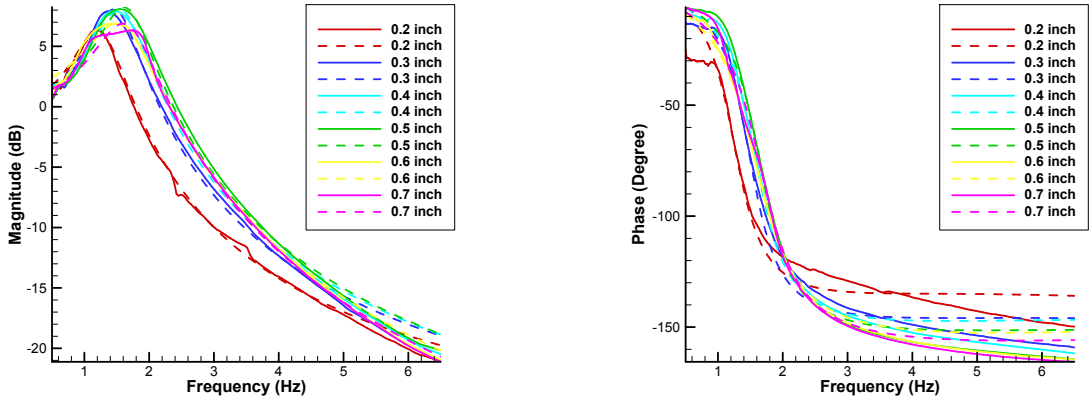

(a) Magnitude Plots (b) Phase Plots

Figure 4.9: Bode Plots for Various Disturbance Amplitudes (7 volt)

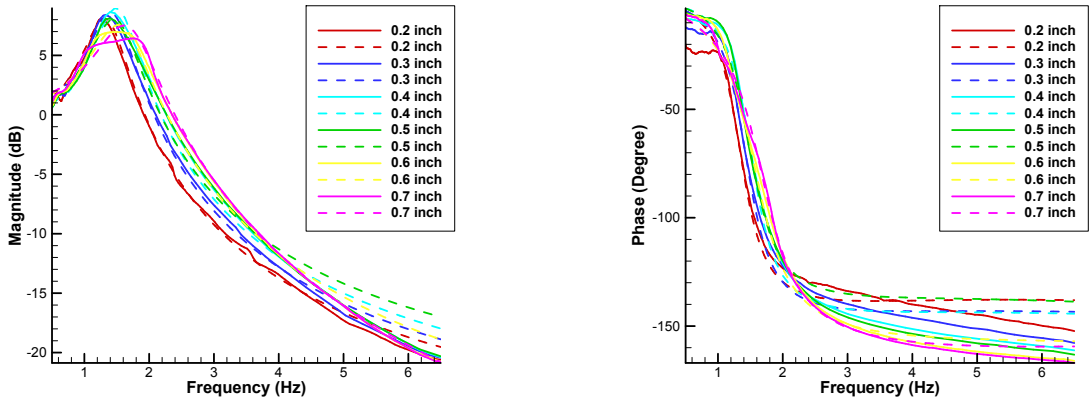

(a) Magnitude Plots (b) Phase Plots

Figure 4.10: Bode Plots for Various Disturbance Amplitudes (8 volt)

3. **Summary**

Figure 4.11 is the overall plot for ω_n for tests with various combinations of X_d and V_{in}. The results illustrate that ω_n decreases with the increasing V_{in}, but it increases with the increasing X_d. The result is reasonable: while fixing the excitation input, a large orifice voltage would allow a large amount of air to pass through the solenoid valve. As noted previously, the system stiffness, K, reduces as the increasing air spring volume. ω_n is proportional to the square root of the system stiffness, K, because ω_n is equal to $\sqrt{\frac{K}{M}}$. Finally, ω_n decreases with the increasing V_{in}. While observing the Fig. 4.11 for fixed orifice voltage case, the conclusion could be made that ω_n increases with the increasing X_d. For the fixed orifice input voltage, although the increasing excitation input can allow increased air communication to reduce ω_n, the large excitation itself seems to dominate over the effects of the increasing air communication level, and finally ω_n is increased with the increasing excitation input, which is also observed by the dynamic stiffness test in chapter 3. The only exception is 0.2 inch excitation input with less than 5.5 volts orifice voltage. Without the help of the large excitation amplitudes, the orifice opening is too small to have air flow pass through it. The air spring's bag forces dominate the response. Therefore, the ω_n is unable to follow the overall natural frequency trend of the system.

Figure 4.12 represents the results for the damping ratio ζ of a second order system for all of the test cases. It can be seen that ζ depends on the excitation input and the orifice input voltage. A large bandwidth of ζ is observed at the cases with small excitation amplitudes and low orifice voltages, for example, the bandwidth of ζ is from .09 to .32 for 0.3 inch excitation amplitude when the orifice voltage is less than or equal to 6 volts. The damping bandwidth got much squeezed for large amplitudes or high orifice voltage input. For instance, the damping ratio for 0.7 inch excitation amplitude is limited within 0.22 to 0.28.

4.3 Simple Analytical Model of the Pneumatic Suspension System

The system identification technique was used to obtain linear dynamic model for the experimental system under consideration. This section is devoted to the development of linear analytical model which can be used to compare with system-id model. The analytical model

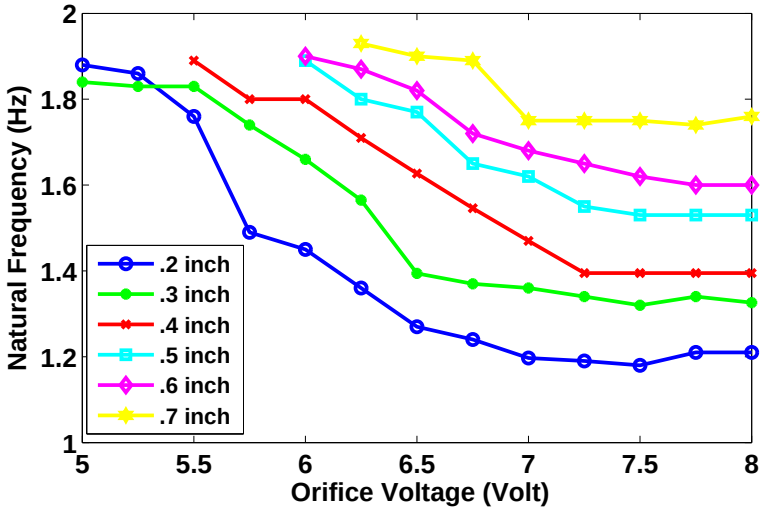

Figure 4.11: Natural Frequencies of System-ID Models

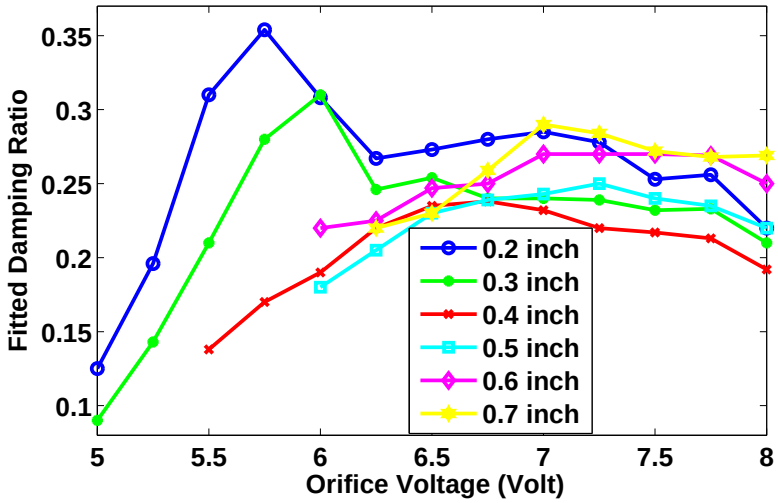

Figure 4.12: Damping Ratios of System-ID Models

can be tuned based on system-id models.

Considering a schematic of air spring-accumulator configuration shown in Figure 4.13(A) The system consisting of the base (unsprung mass), suspended mass (sprung mass), air spring, accumulator, and orifice which controls the air mass flow between the air spring and accumulator. Figure 4.13(B) shows a simplified schematic with associated system parameters. The parameters and variables of the system are as follows,

M: Sprung Mass; C: Damping Coefficient; K: Air Spring Stiffness; X_s: Sprung Mass Displacement; X_d: Base Displacement; F_d: Controllable Force.

The system damping is achieved by using a sharp-edged orifice mechanism even though the system does not have traditional damper (48). The controllable force F_d ,shown in the schematics, is the control input to model the force generated by adjusting orifice control mechanism, which consists of the damping injected into the system and the force due to the stiffness variance. The damping performance of the pneumatic suspension system depends on the quantity and rate of air mass exchange between the air spring and the accumulator, which is adjusted by the orifice mechanism. The orifice opening is controlled by its input voltage. Since the control input F_d does not enter into the dynamics in affine manner, it was approximated through the fictitious damper element.

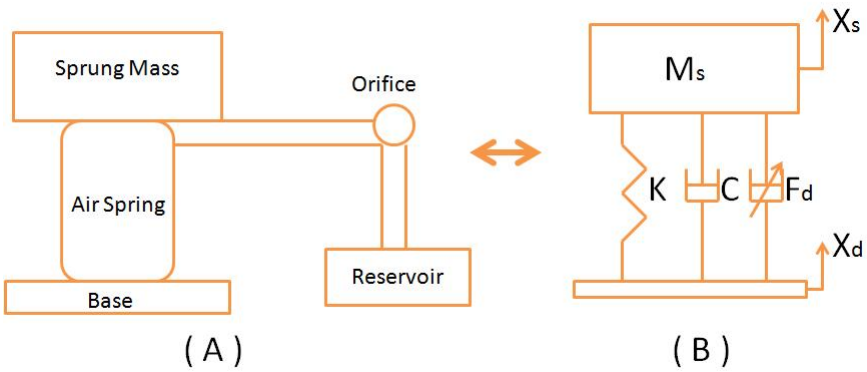

Figure 4.13: Schematics of the Pneumatic Suspension System

The governing dynamic equation of the system of Fig. 4.13 can be given as,

$$M\ddot{X}_s + C(\dot{X}_s - \dot{X}_d) + K(X_s - X_d) + F_d = 0 \tag{4.1}$$

Defining $X = [X_1, X_2]'$, where $X_1 = X_s$, $X_2 = \dot{X}_s - \frac{C}{M}F_d$, and $Y = X_s$, the state space

representation of Eq. (4.1) can be given as,

$$\dot{X} = AX + B_d X_d + B_f F_d \tag{4.2}$$

$$Y = CX + D_d X_d + D_f F_d \tag{4.3}$$

where,

$$A = \begin{bmatrix} 0 & 1 \\ -K/M & -C/M \end{bmatrix}, B_d = \begin{bmatrix} C/M \\ K/M - C^2/M^2 \end{bmatrix}, B_f = \begin{bmatrix} 0 \\ -1/M \end{bmatrix}$$

and,

$$C = \begin{bmatrix} 1 & 0 \end{bmatrix}, D_d = \begin{bmatrix} 0 \end{bmatrix}, D_f = \begin{bmatrix} 0 \end{bmatrix}$$

The Eq. (4.1) can be re-written in another form as follows,

$$M\ddot{X}_s + C\dot{X}_s + KX_s = C\dot{X}_d + KX_d - F_d \tag{4.4}$$

From Eq. (4.4) and treating X_d and F_d as two different inputs, and the transfer functions can be given as,

$$\frac{X_{sd}(s)}{X_d(s)} = \frac{Cs/M + K/M}{s^2 + Cs/M + K/M} \tag{4.5}$$

$$\frac{X_{sf}(s)}{F_d(s)} = \frac{-1/M}{s^2 + Cs/M + K/M} \tag{4.6}$$

where, $X_s(s)$=$X_{sd}(s)$+$X_{sf}(s)$;

$X_{sd}(s)$:$X_s(s)$ contributed from $X_d(s)$;

$X_{sf}(s)$:$X_s(s)$ contributed from $F_d(s)$.

Given a sinusoidal excitation as: X_d= X_0 $sin(\omega t)$, the sinusoidal transfer function of Eq. (4.5) can be given as,

$$\frac{X_{sd}(j\omega)}{X_d(j\omega)} = \frac{Cj\omega/M + K/M}{-\omega^2 + Cj\omega/M + K/M} \tag{4.7}$$

Based on Eq. (4.7), the following terms could be introduced,

$\omega_n = \sqrt{\frac{K}{M}}$: Undamped Natural Frequency;

$\zeta = \frac{C}{2\sqrt{MK}}$: Damping Ratio.

Equations (4.5) to (4.7) can be compared with the transfer functions obtained using system-id techniques and the unknown parameters (natural frequency and damping) could be determined.

4.4 Verification of the System-ID Models

In general there was a good correlation observed between the experimental data and the identified models. Some mismatch was observed especially at the large excitation amplitude cases.

Since the identified models are obtained from the data in frequency domain, another check was done by examining the response in the time domain. Both of the step responses and sinusoidal responses were examined for validation. For step response, Figs. 4.14a and 4.14b respectively represent the experimental and simulated step responses with 0.3 inch (0.0076 m) and 0.4 inch (0.0106 m) amplitude. The orifice voltage was given as 5 volts and 6 volts for each case. The simulations matched the experiments very well except the slight differences in the system settling time. The reason is that the identified models disregard the damping generated by bag forces. Figures 4.15a and 4.15b show results for 0.4 inch and 0.6 inch cases for 8 volts orifice voltage, illustrating that the agreement between two responses is reduced with the increasing orifice voltage, and the reason is due to the high nonlinearity coming from the large air flow.

Another type of transient response examined was the sinusoidal response. Figures 4.16a and 4.16b represent experimental as well as analytical sinusoidal responses for the 0.4 inch excitation input. The orifice voltage was 6.5 volts and 8 volts. The results for 6.5 volts have a better correlation between simulation and experiment than the one for 8 volts case, which illustrate the identified model could represent the system well at low orifice voltage cases.

The above frequency response plots and transient response plots show that the identified model generally represent the real system dynamics.

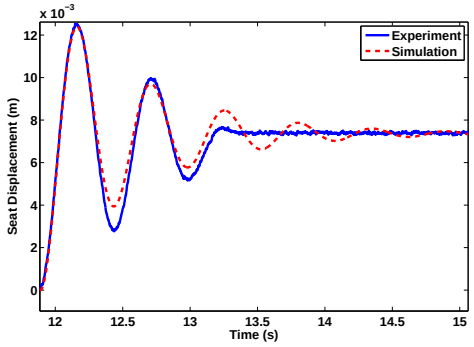

(a) 0.3 inch and 5 volt

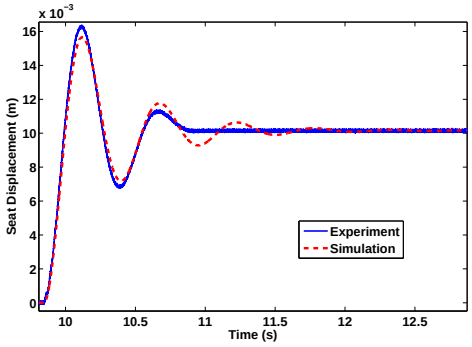

(b) 0.4 inch and 6 volt

Figure 4.14: Step Responses (Experiment Vs Simulation): Part 1

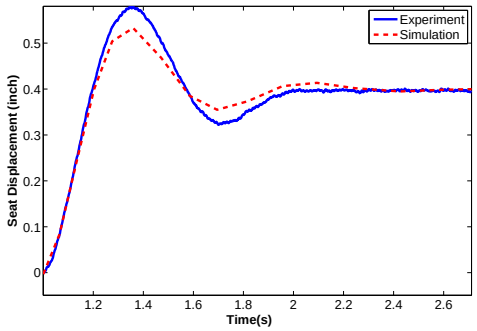

(a) .4 inch and 8 volt

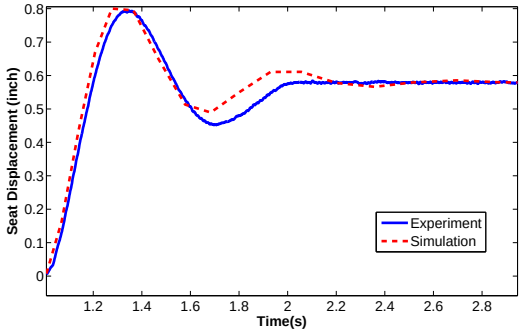

(b) 0.58 inch and 5 volt

Figure 4.15: Step Responses (Experiment Vs Simulation): Part 2

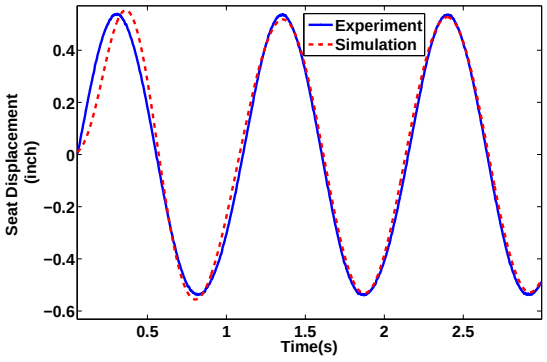

(a) 0.4 inch and 6.5 volt

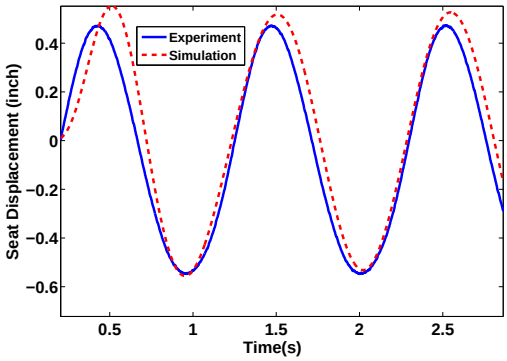

(b) 0.4 inch and 8 volt

Figure 4.16: Sinusoidal Responses (Experiment Vs Simulation)

CHAPTER 5. H-Infinity Controller Design for Pneumatic Suspension System

The last two chapters focused on modeling aspects of the pneumatic suspension system. Both analytical as well as system identification models were developed. The analytical modeling included nonlinear as well as linear approximation of the system dynamics whereas the identified model using experimental frequency response data was constrained to be linear.

This chapter will focus on controller design, specifically the H-infinity controller, for pneumatic system under consideration using linear models. The control design will be implemented on laboratory set-up to evaluate the controller performance. The control actuator of the pneumatic suspension system is a solenoid operated orifice mechanism to control the in and out flow of air mass between the air spring and accumulator. The layout of the chapter is as follows: First, some background is given for H-infinity control design followed by the detailed design process for the controller design and closed-loop simulations and analysis.

5.1 H-Infinity Robust Controller Design

The first step of the controller design is to obtain a model that is simple enough to facilitate the controller design while capturing the critical dynamic characteristics at the same time. The strategy used for controller design was to use a simplified linear model for controller design and use uncertainty model to capture unmodeled dynamics (i.e., the difference between linear model and true nonlinear model) to the extent possible. It is a typical approach used in robust control designs. Figure 5.1 gives a block diagram of the feedback control system under consideration. The system output, sprung mass displacement X_s, consists of two parts: X_{sf} and X_{sd}, defined as the partial output generated by controlling force F_d and excitation input X_d separately. The

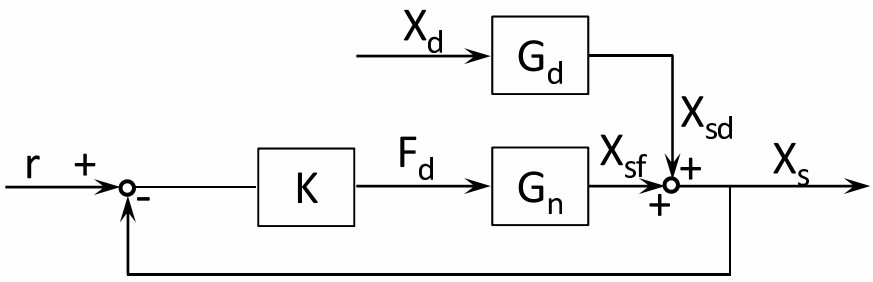

Figure 5.1: Feedback Control System

transfer functions relating X_d and F_d to X_{sd} and X_{sf} were given in Eqs. (4.5) and (4.6) of chapter 4 respectively.

The objective of the controller design is to minimize the system output X_s in the desired frequency range, between 1 Hz to 10 Hz, which is perceived to be the most sensitive frequency range for humans (54). The controllable input, F_d, is the force generated by the system's adjustable damping and natural frequency, which is controlled by varying the solenoid orifice input voltage. Therefore, the pneumatic suspension system uses the control strategy by adjusting the solenoid orifice opening based on the differential signal, between reference r and measured X_s. The reference signal r is set to zero to minimize X_s in this study.

According to Fig. 5.1, the plant output is written as Eq. (5.1), and it can be rearranged as Eq. (5.2) for a SISO system. In that case, the closed-loop response is given as Eq. (5.3), and the controllable error, e=r-y, is written as Eq. (5.4).

$$y = X_s = G_n(s)F_d + G_d(s)X_d \tag{5.1}$$

$$y = G_nK(r - y) + G_dX_d \tag{5.2}$$

$$y = (1 + G_nK)^{-1}G_nKr + (1 + G_nK)^{-1}G_dX_d \tag{5.3}$$

$$e = (1 + L)^{-1}r - (1 + L)^{-1}G_dX_d = Sr - SG_dX_d \tag{5.4}$$

where,

$(1 + G_nK)^{-1}$: sensitivity function S ;

$(1 + G_nK)^{-1}G_nK$: complementary sensitivity function T;

G_nK: loop transfer function L;

In Eq. (5.3), S is the closed-loop transfer function between the output disturbance to the output, and T is the closed-loop transfer function from the reference signal to the output. The addition of S and T is always equal to 1. Obviously, a small S leads to a small error between the reference signal and the measured output, which is what is desired for the control.

For H-infinity controller design, the diagram of Fig. 5.1 can be transformed to a well-known generalized $P - K$ configuration (55) as shown in Fig. 5.2. $W_1(s)$ and $W_2(s)$ are weighting functions on performance output X_s and control input F_d respectively. This is known as the mixed sensitivity problem. The system like Fig. 5.2 is described by a set of equations as follows,

$$Y(s) = P(s)X(s) \tag{5.5}$$

where,

$$Y(s) = \begin{bmatrix} Z_1(s) \\ Z_2(s) \\ V(s) \end{bmatrix}, \; P(s) = \begin{bmatrix} W_1(s) & -W_1(s)G_d(s) & -W_1(s)G(s) \\ 0 & 0 & W_2(s) \\ 1 & -G_d(s) & -G(s) \end{bmatrix}$$

and

$$X(s) = \begin{bmatrix} r(s) \\ w(s) \\ u(s) \end{bmatrix}$$

By defining,

$$Y_1(s) = \begin{bmatrix} Z_1(s) \\ Z_2(s) \end{bmatrix}, \; X_1(s) = \begin{bmatrix} r(s) \\ w(s) \end{bmatrix}$$

The transfer function between $Y_1(s)$ and $X_1(s)$ is the matrix,

$$P(s) = \begin{bmatrix} W_1 & -W_1SG_d \\ W_2KS & -W_2KSG_d \end{bmatrix}$$

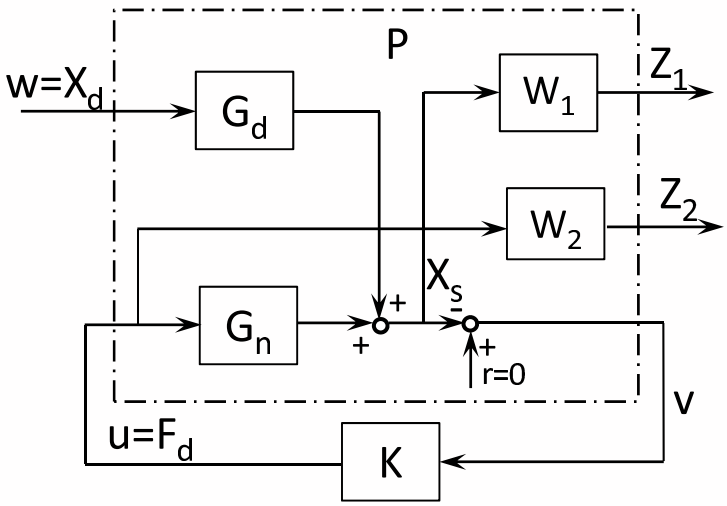

Figure 5.2: Generalized Plant and P-K Configuration (Skogestad, S and Postlethwaite, 2005)

The magnitude of the sensitivity function $|S|$ will be small at all the frequency ranges due to the waterbed effects. In particular, a stable plant must satisfy the relation as follows (55),

$$\int_0^\infty ln\,|S|\,d\omega = 0 \tag{5.6}$$

To decrease the sensitivity function S in the desired frequency range, below 10 Hz, a weighting function $W_1(s)$ has to be designed to satisfy the following condition:

$$|S| \leq |1/W_1(s)| \tag{5.7}$$

As shown above, $W_1(s)$ is designed to be a low pass filter to ensure performance in the desired frequency range. $W_2(s)$ shown below is employed as the weighting function for the control force input, and its inverse is the maximum force that the pneumatic suspension system can generate.

$$|F_d| \leq |1/W_2(s)| \tag{5.8}$$

By combining the Eqs. (5.4) and (5.5), Z_1 and Z_2 can be rewritten as follows,

$$Z_1 = W_1 e = W_1 Sr - W_1 SG_d X_d \tag{5.9}$$

$$Z_2 = W_2 F_d = W_2 K S r - W_2 K S G_d X_d \tag{5.10}$$

While keeping the control input below its saturation value, the objective of controller design is to minimize the reference tracking error for the optimal performance. That is accomplished by designing a stabilizing controller K which minimizes (5.11).

$$\left\| \begin{matrix} W_1 S & -W_1 S G_d \\ W_2 K S & -W_2 K S G_d \end{matrix} \right\|_\infty \tag{5.11}$$

5.1.1 Determination of Nominal Model G_n and Uncertainties

To design a controller K to minimize (5.11), G_n, G_d, $W_1(s)$ and $W_2(s)$ have to be determined. As shown in Fig. 5.3a, a family of system-id models was obtained experimentally to describe the system dynamics. It is observed that the peak magnitude frequency varies with orifice voltages. The reason for this phenomenon is that the varying orifice voltage changes the opening of the air spring inlet valve which in turn changes the effective air spring stiffness and therefore the natural frequency of the system. Chapter 4 has already shown that the the system natural frequency is proportional to the square root of the stiffness. Therefore, the varying orifice voltages results in the varying peak magnitude frequency observed from Fig. 5.3a. The phenomena to be observed is that as the inlet valve opening changes from being open to close there is a clear cut shift in the natural frequency. For all other openings the frequency hovers between these two extreme values. The dip in the transition region shows that the dB magnitude values are clustered together for the range of orifice openings. This is the natural frequency region where the damping is most effective. The nominal model G_n was chosen by selecting a model whose Bode plot lied somewhere in the middle of all the plots. Figure 5.3b shows an example of a good match between the experimental data and system-id fit when the orifice voltage is 6.25 volts and excitation amplitude is 0.2 inch. Based on this information and using Eq. (4.6) the nominal plant model was chosen to be

$$G_n = \frac{-1/230}{s^2 + 5.22s + 96.43} \tag{5.12}$$

Within operating range of orifice openings and excitation amplitudes, the variations from the nominal model were considered as uncertainties in the model. The uncertainty bounds were obtained using the upper and lower bounding transfer functions for all the system-id models. Figure 5.4 shows the Bode magnitude plots of the nominal model and bounding transfer functions. The upper and lower bounding transfer functions are given as follows,

$$G_u = \frac{-2.8/230}{s^2 + 5.2s + 134} \tag{5.13}$$

$$G_l = \frac{-0.75/230}{s^2 + 6s + 109.4} \tag{5.14}$$

There are several types of uncertainty description that can be used to describe system's unstructured uncertainty, modeled as additive uncertainty and multiplicative uncertainty. In this case, the multiplicative uncertainty is shown in Fig. 5.5.

$$L_{iu}(\omega) = Max_\omega \left| \frac{(G_u(j\omega) - G_n(j\omega))}{G_n(j\omega)}, \frac{(G_l(j\omega) - G_n(j\omega))}{G_n(j\omega)} \right| \tag{5.15}$$

where $L_{iu}(s)$ is given by,

$$L_{iu}(s) = \frac{0.006667s^4 + 0.06337s^3 + 1.518s^2 + 6.491s + 69.82}{0.003704s^4 + 0.03722s^3 + 0.9949s^2 + 4.514s + 54.29} \tag{5.16}$$

and the weighting function $W_i(s)$ was chosen to satisfy the relationship (5.17). The choice of $W_i(s)$ is given in Eq. (5.18).

$$|W_i(j\omega)| \geq |L_{iu}(j\omega)|, \forall\omega \tag{5.17}$$

$$W_i(s) = L_{iu}(s) \tag{5.18}$$

5.1.2 Determination of Weighting Function $W_1(s)$

Typically, the formula used for $W_1(s)$ (55) is given below:

$$W_1(s) = \frac{(s/M^{1/n} + \omega_b)^n}{(s + \omega_b A^{1/n})^n} \tag{5.19}$$

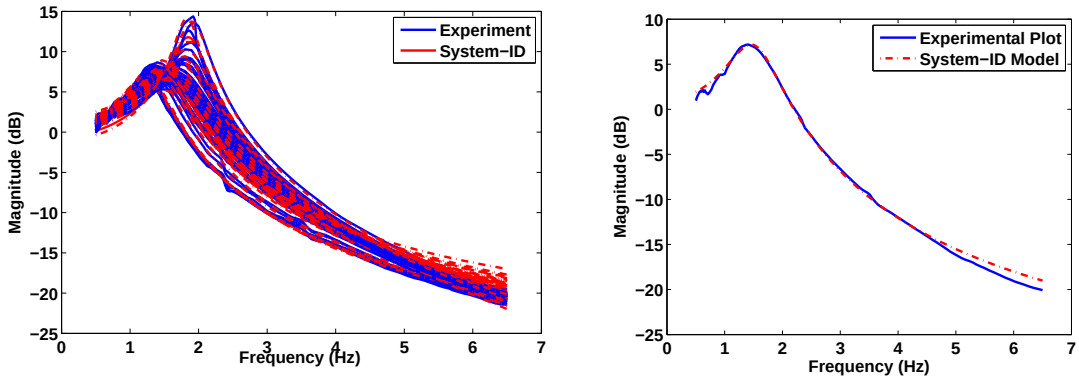

(a) Selected Cases (b) Nominal Model

Figure 5.3: Magnitude Plots of Experimental and System-ID Models

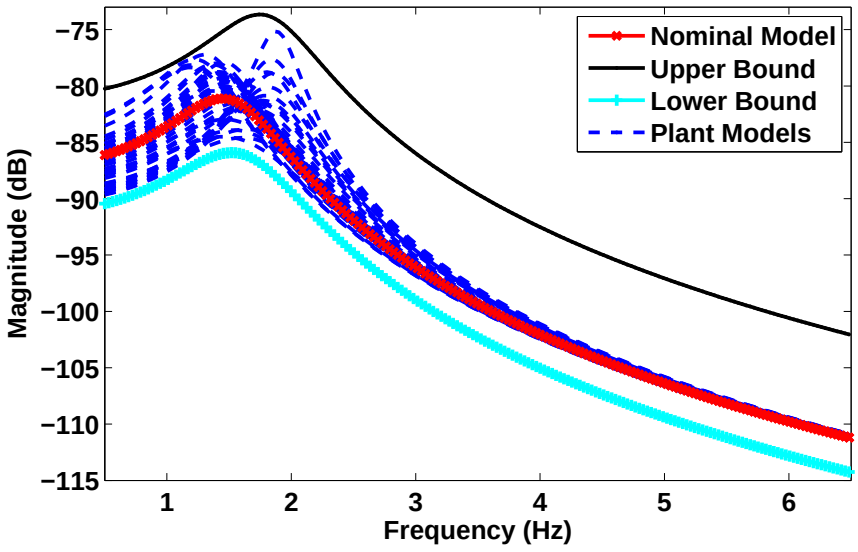

Figure 5.4: Nominal Model and Boundary Models

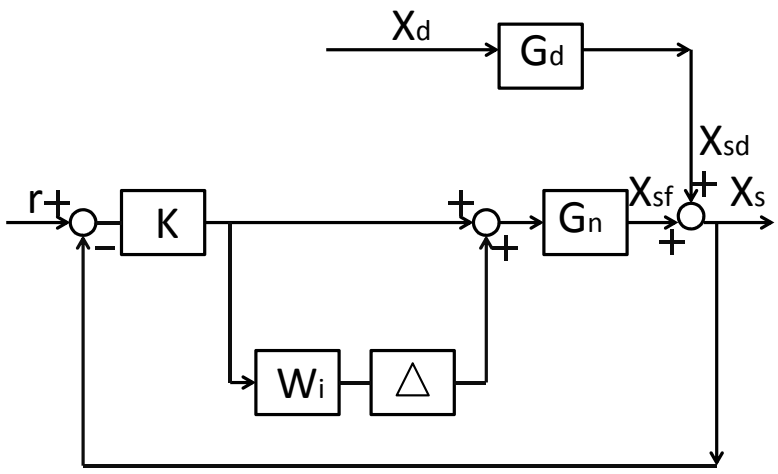

Figure 5.5: Feedback Control Diagram with Multiplicative Uncertainty (Skogestad, S and Postlethwaite, 2005)

Where, ω_b is the bandwidth requirement, M is the inverse of $W_1(s)$ at high frequencies, n is the order of weighting function, and A is the inverse of $W_1(s)$ at low frequencies. To select a suitable $W_1(s)$, a series of simulations performed with multiple weighting functions by selecting various combinations of n, M, and A. The "best" weighting function is selected by employing a set of n, M, and A which could provide the optimal vibration isolation performance, among all of the selected closed-loop cases. The order of the weighting function, n, was determined. The higher the order of the weighting function, the higher the order of the designed controller K. A controller K with high order tends to have practical issues due to the high computation requirement. In this study, the order of the weighting function was limited to 3. For fixed M and A, Figs. 5.6a to 5.6c represent the step responses for the weighting functions with order from 1 to 3. The plots show that a third order weighting function would provide the best performance among all of the cases.

The parameter values of M and A were determined after selecting n by trial and error. Beyond bandwidth frequency M could be selected to be large as we do not need to suppress the value of $|S|$ at large frequencies. In this study, M is selected as 10 for the controller design.

Similarly, in the range of bandwidth, A should be a small value since $|S|$ is desired to be a low value. However, an extremely small value of A is not preferred because it is difficult to get a solution convergent for large control force requirement. The simulation results for several trial studies are shown in Figs. 5.7a to 5.7c. A satisfactory performance was obtained for M=10 and A=0.025. An optimization study was conducted to find the value of A which would provide the optimal closed-loop performance. The range of A values selected was from 0.01 to 0.1 with 0.005 as the increment.

$$X_d = A_1 * sin(\omega_1 * t + \phi_1) + A_2 * sin(\omega_2 * t + \phi_2) + A_3 * sin(\omega_3 * t + \phi_3) \tag{5.20}$$

Three case studies were preformed to evaluate the closed-loop performances under multiple A values. Three sinusoidal excitations were employed to represent the low frequency, medium frequency, and high frequency disturbances, respectively. The excitations were based on the formula in Eq. (5.20) and the coefficients are listed in Table 5.1. The closed-loop performances were evaluated by the vibration isolation performance, which is calculated by dividing the RMS of the excitation by the difference between the RMS of the excitation and the RMS of the closed-loop performance. Figure 5.8 summarize the results for the simulation, and it shows that A=0.015 gives the best performance at two of the three excitation cases. Therefore, A=0.015 was used in the weighting function $W_1(s)$, which is written as,

$$W_1(s) = \frac{0.1s^3 + 40.61s^2 + 5497s + 248100}{s^3 + 46.49s^2 + 720.3s + 3721} \tag{5.21}$$

5.1.3 Determination of Weighting Function $W_2(s)$

$W_2(s)$ is defined as the inverse of the maximum force generated by adjusting the solenoid valve. To be specific, the control force can be considered as a manifestation of the variation of the system damping and natural frequency. For a second order system, the damping force is represented as follows,

$$f = 2\zeta\omega_n M(\dot{X}_s - \dot{X}_d) \tag{5.22}$$

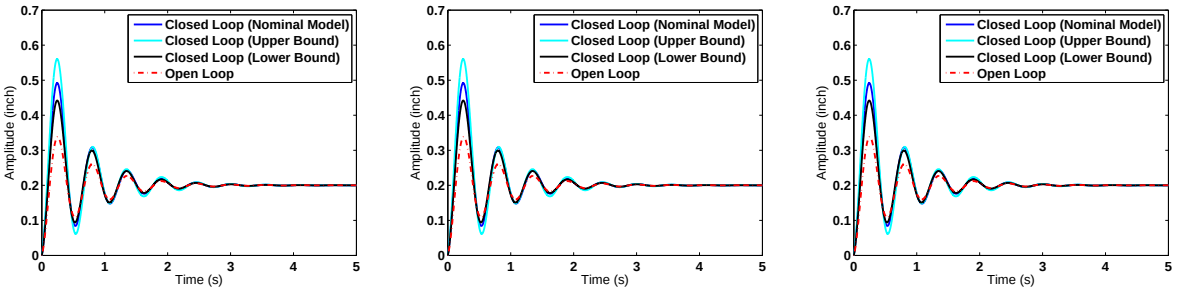

(a) 1st Order (b) 2nd Order (c) 3rd Order

Figure 5.6: Step Response Plots for the Weighting Functions with Various Orders

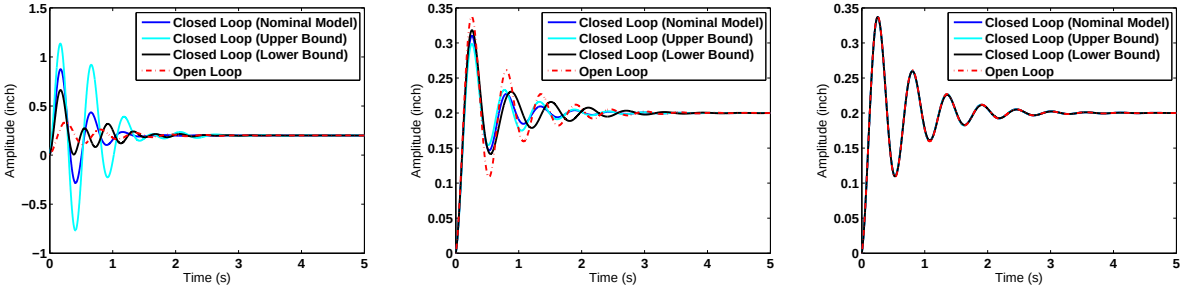

(a) M=10, A=0.005 (b) M=10, A=0.025 (c) M=10, A=0.25

Figure 5.7: Step Response Plots for the Weighting Functions with Multiple M and A Values

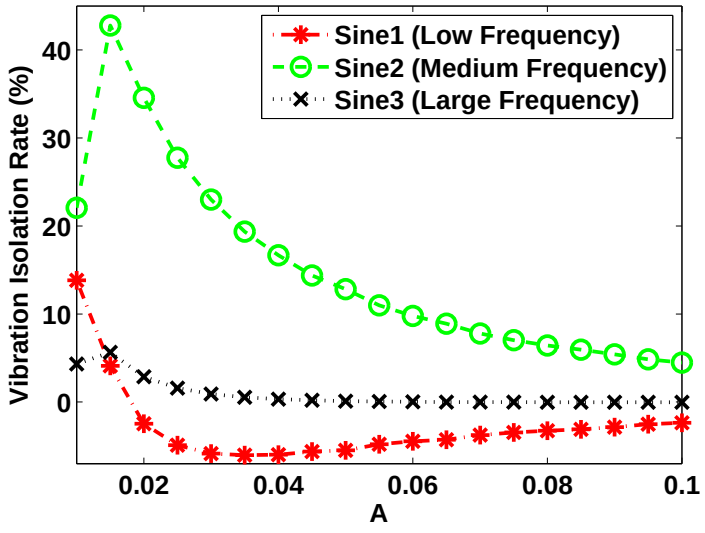

Figure 5.8: Optimization Results

Table 5.1: Parameters of Sinusoidal Excitations for H-Infinity Control

Case	A_1	ω_1	ϕ_1	A_2	ω_2	ϕ_2	A_3	ω_3	ϕ_3
Sine 1	0.42	5	1	0.18	6	1.5	0.3	7	3
Sine 2	0.3	10	0.5	0.18	11	1.5	0.36	12	2
Sine 3	0.3	20	0	0.48	40	0	0.18	60	0

The damping ratio, ζ, and natural frequency, ω_n, could be obtained from the summary results in Figs. 4.11 and 4.12. Figures 5.9a and 5.9b illustrate the experimental results about relative velocity for 0.3 inch and 0.7 inch sinusoidal excitation with frequency 12 rad/s. The summary results for the damping force for various excitations and orifice voltages are shown in Fig. 5.10. The maximum force generated is 287 N, which occurs during orifice modulation from 5 volts under 0.2 inch excitation to 7 volts under 0.7 inch excitation. Therefore, the weighting function $W_2(s)$ is selected as $1/287$ for the controller design.

5.1.4 Determination of G_d

The disturbance transfer function G_d employed in (5.11) is the transfer function between X_s and X_d when the valve is closed. For a second order system, G_d can be derived from the step responses shown by Fig. 5.11. Specifically, the equations (5.23) to (5.26) are used to derive G_d. Recall the definitions of settling time and peak time for linear systems,

$$t_s = \frac{4}{\zeta\omega_n} \tag{5.23}$$

$$T_p = \frac{\pi}{\omega_n\sqrt{1-\zeta^2}} \tag{5.24}$$

$$C = 2\zeta\omega_n \tag{5.25}$$

The disturbance model can be represented as,

$$G_d = \frac{Cs+\omega_n^2}{s^2+Cs+\omega_n^2} \tag{5.26}$$

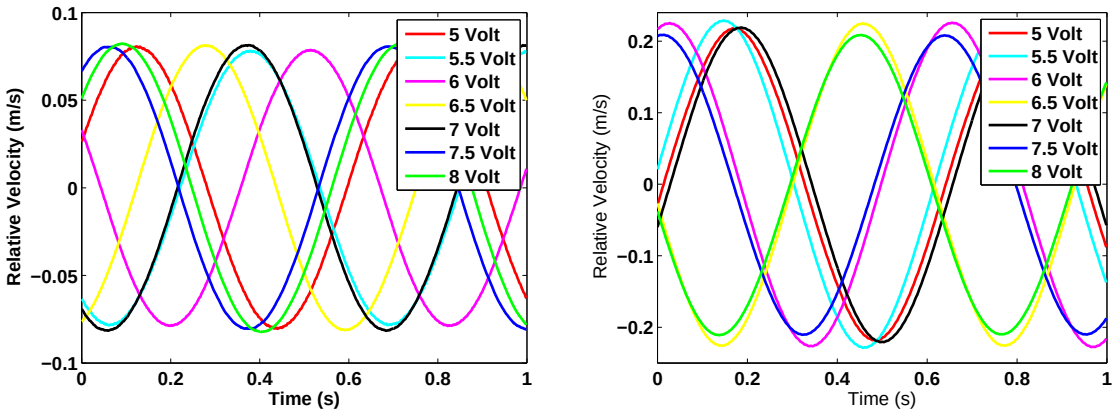

(a) 0.3 inch (b) 0.7 inch

Figure 5.9: Relative Velocity for Multiple Sinusoidal Excitations

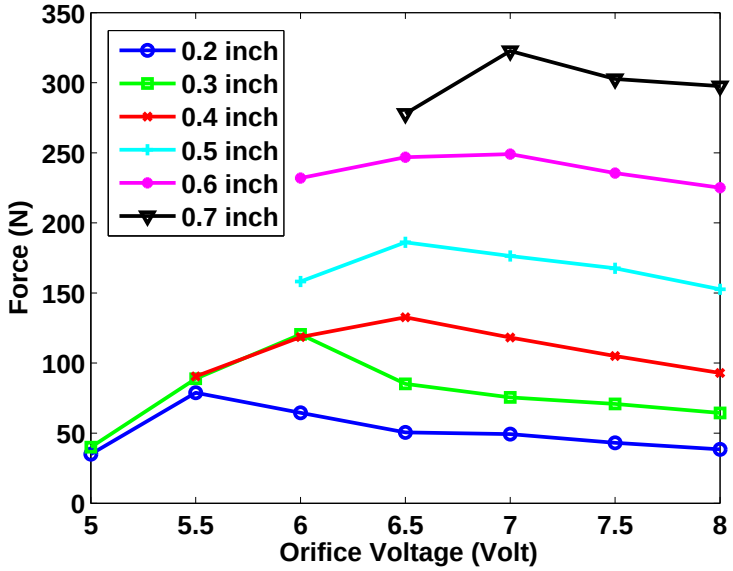

Figure 5.10: Damping Force for Multiple Excitations and Orifice Voltages

Table 5.2: Summary of Step Response Results

Amplitude (inch)	0.2	0.3	0.4	0.5	0.6	0.7
C	7.57	5.41	4.08	3.45	2.96	2.74
$\omega_n(rad/s)$	12.02	11.72	11.58	11.53	11.50	11.49

where, t_s: The settling time; T_p: The peak time; ζ: Damping ratio; ω_n: Natural frequency (Radian); C: Damping Coefficient.

As shown in Fig. 5.11, the step response varies as the excitation amplitude changes. This means that the disturbance model G_d depends on the excitation amplitude. Since it is not possible to design a controller with multiple disturbance models, only one G_d is to be chosen for controller design when the excitation amplitude is from 0.2 inch to 0.7 inch. To pick the "best" G_d, a set of controllers K was designed to minimize (5.11) for each G_d. After getting a set of G_d and K, the closed-loop performances, based on Eq. (5.27), were evaluated using a set of random sinusoidal excitation. The G_d model which gave the "best" vibration isolation performance was selected.

$$TF = G_d S \tag{5.27}$$

During the simulation study, the performances of the closed-loop system with each disturbance model G_d were studied. The G_d models were for 0.2 inch to 0.7 inch excitations with 0.1 inch interval. The H-infinity controller was designed based on each G_d and the sprung mass displacement X_s for each G_d was evaluated by comparing the root mean square (RMS) value of X_s. Four different simulation studies were performed based on multiple random excitations with various excitation frequencies. The time transient responses were plotted in Figs. 5.12 and 5.13. By observing Fig. 5.12a, it is noticed that X_s is less than the excitation source for every disturbance model. It means that designed controller is effective to isolate the vibration. To determine the G_d that generate the optimal performance, the RMS value of each response is compared, and the the summary of the RMS values for all of the case study is given in Appendix B. The performance of the closed-loop system is evaluated by the

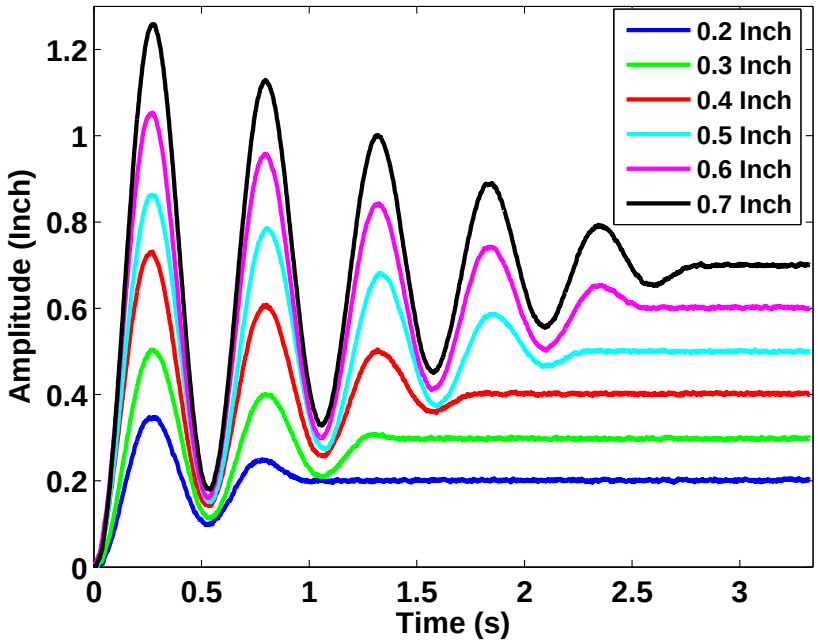

Figure 5.11: Step Responses for Multiple Amplitudes (Closed Valve)

vibration isolation level, which is indicated by the RMS reduction rate that is calculated by $\frac{RMS(X_d - Xs)}{RMS(X_d)}$. Figure 5.14 summarizes the vibration isolation performance of the closed-loop responses for multiple disturbance models. Overall, good isolation performances were obtained using the selected G_d with a large amplitudes, for example, 0.6 to 0.7 inches. The G_d is given in Eq. (5.28).

$$G_d = \frac{2.74s + 131.9}{s^2 + 2.74s + 131.9} \tag{5.28}$$

After determining the nominal model, G_n, the disturbance model, G_d and the weighting functions $W_1(s)$ and $W_2(s)$, the controller K to minimize Eq. (5.11) is given by,

$$K(s) = \frac{N_k(s)}{D_k(s)} \tag{5.29}$$

where, $N_k(s) = -8.77e4s^6 - 3.45e6s^5 - 4.3e7s^4 - 1.95e8s^3 - 9.452e7s^2 + 2.23e10s + 7.01e11$,

$D_k(s) = s^7 + 67.73s^6 + 2138s^5 + 4.211e4s^4 + 5.677e5s^3 + 5.311e6s^2 + 3.375e7s + 1.13e8$.

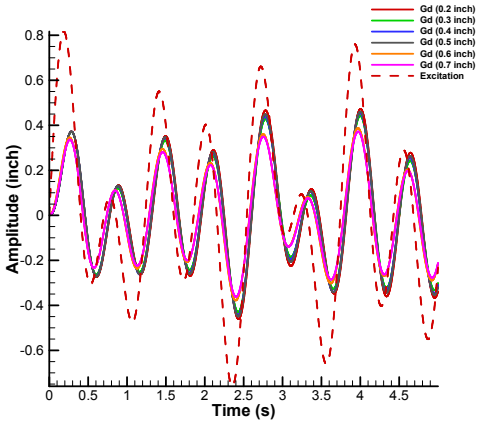

(a) Case 1

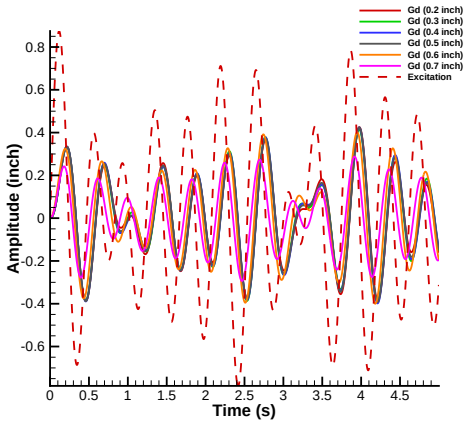

(b) Case 2

Figure 5.12: Relative Velocity for Multiple Sinusoidal Excitations: Part 1

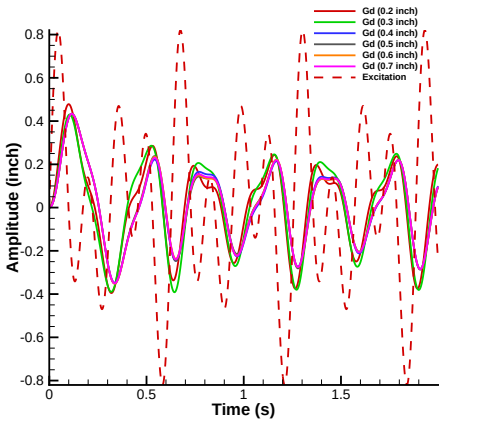

(a) Case 3

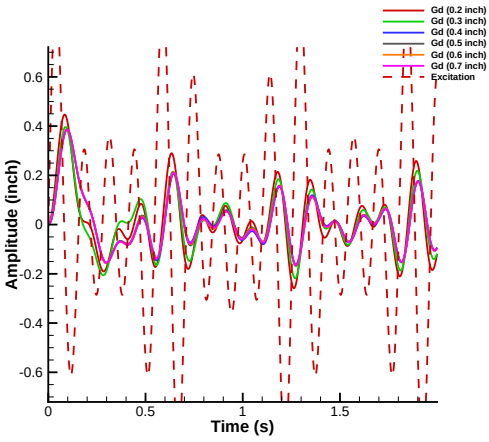

(b) Case 4

Figure 5.13: Relative Velocity for Multiple Sinusoidal Excitations: Part 2

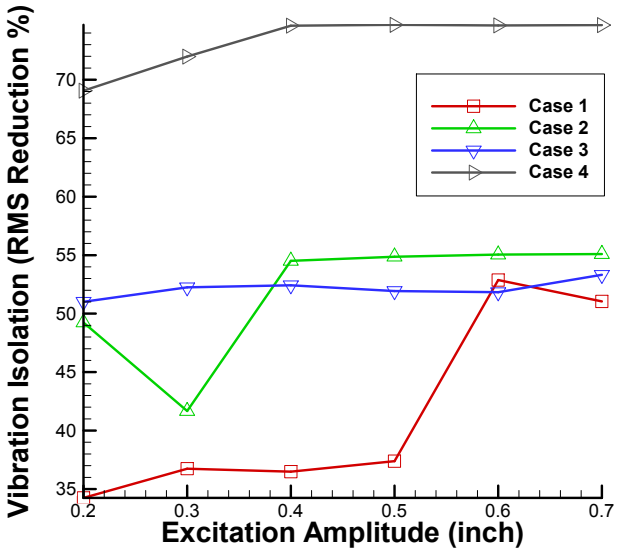

Figure 5.14: Vibration Isolation Rates of Closed-Loop Performances

5.2 H-Infinity Controller Performance

5.2.1 Frequency Response Analysis

Figures 5.15a to 5.15c illustrate the open-loop and closed-loop frequency response plots for multiple sinusoidal excitations, specifically, for 0.2 inch, 0.4 inch and 0.6 inch amplitude excitations. Figure 5.15a shows the closed-loop responses when the plant models used are the nominal model and the two off-design cases: models for 0.2 inch with 5 volt and 8 volt orifice voltage inputs. The peak amplitudes of closed-loop responses reduce significantly at the resonant frequency. The closed-loop natural frequency shifts to lower value due to the decreasing stiffness with opening valve. The plots also show that the closed-loop responses are desirable except in the high frequency range.

To verify the effectiveness of the controller for other excitation cases, the frequency responses for 0.4 inch and 0.6 inch were also studied and are shown in Figs. 5.15b and 5.15c. Both plots show that the closed-loop responses have low resonant vibration levels, although the isolation performance is not as good as the one shown in Fig. 5.15a. The reason is that since the controller was designed based on G_n associated with 0.2 inch excitation, the performance

deteriorates for other excitation amplitude cases. Similarly as the results for 0.2 inch cases, at the high frequency, i.e. greater than 4 Hz, all of the closed-loop responses for 0.6 inch models are worse than the open-loop response.

5.2.2 Transient Response Analysis

Figure 5.16a shows the step responses of the open-loop and closed-loop systems using G_n corresponding to 0.2 inch test data. Besides G_n, the closed-loop analysis also includes the off-design cases: 0.2 inch disturbance amplitude with 5 volts and 8 volts respectively. As seen from the plots, the closed-loop system shows much improved performance over the open-loop system regardless of G_n. Figures 5.16b and 5.16c respectively illustrate the step responses for 0.4 inch and 0.6 inch cases. The closed-loop responses are improved over the one of the open-loop responses regardless of orifice voltage.

Besides the step responses, the system's performance for mixed sinusoidal disturbance of varying frequencies and amplitudes was also studied. Figures 5.17a to 5.17c show the system responses for sinusoidal excitations with varying amplitudes in the frequency range of 1 Hz to 4 Hz. It was observed that the closed-loop systems successfully isolate the vibrations. Figures 5.18a to 5.18c illustrate the system responses under various excitation amplitudes in a high frequency range, above 4 Hz. The plots show that the closed-loop responses did not improve much compared to the open-loop responses. Specifically, for 0.6 inch models the closed-loop responses are even worse than the open loop ones for high frequency excitation, as shown in Fig. 5.18c.

5.2.3 Summary

In summary, the simulation studies show that an effective H-infinity controller can be designed to achieve desirable vibration isolation. The closed-loop performance was examined both in frequency and time domain through extensive simulations. The controller design used the linear model derived from system-id process. The experimental validation is the next step and is addressed in the later chapters.

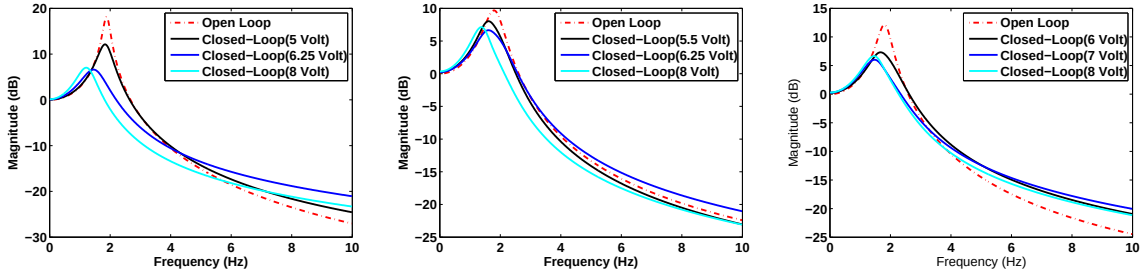

(a) 0.2 inch Models (b) 0.4 inch Models (c) 0.6 inch Models

Figure 5.15: Frequency Response Plots

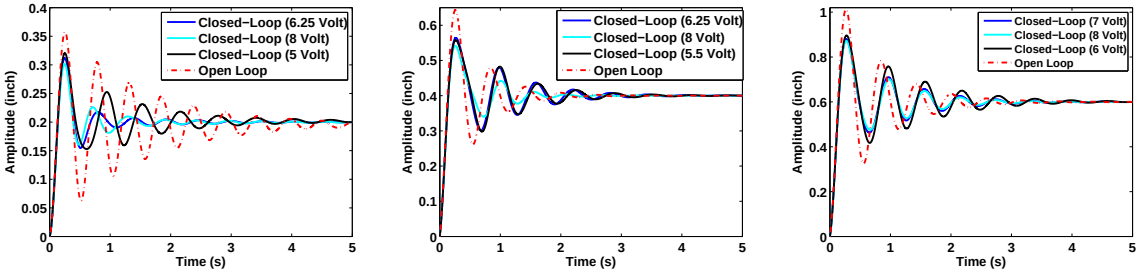

(a) 0.2 inch Excitation (b) 0.4 inch Excitation (c) 0.6 inch Excitation

Figure 5.16: Step Response Plots

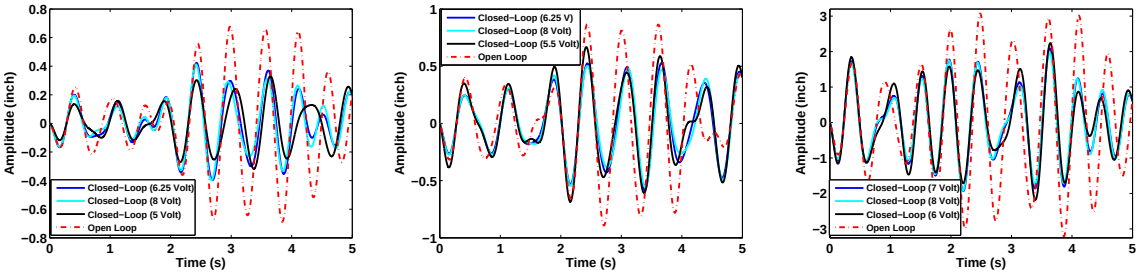

(a) 0.2 inch Excitation (b) 0.4 inch Excitation (c) 0.6 inch Excitation

Figure 5.17: Sinusoidal Responses: Part 1

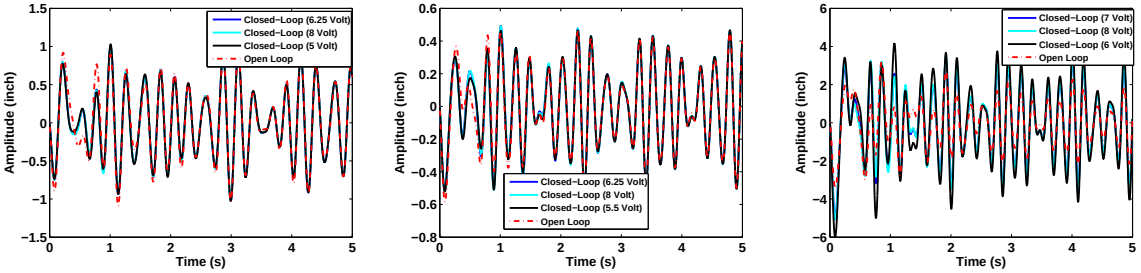

(a) 0.2 inch Excitation (b) 0.4 inch Excitation (c) 0.6 inch Excitation

Figure 5.18: Sinusoidal Responses: Part 2

CHAPTER 6. Model-Reference Sliding Mode Control

The previous chapter presented the H-infinity controller design and the closed-loop performance of the controller via computational simulations. The H-infinity design process yields the control force which is hard to implement because the control action is created by changing orifice opening which in turn also affects systems effective damping and natural frequency which is not accounted for in the H-infinity design process. So there is inherent uncertainty in the control force realization in practice which is not accounted for in traditional design.

This chapter focuses on a control design technique called "sliding mode control design" wherein the fast convergence to the desired trajectory is achieved by employing a discontinuous control (variable structure control). The use of sliding mode controller is to overcome limitations of the H-infinity control law by formulating the control problem as an asymptotic model matching problem-in which-the objective is to force the plant to behave like the H-infinity reference model in response to an exogenous input. The reference tracking is achieved by forcing the tracking error dynamics between the reference model and the pneumatic system in the sliding mode. The idea is that damping force can be made to follow the desired force generated by the H-infinity control law.

This chapter is organized as follows: First, a brief background of sliding mode control is given; then the problem formulation in the context of problem at hand is presented followed by the control law development. Finally, the designed control law is implemented on the simulation model and closed-loop simulations are presented demonstrating the effectiveness of the control scheme.

6.1 Fundamentals of Sliding Mode Control

This section gives a brief background of sliding mode concept using generic system description.

6.1.1 Sliding Surface

Given a single-input dynamic system,

$$x^n = A(X) + B(X)u \tag{6.1}$$

where the scalar x is the output of interest (the displacement of the pneumatic suspension system in this case), the scalar u is the control input (the solenoid orifice force in this case), and X=[x $\dot{x}$ .....$x^{(n-1)}$]^T is the state vector. The control strategy is to make the state X to track a desired time varying state vector X_r= [x_r $\dot{x_r}$ .....$x_r^{(n-1)}$]^T when $A(X)$ and $B(X)$ are not precisely known but are bounded by a continuous function of X.

In sliding mode methodology, one defines what is called as switching function s(x) as follows

$$s(x) = Sx = 0 \tag{6.2}$$

where $S \in \Re^{m \times n}$ and $x \in \Re^n$.

When x(t) is the solution to Eq. (6.2), the sliding motion is defined by the Eq. (6.3) and the state trajectory evolution is shown in Fig. 6.1,

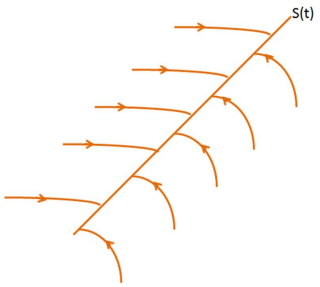

Figure 6.1: The Sliding Conditions (Jean J, Slotine, W., Li)

$$s(t) = 0, \forall t \geq t_f \tag{6.3}$$

where, t_f is a finite time. The sliding surface is defined as follows (56) ,

$$s = (\frac{d}{dt} + m)^{n-1} e = 0 \tag{6.4}$$

where, $e = x - x_r$ and one can get the state vector error as follows,

$E = X - X_r$=[e $\dot{e}$ .....$e^{(n-1)}$]^T

6.1.2 Sliding Mode Condition

The problem of tracking $X = X_d$ is equivalent to that of making sure that the system trajectories evolve such that system slides along the sliding surface s as shown in Fig. 6.2. Therefore, the sufficient condition to establish the sliding motion should be presented. (56) gives the sliding mode condition as follows,

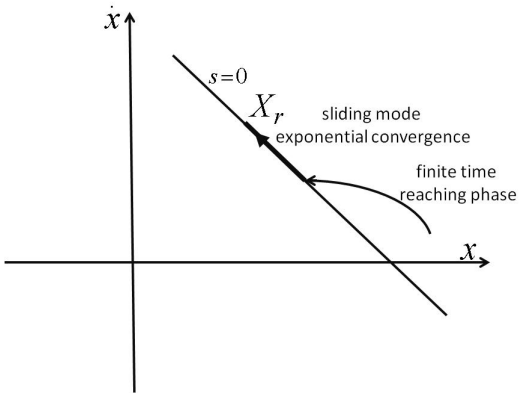

Figure 6.2: The Sliding Surface (Jean J, Slotine, W., Li)

$$s\dot{s} < -\eta\,|s| \tag{6.5}$$

6.2 State Space Representation of the Suspension System and Its Reference Model

This section presents the mathematical development needed for implementing sliding mode strategy for the control of the pneumatic system at hand. To begin with, the state space representations are obtained for both the reference model and the system model. Figure 6.3 represents the schematic of the reference model for pneumatic suspension system, in which F_r

consists of two parts as shown in Eqs. (6.6) and (6.7). The governing dynamical equation of the reference model is given in Eq. (6.8),

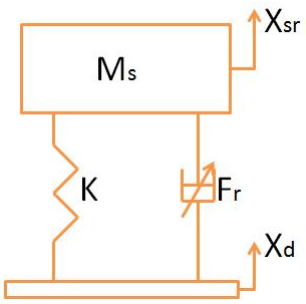

Figure 6.3: FBD of the Reference Model

$$F_r = F_d + F_{dr} \tag{6.6}$$

$$F_{dr} = C_{dr}(\dot{X}_{sr} - \dot{X}_d) \tag{6.7}$$

$$M\ddot{X}_{sr} + K_r(X_{sr} - X_d) + F_r = 0 \tag{6.8}$$

where,

F_{dr}: Damping force generated by the disturbance model in the reference;

C_{dr}: Damping coefficient of the disturbance model in the reference;

K_r: Suspension stiffness for the reference model.

By defining state vector $X_r = [X_{r1}, X_{r2}]'$, in which $X_{r1} = X_{sr}$ is the sprung mass displacement from the reference model, and $X_{r2} = \dot{X}_{sr}$ is the sprung mass velocity for the reference model. The state space representation of the reference model is given by Eq. (6.9),

$$\dot{X}_r = A_r X_r + B_{fr} F_r + B_{dr} X_d \tag{6.9}$$

where,

$$A_r = \begin{bmatrix} 0 & 1 \\ -\frac{K_r}{M} & 0 \end{bmatrix}, B_{fr} = \begin{bmatrix} 0 \\ -\frac{1}{M} \end{bmatrix}, B_{dr} = \begin{bmatrix} 0 \\ \frac{K_r}{M} \end{bmatrix}$$

Similarly, the governing dynamical equation of the pneumatic suspension system is obtained as follows,

$$M\ddot{X}_s + K(X_s - X_d) + F_{adj} = 0 \tag{6.10}$$

where $F_{adj} = C(\dot{X}_s - \dot{X}_d)$ is the damping force generated by the pneumatic suspension system, and C is the pneumatic suspension damping coefficient. Let the state vector as $X = [X_1, X_2]'$, where X_1 and X_2 are $X_1 = X_s$ and $X_2 = \dot{X}_s$ respectively. The state space representation of the pneumatic suspension system can be written as,

$$\dot{X} = AX + B_f F_{adj} + B_d X_d \tag{6.11}$$

where,

$$A = \begin{bmatrix} 0 & 1 \\ -\frac{K}{M} & 0 \end{bmatrix}, B_f = \begin{bmatrix} 0 \\ -\frac{1}{M} \end{bmatrix}, B_d = \begin{bmatrix} 0 \\ \frac{K}{M} \end{bmatrix}$$

6.3 Error Dynamics and Sliding Surface Design

After obtaining the state space representations of the reference model and the real system model, a suitable error dynamics and sliding surface can be derived. The error vector is defined as $E = [e_1, e_2]$, where $e_1 = X_s - X_{sr}$ and $e_2 = \dot{X}_s - \dot{X}_{sr}$. The governing dynamical equation is given as (6.12), and the state space representation of the error dynamics is represented by (6.13).

$$\begin{cases} \dot{e}_1 = e_2 \\ \dot{e}_2 = -\frac{K_r}{M} e_1 + \frac{1}{M}(F_r - F_{adj}) - \frac{K - K_r}{M}(X_s - X_d) \end{cases} \tag{6.12}$$

$$\dot{E} = A_e E + B_{ef}(F_r - F_{adj}) + B_{dis}(X_s - X_d) \tag{6.13}$$

,where

$$A_e = \begin{bmatrix} 0 & 1 \\ -\frac{K_r}{M} & 0 \end{bmatrix}, B_{ef} = \begin{bmatrix} 0 \\ \frac{1}{M} \end{bmatrix}, B_{dis} = \begin{bmatrix} 0 \\ -\frac{(K - K_r)}{M} \end{bmatrix}$$

B_{ef} is the input vector for error dynamics, and B_{dis} is the input matrix for error dynamics disturbances. Based on the error dynamics equations (6.12) and (6.13), it can be verified that the controllability matrix (6.14) has full rank, which means the states of the error vector E can be controlled to any desired values.

$$[B_{ef}, A_e B_{ef}] = \begin{bmatrix} 0 & \frac{1}{M} \\ \frac{1}{M} & 0 \end{bmatrix} \tag{6.14}$$

Based on the sufficient condition for the sliding motion in (6.5) and the error dynamics (6.13), the control law to guarantee the ideal sliding motion of error dynamics can be derived. By employing the formula in (56), the sliding surface s could be defined in Eq. (6.15). Once s is on the ideal sliding surface, one gets Eq. (6.16). After combining Eqs. (6.12) and (6.16), the sliding motion could be rewritten as Eq. (6.17).

$$s = me_1 + e_2 \tag{6.15}$$

$$s = \dot{s} = m\dot{e}_1 + \dot{e}_2 = 0 \tag{6.16}$$

$$\dot{s} = m\dot{e}_1 + \dot{e}_2 = me_2 - \frac{K_r}{M}e_1 + \frac{1}{M}(F_r - F_{adj}) - \frac{K - K_r}{M}(X_s - X_d) = 0 \tag{6.17}$$

In terms of control law to guarantee the ideal sliding motion, the adjustable force F_{adj} could be considered in Eq. (6.18).

$$F_{adj} = F_n + F_{dis} \tag{6.18}$$

where, F_n is the force for the nominal model control without disturbances, and F_{dis} is a discontinuous or switched force for disturbances including varying parameters and uncertainties. By choosing F_n as Eq. (6.19), Eq. (6.17) could be simplified as Eq. (6.20).

$$F_n = F_r - K_r e_1 + Mme_2 \tag{6.19}$$

$$\dot{s} = -\frac{1}{M}F_{dis} - \frac{K - K_r}{M}(X_s - X_d) \tag{6.20}$$

By defining a value ρ as (6.21) and F_{dis} as Eq. (6.22), one could get (6.23) to satisfy the ideal sliding motion condition,

$$\rho \leq -M\eta - |(K - K_r)(X_s - X_d)| \tag{6.21}$$

$$F_{dis} = -\rho sgn(s) \tag{6.22}$$

$$s\dot{s} = -\frac{1}{M}F_{dis}s - \frac{K - K_r}{M}(X_s - X_d)s \leq -\eta\,|s| \tag{6.23}$$

By adding Eqs. (6.19) and (6.22), the control force to guarantee the sliding motion is given in Eq. (6.24).

$$F_{adj} = F_r - K_r e_1 + M m e_2 - \rho sgn(s) \tag{6.24}$$

Please note the term $sgn(s)$ of Eq. (6.24) is a discontinuous item. For a pneumatic suspension system, the implementation of such a control law including the discontinuous part would produce a chattering motion at a boundary of the surface s, which is not desired in practice because it will cause wear and tear of the actuator. Therefore, $sgn(s)$ is approximated by a continuous term, $sat(\frac{s}{\phi})$, and the control law (6.24) is rewritten as Eq. (6.25). Figures 6.4a and 6.4b are the examples of the force input based on Eqs. (6.24) and (6.25) respectively. The item ϕ of Eq. (6.25) is defined as the boundary layer thickness. The new control law (6.25) would force the trajectory of s to move close to the ideal sliding motion. Once s enter the area within the boundary ϕ of the ideal sliding motion, the control law becomes continuous to avoid the chattering problem. Therefore, instead of letting s always stay on the ideal sliding motion, s is allowed to move up and down within ϕ of the ideal sliding motion. In order to have ideal reference tracking performance, the boundary thickness ϕ needs to be tuned and will be discussed later in this chapter.

$$F_{adj} = F_r - K_r e_1 + M m e_2 - \rho sat(\frac{s}{\phi}) \tag{6.25}$$

$$\begin{cases} sat(\frac{s}{\phi}) = \frac{s}{\phi}, if\ |s| \leq \phi \\ sat(\frac{s}{\phi}) = sgn(s), otherwise \end{cases} \tag{6.26}$$

6.4 Simulation Study about Reference Tracking Performances

The previous section presented the control law to guarantee the sliding motion of the error dynamics between the reference model and the suspension system. The control law (6.25) was given based on the sliding surface construction (6.15). To implement the control law (6.25) on the prototype suspension system, it is necessary to evaluate the reference tracking performance for various parameter values, m, ρ, and ϕ. This section is devoted to determine "good" parameter values that will facilitate the implementation of the control law. The criteria to determine "good" parameters are listed below,

1. Small reference tracking error between the sprung mass displacement and its reference.
2. Continuity of the force input to avoid fatigue of the actuator.

The simulink diagram for the model reference control is shown in Appendix C. Three random sinusoidal excitations based on the formula (6.27) were used in the simulation study. The parameter values employed in each excitation case are summarized in Table 6.1.

$$y = b_1 A_1 Sin(\omega_1 * t) + b_2 A_2 Sin(\omega_2 * t) + b_3 A_3 Sin(\omega_3 * t) \tag{6.27}$$

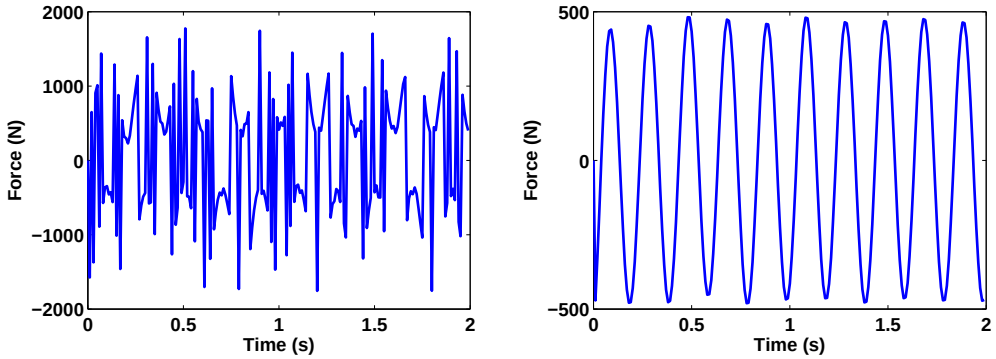

(a) Discontinuous Control Law (b) Continuous Control Law

Figure 6.4: Sample Plots: Force Input for Discontinuous and Continuous Control Law

6.4.1 Sutdy on the Effects of m

The first parameter studied was coefficient of e_1 in (6.15)- m. Ideally the m value once selected should be universal for random excitations. During the search for "good" m values, the other parameter values were fixed ($\rho = -2000$ and $\phi = 0.05$). The stiffness K_r was equal to 22180 N/m, and the stiffness K was equal to 15000 N/m.

Usually, a very large m or a very small m is undesirable for reference tracking due to the nonconvergent solution. As shown in Figs. 6.5a and 6.5b, m=0.1 and m=300 would lead to the nonconvergent results. The cause for this phenomenon could be explained as follows: Given a small m, a large reference tracking error is expected because the force input from the sliding mode control is not enough to suppress the reference tracking error, and the increasing tracking error could go to infinite within finite time. On the contrary, a large m would require an overwhelming force input to the system which would exceed the force limit and result in a nonconvergent solution.

Based on the above, m=200, 100, 10 are employed in the simulation study. Figures 6.6 illustrate the results for the excitation source 1, representing the low frequency excitation. We could observe that the reference tracking performance is improved with the increasing m value. The force input for all of the m's are continuous. Therefore, we could claim that the simulated three m values could be considered as the candidates for the parameter values in the control law.

As mentioned above, the suggested parameters should be universal for multiple excitations. Therefore, the simulation study was also performed based on the excitation sources 2 and 3, representing medium frequency and high frequency respectively. The simulation results

Table 6.1: Parameters of Sinusoidal Excitations for Sliding Mode Control

Excitation Number	b_1	A_1	ω_1	b_2	A_2	ω_2	b_3	A_3	ω_3
1	0.8	0.6	4	0.5	0.6	6	0.6	0.6	8
2	0.8	0.6	15	0.5	0.6	13.5	0.6	0.6	18
3	0.2	0.6	30	0.8	0.6	36	0.7	0.6	45

are summarized in Figs. 6.7 to 6.8. For reference tracking performance, the plots show the performance with $m = 10$ is the least satisfying, and performance based on $m = 100$ and $m = 200$ are very similar. The force input is continuous and smooth. Therefore, we could conclude that the simulated m values are good for all of the excitation sources and m=200 is recommended for the control law.

6.4.2 Study on the Effects of ρ

The parameter ρ of the control law (6.25) is to guarantee the convergent sliding motion with the existence of the varying parameters and dynamic uncertainties. The approximate value of ρ could be determined based on (6.21). In (6.21), η is a positive value that is inversely proportional to the time reaching the sliding motion from the initial state of $s(0)$. Since $s(0)$ is equal to 0 in both the simulation study and experimental test in the later chapter, η is selected to be 0 to simplify the study. Then the condition of ρ to satisfy the sliding motion could be rewritten as (6.28). In the simulation study K_r is selected as 22180 N/m and the suspension stiffness K is equal to 15000N/m. $X_s - X_d$ is a dynamically varying parameter, while the m and ϕ value are equal to 200 and 0.05 respectively in the simulation study.

$$\rho \leq -M\eta - |(K - K_r)(X_s - X_d)| \Rightarrow -\rho \geq |(K - K_r)(X_s - X_d)| \tag{6.28}$$

To satisfy the condition of (6.28), a ρ value is selected which make $-\rho$ large enough to cover $|(K - K_r)(X_s - X_d)|$ for all of the conditions. In the simulation study, three different values of ρ (-2000, -200, and -20) were studied and the simulation results are presented in Figs. 6.9

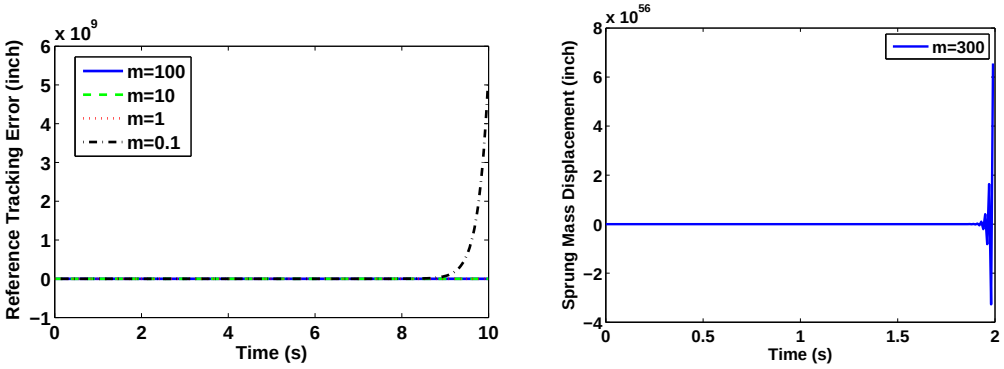

(a) Discontinuous Control Law (b) Continuous Control Law

Figure 6.5: Sample Plots: m Values Result in Nonconvergent Solutions

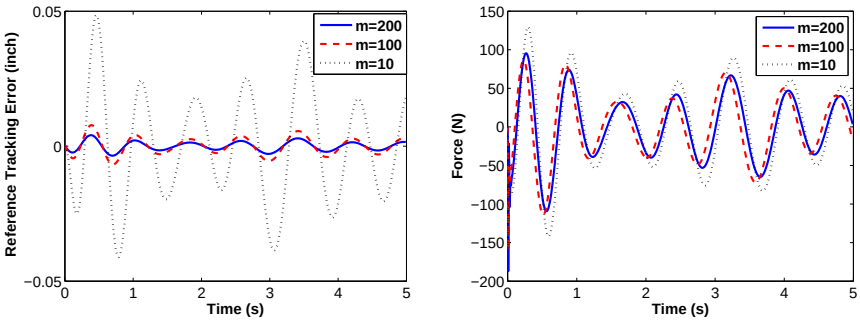

(a) Reference Tracking Error (b) Force Input

Figure 6.6: Excitation-1: Plots for m

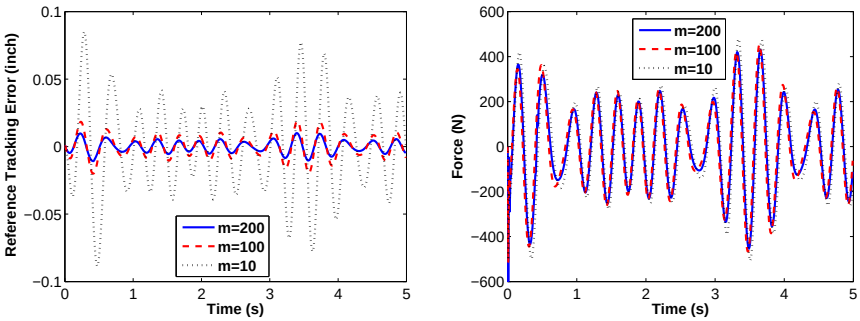

(a) Reference Tracking Error (b) Force Input

Figure 6.7: Excitation-2: Plots for m

to 6.11. It is observed that the simulation with ρ=-2000 always has the best performance of the reference tracking. The cause of this phenomena is because the selected - ρ is large enough to cover all of the uncertainty cases. The simulation results with ρ=-200 and ρ=-20 are least satisfying compared with the ones for ρ=-2000.

Although the above study shows the smallest ρ value produces the optimal performance, this does not mean that the ρ should be an infinitely small value. Figure 6.12 represent the simulation results for the reference tracking performance and force input for $\rho = -3000$ case. Obviously, such a high frequency force input is also of no practical usage, and the ρ cannot be an infinitely small number.

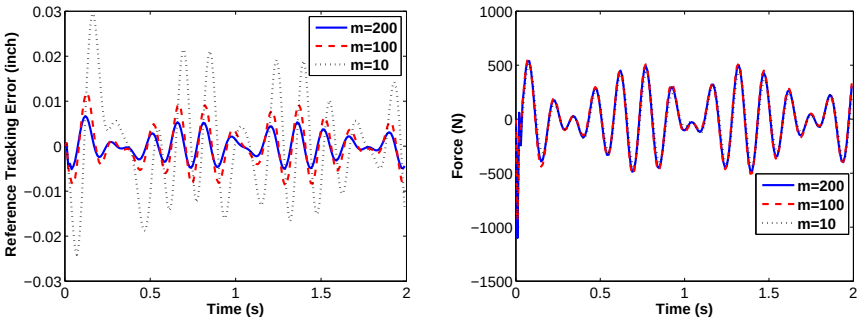

(a) Reference Tracking Error (b) Force Input

Figure 6.8: Excitation-3: Plots for m

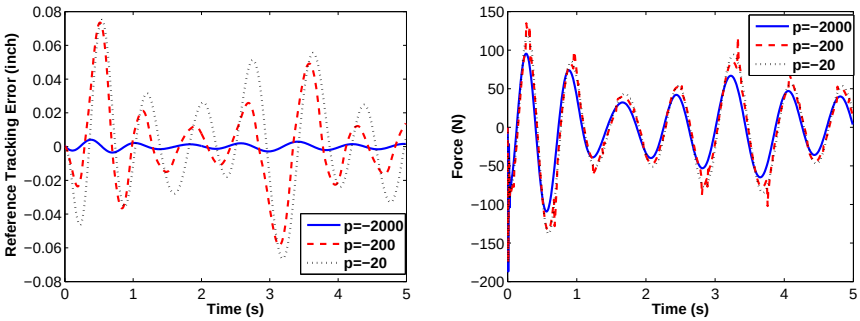

(a) Reference Tracking Error (b) Force Input

Figure 6.9: Excitation-1: Plots for ρ

6.4.3 Study on the Effects of ϕ

After studying the effects of parameter values of m and ρ, the effects of ϕ values were studied on the reference tracking performance. m=200 and ρ =- 2000 are used in the simulation study. Figure 6.13 shows the simulation results for various ϕ values (0.005, 0.05, and 0.5). It is observed that the change of ϕ value greatly affects the reference tracking performance. For instance, a very small ϕ value like 0.005 results in the discontinuous reference tracking error and force input which is not desired in reality. It also illustrates that a large ϕ value such as 0.5 has the larger reference tracking error than ϕ=0.05. Therefore, ϕ=0.05 is recommended to be used in the control law (6.25).

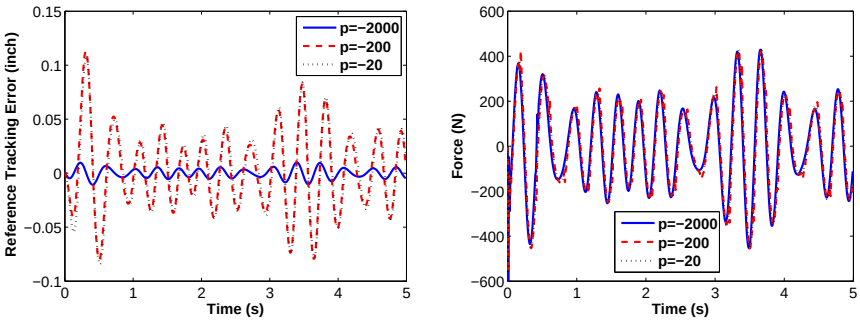

(a) Reference Tracking Error (b) Force Input

Figure 6.10: Excitation-2: Plots for ρ

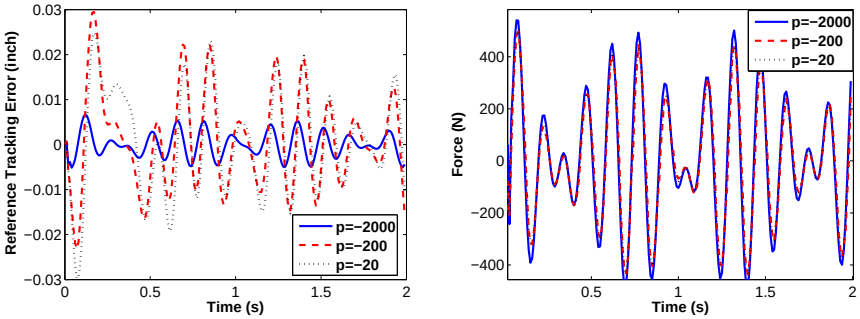

(a) Reference Tracking Error (b) Force Input

Figure 6.11: Excitation-3: Plots for ρ

6.4.4 Simulation Study on Multiple Stiffness Conditions

The parameter values of m, ρ, and ϕ ($m = 200$, $\rho = -2000$, and $\phi = 0.05$) are recommended by the above study. Please note that the suggested parameter values were only evaluated based on the condition that the stiffness of the real system is 15000 N/m. Since the pneumatic suspension is a stiffness-varying system, it is necessary to evaluate the performances under other system stiffness values. Two more stiffness (K=33268 N/m, K=11090 N/m) were studied and the results are summarized in Figs. 6.14 to 6.16. The results show that the varying stiffness does affect the reference tracking performance, force input, etc. Specifically, the system with stiffness K=33268 N/m has the minimum reference tracking error with the compensation of a large force input. Although there are differences between the performances for various stiffness values, the suggested parameter values in the control law are universal for all of the cases.

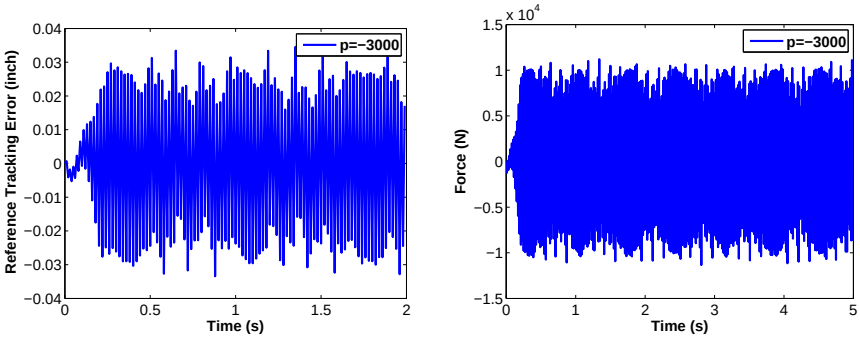

(a) Reference Tracking Error (b) Force Input

Figure 6.12: Excitation-3: Plots for ρ= -3000

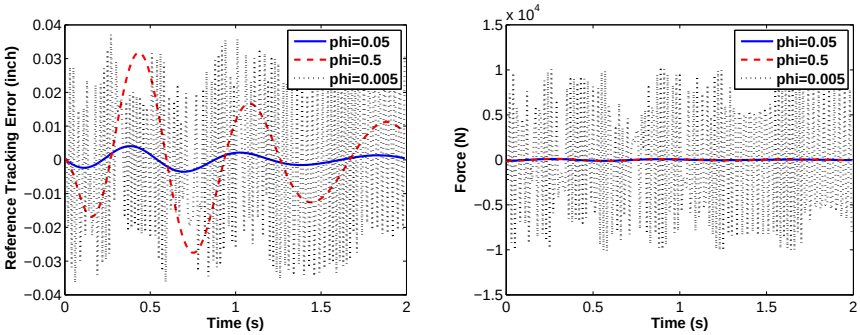

(a) Reference Tracking Error (b) Force Input

Figure 6.13: Excitation-1: Plots for ϕ

Therefore, one can conclude that the recommended parameter values in the control law are satisfactory for the controller design.

6.5 Summary

This chapter discussed the sliding mode reference tracking control and its application to pneumatic suspension system under consideration. Various simulation studies were performed to determine the acceptable values of parameters m, ρ, and ϕ. For the selected parameter values the controller performance was examined through simulations. The simulation results are presented in Figs. 6.6 to 6.16. The results show that the reference tracking error is controlled within a finite boundary to zero and no discontinuous force behavior was observed.

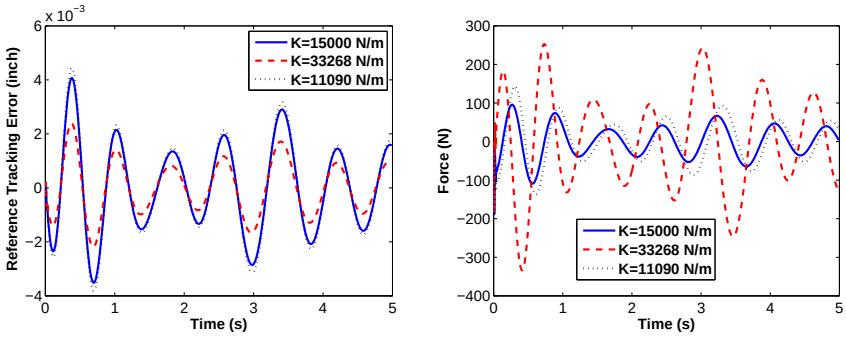

(a) Reference Tracking Error (b) Force Input

Figure 6.14: Excitation-1: Plots for Multiple Stiffness Values

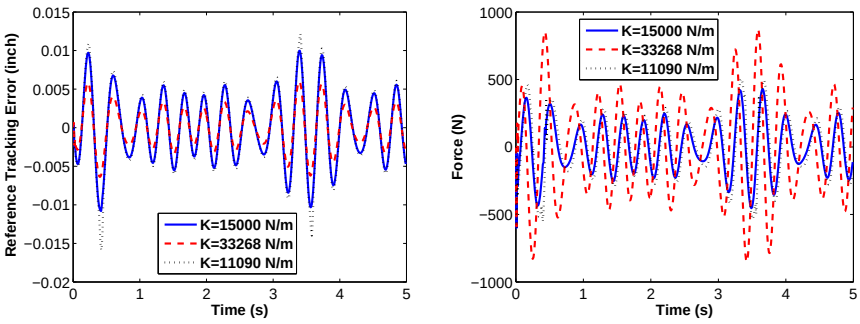

(a) Reference Tracking Error (b) Force Input

Figure 6.15: Excitation-2: Plots for Multiple Stiffness Values

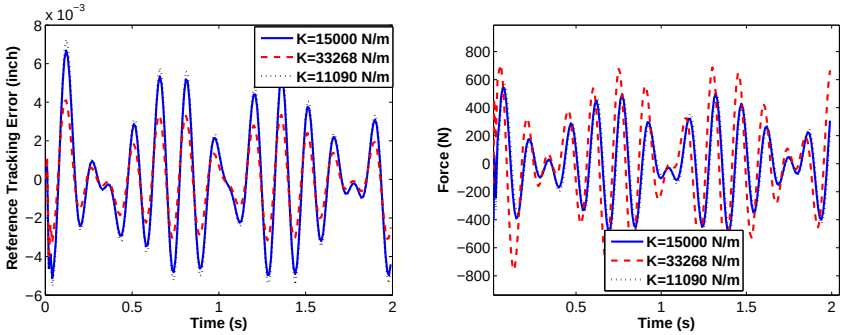

(a) Reference Tracking Error (b) Force Input

Figure 6.16: Excitation-3: Plots for Multiple Stiffness Values

CHAPTER 7. Experimental Validation of Controller Designs

The previous two chapters discussed the H-infinity and the sliding mode reference tracking controller designs and simulation results. The results showed that these controllers have good potential for improving the vibration isolation performance of the pneumatic suspension system. This chapter is focused on implementation of these controllers on real laboratory prototype system shown in Fig. 4.1 in the Experimental Test-Rig subsection of chapter 4. Since our control input derived in controller synthesis process is in terms of damping like force where as the actual control input for real system is the control voltage to solenoid valve it is important to determine the relationship between solenoid voltage V and the effective damping coefficient C.

A schematic of the overall control system is given in the block diagram of Fig. 7.1. It is composed of two parts: H-infinity control part and sliding mode control part. The H-infinity control is used to generate a reference force signal, and the sliding mode control is utilized to force the real system to follow the reference force signal in the presence of uncertainties and unmodeled dynamics.

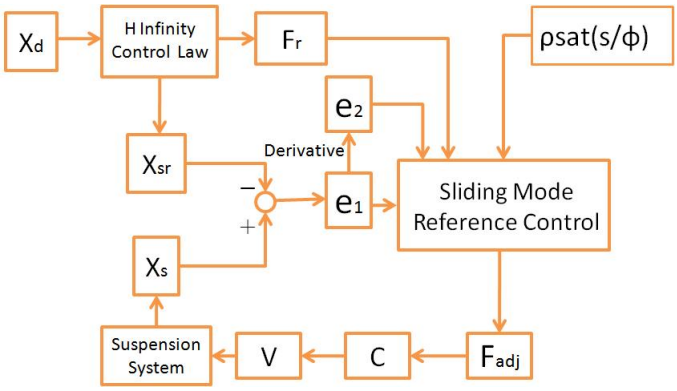

Figure 7.1: Structure of the Sliding Mode H-Infinity Robust Control

7.1 Determination of Mapping Functions between V and C

For the pneumatic suspension system, the force input F_{adj} is controlled by controlling the opening of the solenoid orifice. The control input is the solenoid voltage V and its output is F_{adj}. To implement the controller successfully, a full understanding of the mapping between F_{adj} and V is required. F_{adj} can also be calculated based on Eq. (7.1), in which C is the damping coefficient calculated by Eq. (7.2) and $\dot{X}_s - \dot{X}_d$ is the relative velocity, derived from the relative displacement. By combining Eq. (7.2), Figs. 4.11 and 4.12 together, the mapping between C and V for each excitation case is obtained in Fig. 7.2. For each desired F_{adj}, there exists a corresponding C as seen in Eq. (7.1). By collecting the desired C and base displacement X_d, the desired V could be interpolated based on Fig. 7.2.

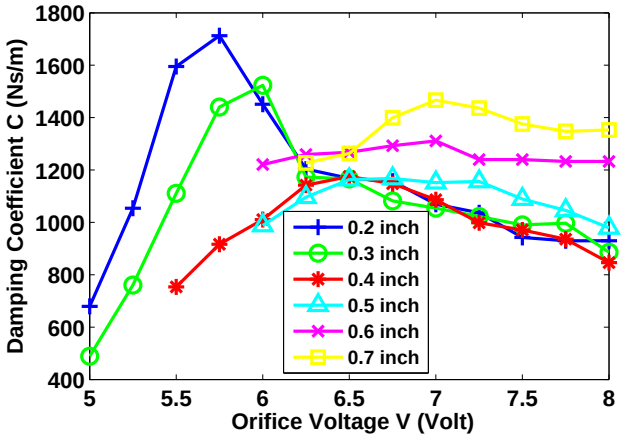

Figure 7.2: Damping Coefficient Vs Orifice Voltage

$$F_{adj} = C(\dot{X}_s - \dot{X}_d) \Rightarrow C = \frac{F_{adj}}{\dot{X}_s - \dot{X}_d} \tag{7.1}$$

$$C = 2\zeta\omega_n M \tag{7.2}$$

In Eq. (7.1), the relative velocity can be obtained by differentiating the relative displacement. Therefore, the problem of mapping $F_{adj} = f(V)$ can be transferred to the mapping of $V = f(C)$ for each excitation case. One challenge is that the mapping is nonlinear by nature. For instance, for 0.2 inch case the mapping $V = f(C)$ is shown in Fig. 7.3. In Fig. 7.3, one

particular C value can be generated by two different V values. In that case, it brings up a question which orifice voltage we should use. We use 0.2 inch case as the example and separate Fig. 7.3 into two parts by the "peak C"-5.75 volt. Two mapping functions can be fitted for each part as shown in Fig. 7.4.

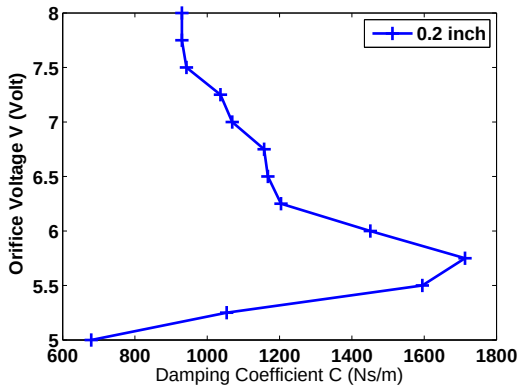

Figure 7.3: Orifice Voltage Vs Damping Coefficient for 0.2 inch Excitation Case

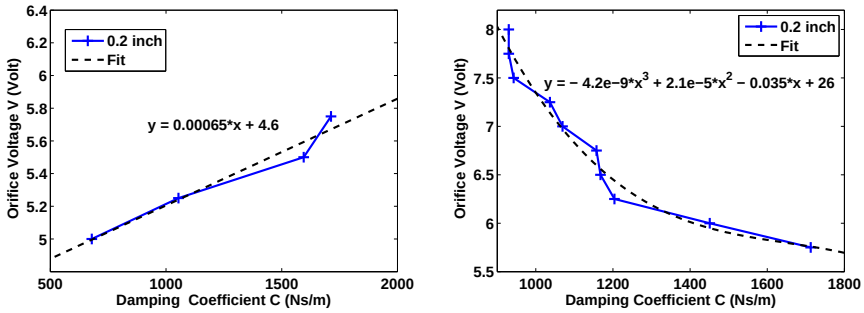

(a) Case 1: V $\leq$ 5.75 Volt (b) Case 2: V $\geq$ 5.75 Volt

Figure 7.4: Curve-Fit Function $C = f(V)$ for 0.2 inch

By using the same method, the fitted functions for other excitations, from 0.3 to 0.7 inches, can be given in Figs. 7.5 to 7.9. All of the "Case 1" mapping functions from Figs. 7.4 to 7.9 contribute a set of mapping functions to represent $V = f(C)$ for a random excitation with amplitudes from 0.2 to 0.7 inches. An interesting phenomenon is observed that the major controllable range for the damping is from 5 to 7 volts. This matches the results in Fig. 7.2 in that the orifice voltage range from 5 to 7 volts has a wide damping controllable range. Similarly, all of the "Case 2" mapping functions fitted from Figs. 7.4 to 7.9 contribute a new

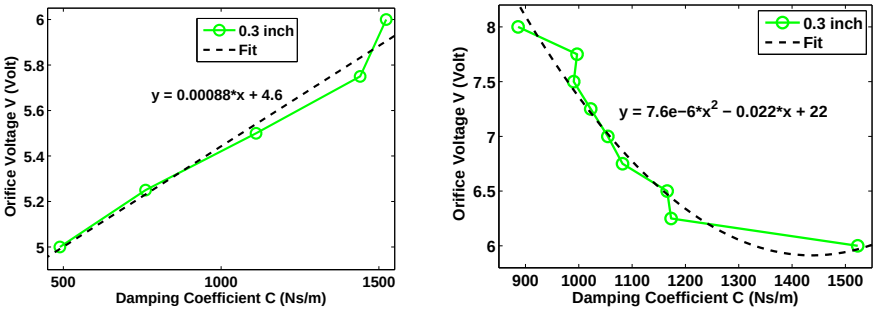

(a) Case 1: V $\leq$ 6 Volt (b) Case 2: V $\geq$ 6 Volt

Figure 7.5: Curve-Fit Function $C = f(V)$ for 0.3 inch

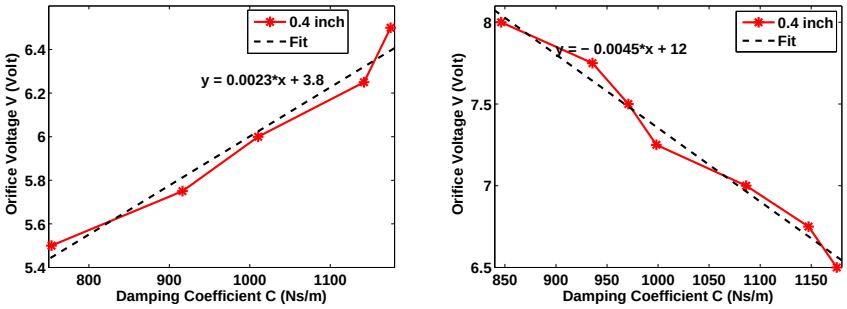

(a) Case 1: V $\leq$ 6.5 Volt (b) Case 2: V $\geq$ 6.5 Volt

Figure 7.6: Curve-Fit Function $C = f(V)$ for 0.4 inch

set of mapping functions for the large stiffness controllability. The details of each function are summarized in Appendix D.

As discussed above, one could select either "Case 1" subplots or "Case 2" subplots to obtain the set of mapping functions. However, whatever mapping function selected would be able to adjust the solenoid orifice on a partial voltage range instead of the whole range (5v to 8v). Therefore, one of the objectives for the experimental study was to compare the closed-loop

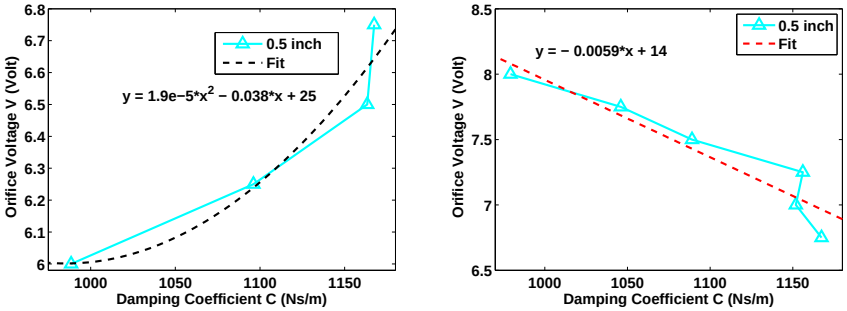

(a) Case 1: V $\leq$ 6.75 Volt (b) Case 2: V $\geq$ 6.75 Volt

Figure 7.7: Curve-Fit Function $C = f(V)$ for 0.5 inch

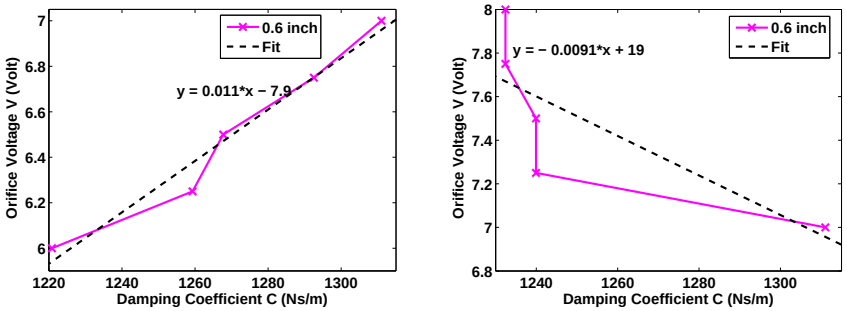

(a) Case 1: V $\leq$ 7 Volt (b) Case 2: V $\geq$ 7 Volt

Figure 7.8: Curve-Fit Function $C = f(V)$ for 0.6 inch

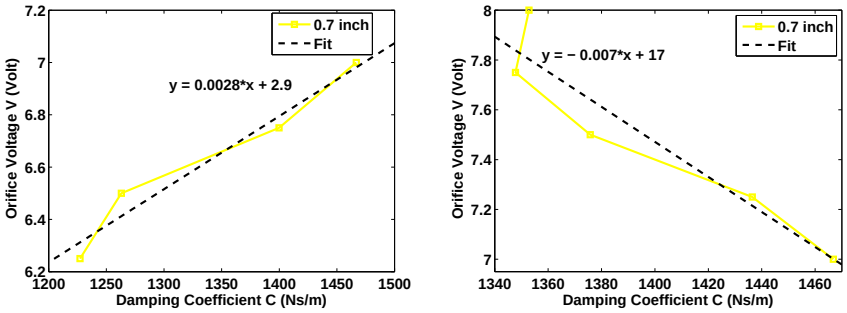

(a) Case 1: V $\leq$ 7 Volt (b) Case 2: V $\geq$ 7 Volt

Figure 7.9: Curve-Fit Function $C = f(V)$ for 0.7 inch

performances based on these two sets of mapping functions and choose the best option for the controller implementation.

7.2 Closed-Loop Analysis of the Nonlinear Pneumatic Suspension System

The controller designs in chapter 6 were based on the approximate (linear) dynamic models of the pneumatic system derived using system identification techniques. It is therefore necessary to see how these controller perform on higher fidelity nonlinear dynamic model obtained previously in earlier chapter. This section is devoted to explore the performance of the closed-loop system formed by interconnection of the nonlinear system model with controller designed using linear approximation. It is to be noted that although the control input computed by controller is the damping force, in the real system this is generated indirectly by modulating the opening of the solenoid valve. In the nonlinear model of the pneumatic suspension system developed in chapter 3, an important tuning factor K_{cr} was used to adjust the rate of change

of pressure in the pneumatic suspension system. By varying the K_{cr} values along time, one is able to implement the designed controller for the system-id models on the nonlinear model of the pneumatic suspension system. The key is to determine how the tuning K_{cr} varies along the time by the designed control law. In the experiment, the control voltage functions $V = f(t)$ can be approximately obtained by the mapping 2 functions of Figs. 7.19b, 7.20b, and 7.22b (see pages 111, 112). The functions $K_{cr}= g(V)$ for all cases can also be approximately obtained by Fig. 3.12. By combining the functions $V = f(t)$ and $K_{cr}= g(V)$, the function $K_{cr}= h(t)$ using the control law can be obtained. All three types of functions are summarized in Table 7.1. Besides K_{cr}, another important tuning parameters K_{amp} also needs to be considered. Since tuning of K_{amp} is challenging when used in dynamically varying K_{cr}, a set of random data in the range from 0 to 2 from chapter 3 was used in the simulation study. Three case studies were performed for 0.6 inch sinusoidal excitations with frequencies 10 rad/s, 15 rad/s, and 30 rad/s.

Table 7.1: Summary of Functions $V = f(t)$, $K_{cr}= g(V)$, and $K_{cr}= h(t)$

Frequency (rad/s)	$V = f(t)$	$K_{cr}= g(V)$	$K_{cr}= h(t)$
10	V=2.5 sin(10t)+5.5	K_{cr}=0.55 V-2.2	K_{cr}=1.375 sin(10t)+0.825
15	V=1.5 sin(15t)+6.5	K_{cr}=0.53 V-2.5	K_{cr}=0.795 sin(15t)+0.945
30	V=1 sin(30t)+6.5	K_{cr}=0.49 V-2.2	K_{cr}=0.49 sin(30t)+0.985

The simulation study was performed to compare the closed-loop performance (using varying K_{cr}) with open-loop performance (fixed K_{cr}), for a given set of excitations. Figures 7.10a, 7.10b, and 7.10c illustrate the simulation results for various cases. It is observed that the closed-loop system performance is better than the open-loop system performance. Figure 7.10a illustrates resonant response of the open loop system. This is due to the fact that the natural frequency cannot be shifted away from the resonant frequency of the system. This phenomena was later observed during the experimental study. At a high frequency excitation such as 30 rad/s in Fig. 7.10c, both the open-loop and closed-loop system show good vibration isolation performance which match the experimental results as will be shown in the next section.

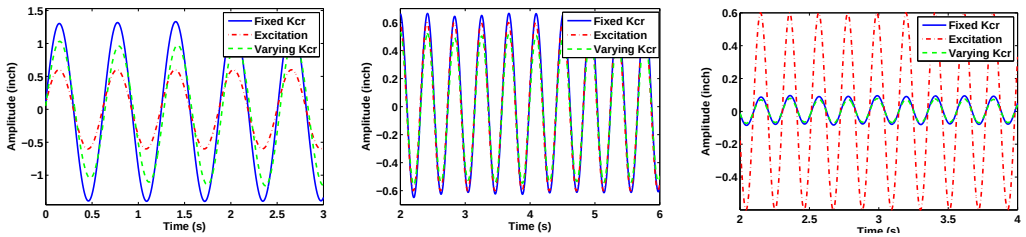

(a) 10 rad/s (b) 15 rad/s (c) 30 rad/s

Figure 7.10: Performances for the Nonlinear Model

7.3 Experimental Validation

The section 7.1 discussed the mapping needed to establish the relation between solenoid voltage and damping coefficient in order to enable implementation of the designed controller into the real system. Two sets of functions were determined to describe the mapping $V = f(C)$. The simulation results for the closed-loop performance using nonlinear plant model were presented in the previous section. This section is devoted to implementation of controllers on the real hardware and study the performance of the controller designs.

As a first step in the implementation, the parameter values determined for the control law of Eq. (6.25) are needed to be verified to see if they yield a desired performance as predicted by the simulation studies. The parameter values of m=200, ρ=-2000 and $\phi = 0.05$ were used in the experimental study.

As a part of experimental procedure, first a simulink model was created as shown in Appendix E and F. The feedback control system built in the simulink was depicted by the block diagram of Fig. 7.1. The input for the simulink model are the excitation sources and the control input (solenoid orifice voltage) X_s is the output of the simulink model. Two displacement transducers are used in the experimental study to record X_s and X_d respectively. The overall simulink model can be divided into three blocks as follows,

1. The first block is for H-infinity control. The objective of this control block is to send the reference signal of X_s based on the base displacement X_d.

2. The second block is for sliding mode control. The objective of this control block is to force the system to track the reference signal sent from the H-infinity control block. The input

to this block is the sprung mass displacement, velocity and the related reference signals. The output is the force input to the system F_{adj}, which is used to obtain the desired C by dividing the force by the relative velocity.

3. The third block is to obtain the desired solenoid orifice input voltage using the previously determined mapping $V = f(C)$. V can then be used in the control law (6.25).

The simulink model is downloaded onto the D-Space 1105 controller board. The board has 16 D/A and 16 A/D channels, which are used to send signals and receive signals from the suspension system.

The experimental study involved use of three excitation signals based on the formula in (6.27) and the parameters listed in Table 7.2. The X_s for each excitation signal was recorded to compare with the reference signal. Figures 7.11a to 7.12b illustrate the results for the excitation signal 1. Generally, a good correlation was observed between the experimental X_s and its reference signal and is shown in Fig. 7.11a. However, some error was observed at the small peak amplitude area. The reason for this phenomenon is that the air spring bag forces restrict the movement of the air spring, especially at the low frequency excitations with small amplitudes. Moreover, a small mismatch was observed between the simulated X_s and the reference signal. The reason is illustrated by the Fig. 7.12b as it can be seen that X_d in the experiment is slightly different from the one in the simulation. This deviation was generated by the mechanical shaker system even though the excitation command was same as the one used in the simulation study.

Table 7.2: Parameters for Sinusoidal Excitations in Experiment

Excitation Number	b_1	A_1	ω_1	b_2	A_2	ω_2	b_3	A_3	ω_3
1	0.8	0.6	4	0.5	0.6	6	0.6	0.6	8
2	0.8	0.6	15	0.5	0.6	13.5	0.6	0.6	18
3	0.8	0.6	30	0.5	0.6	36	0.6	0.6	45

The results for excitation signals 2 and 3 are presented in Figs. 7.13a to 7.16b. In case of the excitation signal 2, a good correlation is observed in Fig. 7.13a between the experimental X_s and its reference signal. The mismatch between the simulated X_s and the reference signal still

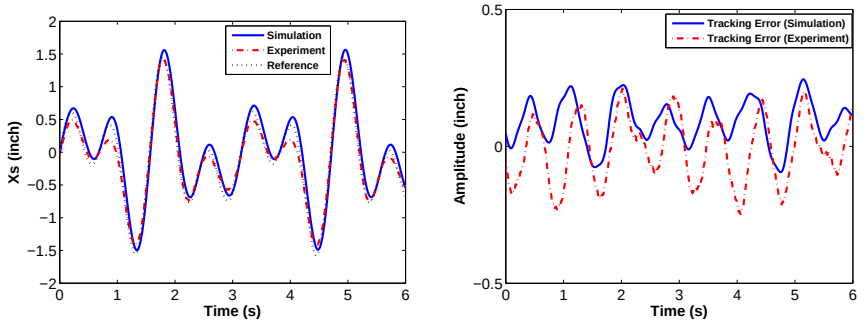

(a) Sprung Mass Displacement (b) Reference Tracking Performance

Figure 7.11: Simulation Results for Case 1: Part 1

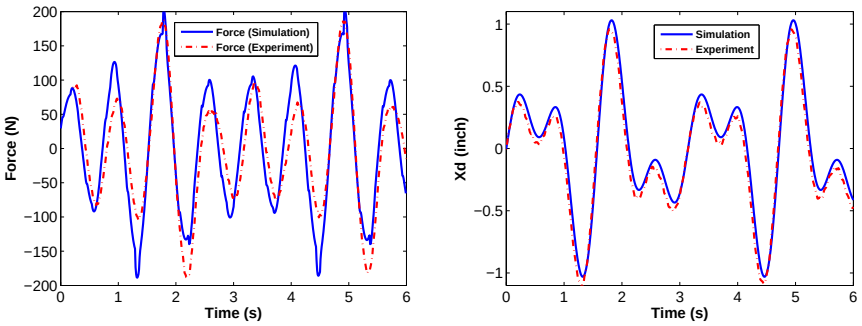

(a) Force Input (b) Excitation

Figure 7.12: Simulation Results for Case 1: Part 2

exists because the experimental X_d is different from the simulated one, as shown in Fig. 7.14b. Figure 7.14a shows that the experimental force input is less than the simulation due to the large reference tracking error in the simulation study, as shown in Fig. 7.13b.

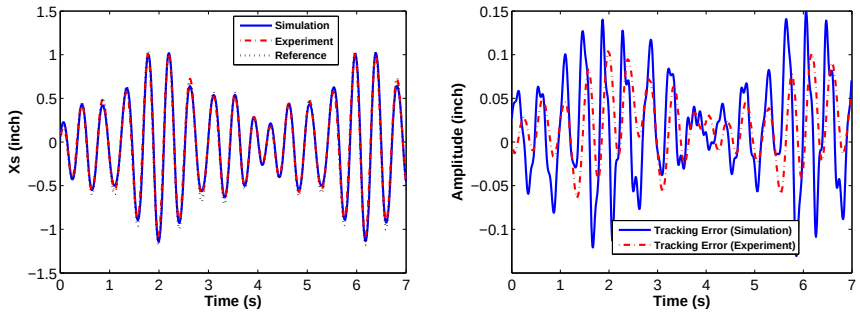

(a) Sprung Mass Displacement (b) Reference Tracking Error

Figure 7.13: Simulation Results for Case 2: Part 1

The responses to the excitation signal 3 are summarized in Fig. 7.15. A large mismatch between the data is observed. One of the reasons could be bandwidth limitation of the solenoid valve. The solenoid valve could not respond as fast as the system required under the high

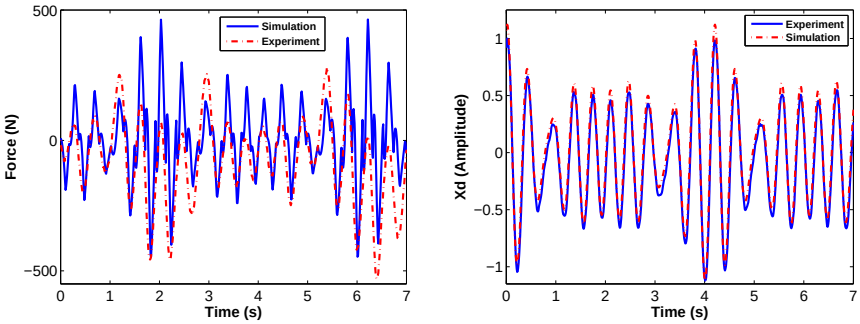

(a) Force Input (b) Excitation

Figure 7.14: Simulation Results for Case 2: Part 2

frequency excitation. The difference between the simulated X_s and the reference signal is due to a couple of reasons. One of the reasons is the big difference in the excitation signal illustrated by Fig. 7.16b, and another reason is that the system-id models do not accurately represent the system dynamics in the high frequency region. Therefore, the simulated response X_s is much different from the experimental X_s. Due to the existence of a large tracking error, a large force input is also observed in the force plot shown in Fig. 7.16a.

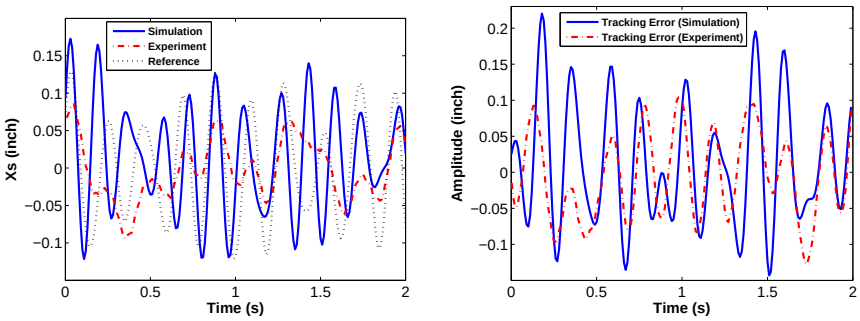

(a) Sprung Mass Displacement (b) Reference Tracking Error

Figure 7.15: Simulation Results for Case 3: Part 1

In summary, the experimental results show a good tracking performance at low frequency and medium frequency ranges. A large tracking error was observed in the high frequency range due to the bandwidth limitation of the solenoid valve and the inaccurate system-id models at high frequency. Next, the vibration isolation performance will be examined experimentally and the limitations of the controller bandwidth will be explored.

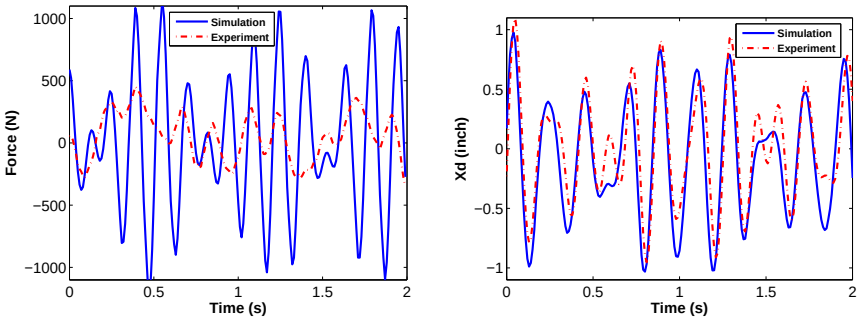

(a) Force Input (b) Excitation

Figure 7.16: Simulation Results for Case 3: Part 2

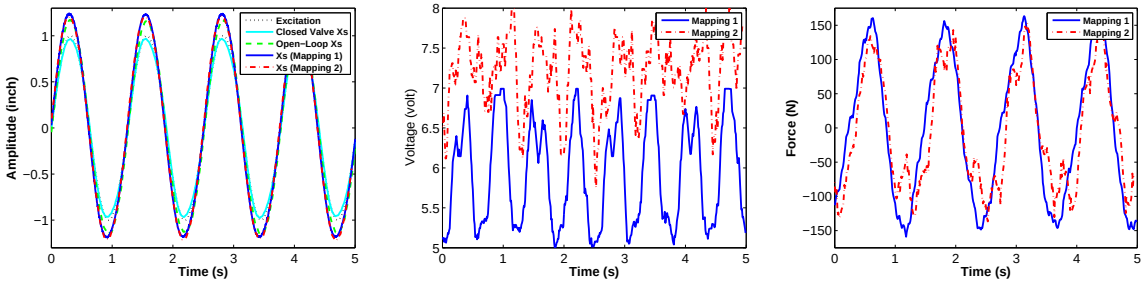

(a) Xs (b) Volt (c) Force

Figure 7.17: Experimental Results for the Sinusoidal Excitation with 5 rad/s

7.3.1 Vibration Isolation Performance and Controller Bandwidth

The primary objective of this thesis study is to design a control system to improve the vibration isolation performance. In order to study the vibration isolation performance of the closed-loop system, a series of experimental studies was performed for the two control laws. To be specific, the two closed-loop systems were designed based on two sets of mapping $V = f(C)$, as shown in Appendix D.

In the experimental study, a series of sinusoidal excitations with 1 inch amplitude were given to the shaker. The excitation frequencies were 5 rad/s, 8.5 rad/s, 11 rad/s, 14 rad/s, 25 rad/s and 30 rad/s. During the tests, the sprung mass displacement, orifice voltage and the force input were collected for each test case. Both open and closed-loop responses were recorded for each test case. The orifice voltage was always equal to 7 volts for the open-loop system. All of the test data is plotted in Figs. 7.17 to 7.22.

The root mean square value (RMS) is used to measure the vibration isolation performance of the system. The RMS values for all of the test cases were calculated and summarized in

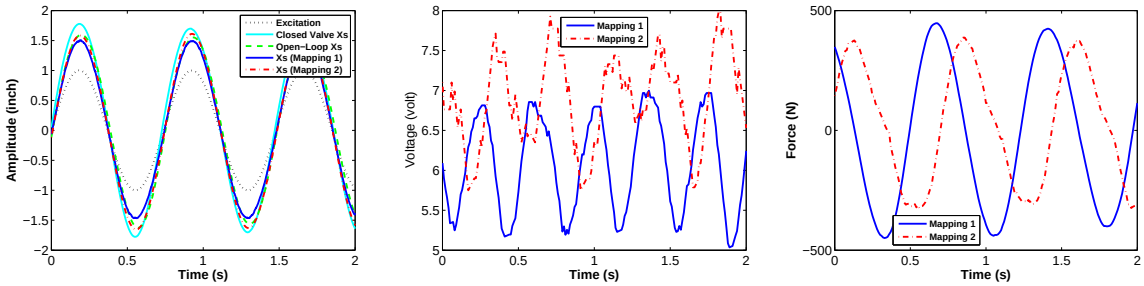

(a) Xs (b) Volt (c) Force

Figure 7.18: Experimental Results for the Sinusoidal Excitation with 8.5 rad/s

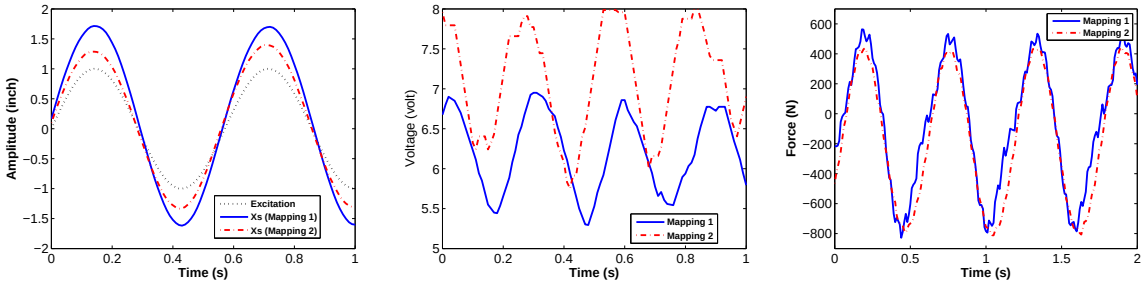

(a) Xs (b) Volt (c) Force

Figure 7.19: Experimental Results for the Sinusoidal Excitation with 11 rad/s

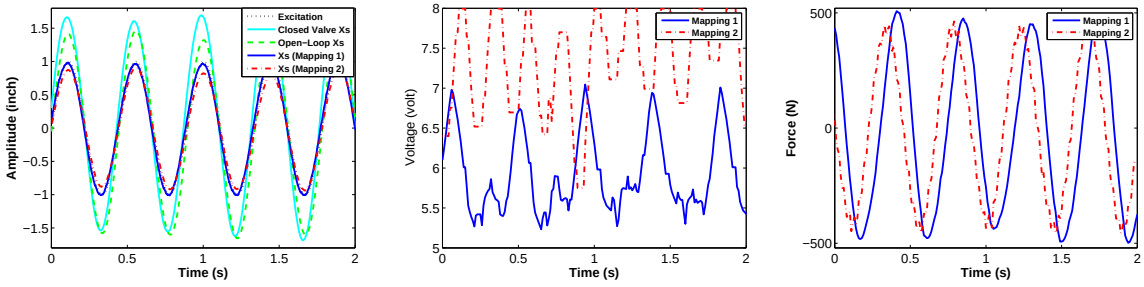

(a) Xs (b) Volt (c) Force

Figure 7.20: Experimental Results for the Sinusoidal Excitation with 14.1 rad/s

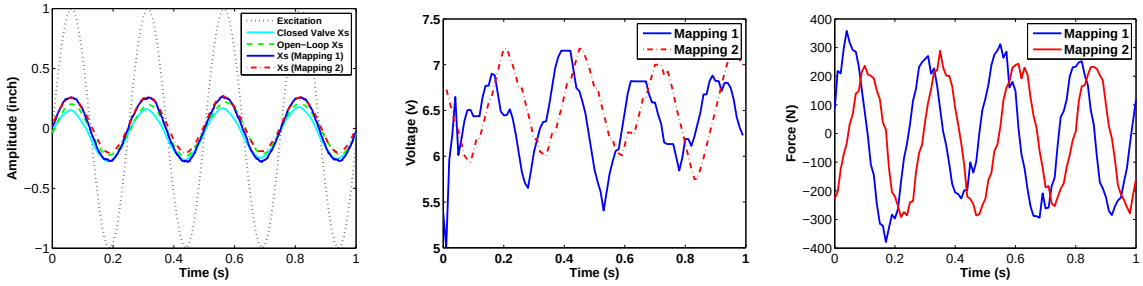

(a) Xs (b) Volt (c) Force

Figure 7.21: Experimental Results for the Sinusoidal Excitation with 25 rad/s

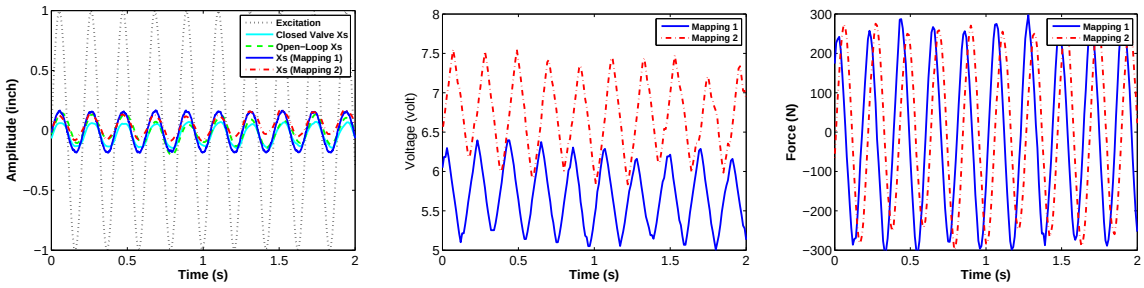

(a) Xs (b) Volt (c) Force

Figure 7.22: Experimental Results for the Sinusoidal Excitation with 30 rad/s

Fig. 7.23. For the open-loop system and the closed valve case, the data at the resonant frequency is unavailable because the resonant vibration is aggressive and exceeds the limit of the air spring stroke. The resonant vibration isolation is significantly improved for the closed-loop responses because the vibration is successfully controlled within the air spring stroke. The closed-loop vibration isolation performance at other frequencies is also improved. These frequencies are in the range 14 rad/s and 25 rad/s. In this frequency range, the closed-loop system can isolate the vibration effectively as the RMS of X_s is lower than the one for X_d.

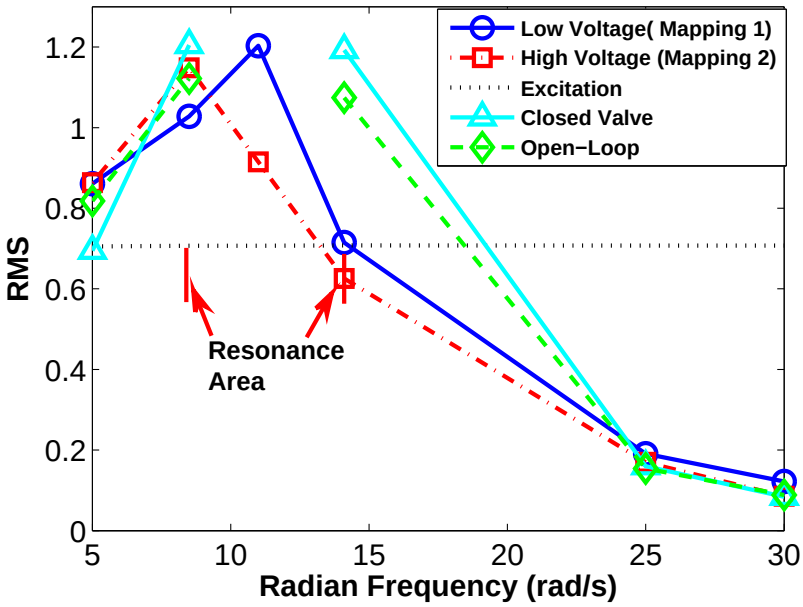

Figure 7.23: Summary for the Vibration Isolation Study

One can also notice that the RMS values of the closed-loop responses are larger than the one for the closed valve case when the excitation frequency is very low or high. This occurs when

the excitation frequency is equal to 5 rad/s or greater than 25 rad/s. However, since human beings are insensitive to the vibration when the excitation frequency is less than 1 Hz (6.28 rad/s), the lack of vibration isolation performance at such low frequencies is not a concern. The overall vibration amplitude is very small at high frequency excitations. As a result, it can be concluded that the closed-loop system performance under proposed controllers is satisfactory.

Next, the closed-loop performance is evaluated for different mapping functions used for relating voltage to damping. Figure 7.23 shows the closed-loop performance for two sets of mapping functions of $V = f(C)$. The closed-loop system with the first mapping is operated with the solenoid orifice voltage ranging from 5 to 7 volts, and the one with the second mapping is operated with the solenoid orifice voltage ranging between 5.75 to 8 volts. By observing the plots in Fig. 7.2, the damping coefficient controllability for mapping 1 is from 500 Ns/m to 1700 Ns/m, and the the damping coefficient for mapping 2 is from 850 Ns/m to 1700 Ns/m. Overall, the closed-loop system with the mapping 1 is operated with a large damping controllability in a relatively "stiff" suspension, and the closed-loop system with mapping 2 is operated with a small damping band in a relatively "soft" suspension. From Fig. 7.23, one could observe that the response for mapping 1 has a larger peak magnitude frequency than the one for the mapping 2. The reason is that a stiff suspension has a large natural frequency, which would result in a large peak magnitude frequency.

Although the above discussion conveys that a closed-loop system benefits from a relatively "soft suspension", it does not mean the system will respond well at a "soft" suspension with fixed stiffness. As shown in Fig. 7.23, the open-loop response has a similar resonant vibration problem as the closed valve case. It can be explained as follows: An open-loop system has a fixed natural frequency, and the vibration would be extreme when the excitation frequency is close to its natural frequency. Without the controller's ability to shift the natural frequency of the system by modulating the solenoid valve opening and changing the stiffness of the spring, no enough damping could be generated to suppress the resonant vibration magnitude. Therefore, a closed-loop control that has ability to continuously alter the frequency and damping characteristics of the system is needed for improving the vibration isolation performance of the pneumatic suspension system.

Besides the peak magnitude and frequency, the closed-loop system with mapping 2 has a wider controllable frequency band than the one with mapping 1. Based on the above discussion, it is recommended that the closed-loop system with mapping 2 is the better choice for the controller design.

Using the mapping 2 functions in the controller design, several random tests were performed to compare the closed-loop performance with the closed valve case. The excitation files were based on the formula in (6.27) and the coefficients are listed in the Table 7.3. Figures 7.24a to 7.24c show the results for the random test responses. As can be seen from the plots, the closed-loop system has much better performance than the closed valve case.

Table 7.3: Coefficients of Experimental Test

Case	A_1	ω_1	A_2	ω_2	A_3	ω_3
1	0.1	10	0.1	11	0.05	12
2	0.25	11	0.15	12	0.1	13
3	0.25	7	0.2	8	0.1	9

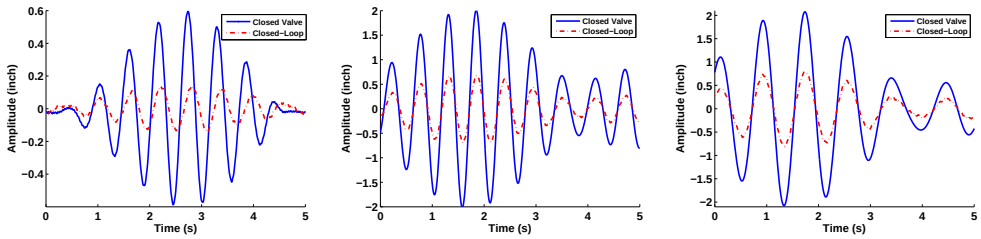

(a) Case 1 (b) Case 2 (c) Case 3

Figure 7.24: Closed-Loop Vs Closed Valve

CHAPTER 8. Conclusions and Future Work

This chapter summarizes the research findings from the work of this thesis and presents potential future directions to advance the state-of-the-art in the pneumatic suspension area.

Overall, this thesis deals with the modeling, analysis and control of the semi-active pneumatic suspension system. The primary contributions of this thesis include:

- gaining deeper understanding of the dynamical interaction between different parameters of semi-active pneumatic suspension under consideration.

- development of high fidelity nonlinear model of the system by incorporating thermodynamic properties of the compressible media (air) and exploring dependence of system dynamics on disturbance signal amplitude and other system parameters.

- development of suitable control strategies using state-of-the-art control design techniques and validation of the same with extensive experimental work.

The study of dynamic characteristics began with an effort to understand how stiffness characteristics of the system change with respect to disturbance characteristics and control voltage applied to the solenoid. This study led to the determination of two types of stiffness - static and dynamic - which need to be accounted for in the modeling of system.

Next, a nonlinear model of the pneumatic suspension system was derived and verified by the experimental study. The previous research work mainly focused on the modeling of an air spring under a specific operating condition like for a particular excitation with fully open or closed valve condition. Such analysis has its limitations because the real system always operates under different operating conditions which significantly affect the dynamical model of the system. The nonlinear model developed in this thesis can be used to describe system dynamics for multiple operating conditions. Towards this effort, two key parameters, K_{cr} and K_{amp}, were introduced to account for the effects of various excitation sources and orifice

voltages on the dynamic stiffness of the system. The K_{cr} and K_{amp} values were identified based on each test case, and the nonlinear model of the pneumatic suspension was finally built with the tuning parameters, and it was validated using the experimental tests. The linearization study and several case studies for different stiffnesses were performed.

Since controller synthesis techniques for nonlinear systems are not as developed as for linear case simplified linear models were obtained both by analytical derivation and system identification process. The analytical model parameters were tuned using system-id data.

Once the linear model with adequate fidelity was obtained two different control techniques were utilized to design controllers. These techniques were H-infinity and Sliding Mode control methodologies. The effective controller design was obtained by synthesizing hybrid controller which used strengths of both of these control techniques in a unified control scheme. The controller designs were implemented in simulation first and then onto real hardware. The benefits as well as limitations of controllers were assessed. The results were summarized via various response plots and tables.

The simulation as well as experimental results showed that the semi-active air spring-accumulator system offers great vibration isolation properties and is a viable suspension system for future. The dynamical behavior of the system is also understood better through this work and controller implementation demonstrated that advanced controller designs can be used for such system to exploit its inherent characteristics.

Future work should address the following:

(1) how the bandwidth limitations of the valve control system can be removed.

(2) how multiple air-springs can be used to increase controllability.

(3) how variable volume accumulator can be designed to give increased degree of freedom for control.

(4) how the bag force dynamics can be isolated using some kind of real-time compensation.

(5) how to quantify the stability margin of the parameter values used in the sliding mode control law.

In summary, the semi-active pneumatic suspensions of the type considered in.

APPENDIX A. Simulink Diagram for Nonlinear Model of the Pneumatic Suspension System

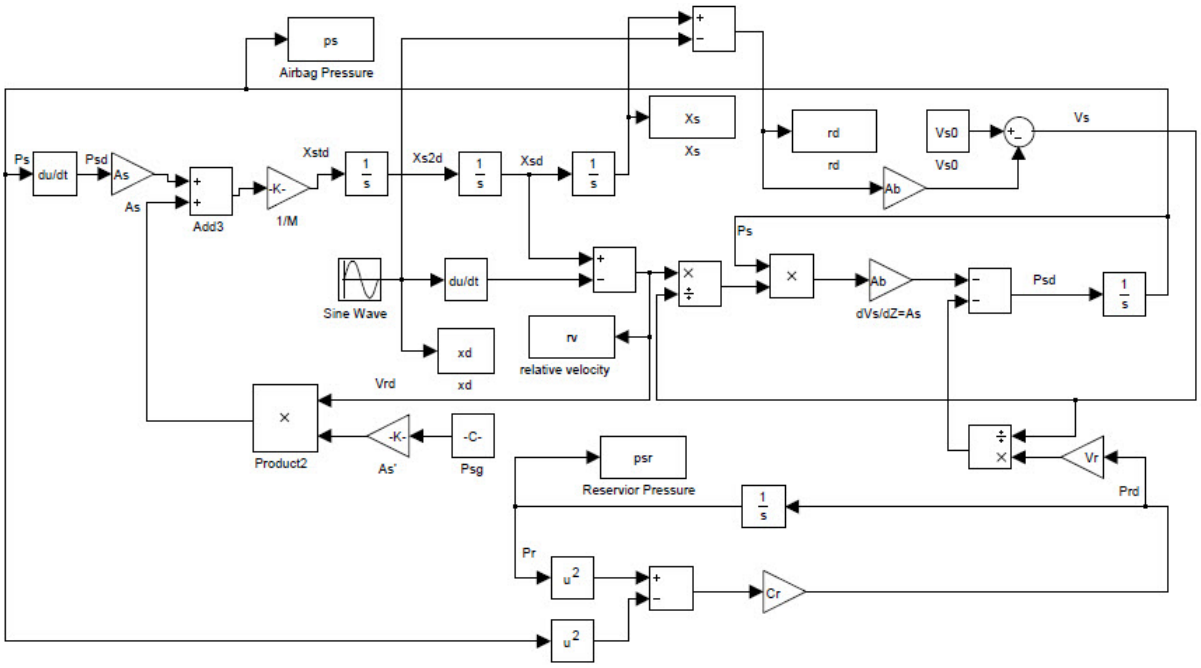

APPENDIX B. RMS Values of the Pneumatic Suspension System for Multiple Gds

	0.2 inch	0.3 inch	0.4 inch	0.5 inch	0.6 inch	0.7 inch
Excitation Input(case 1)	0.3881	0.3881	0.3881	0.3881	0.3881	0.3881
Closed-Loop Output(case 1)	0.2552	0.2455	0.2465	0.243	0.1829	0.19
Excitation Input(case 2)	0.3964	0.3964	0.3964	0.3964	0.3964	0.3964
Closed-Loop Output(case 2)	0.2012	0.2312	0.1803	0.1789	0.1782	0.178
Excitation Input(case 3)	0.404	0.404	0.404	0.404	0.404	0.404
Closed-Loop Output(case 3)	0.1979	0.1929	0.1922	0.1942	0.1946	0.1286
Excitation Input(case 4)	0.4315	0.4315	0.4315	0.4315	0.4315	0.4315
Closed-Loop Output(case 4)	0.1335	0.1209	0.1095	0.1092	0.1094	0.1093

APPENDIX C. Simulink Diagram of the Sliding Mode Reference Control

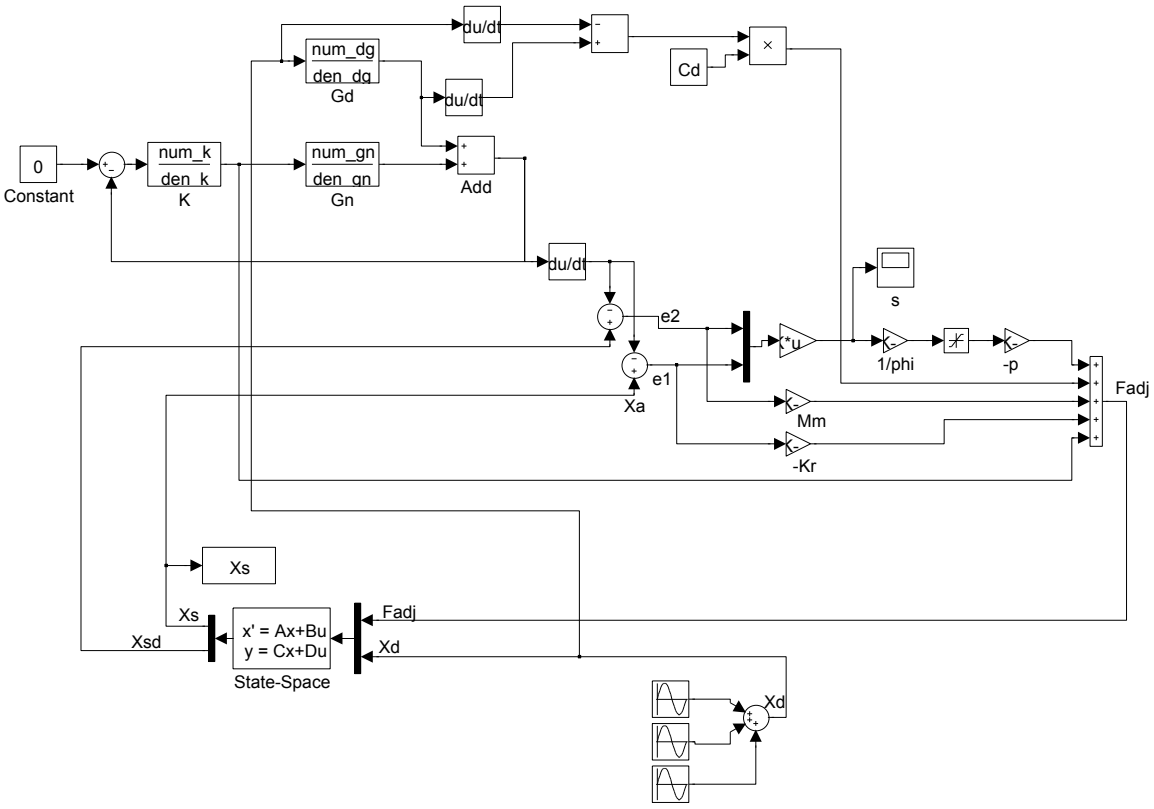

APPENDIX D. Summary of Fitting Functions: V = f(C)

Case Number	Excitation (Inch)	C (Ns/m)	V (Volt)	$V = f(C)$
1	0.2	679-1713	5-5.75	0.65e-3C + 4.6
1	0.3	489-1523	5-6	0.88e-3C + 4.6
1	0.4	753.4-1175	5.5-6.5	0.23e-2C + 3.8
1	0.5	989.4-1167	6-6.75	1.9e-5C^2 - 0.038C + 25
1	0.6	1221-1311	6-7	0.011C - 7.9
1	0.7	1227-1467	6.25-7	0.28e-2C + 2.9
2	0.2	930-1713	5.75-8	-4.2e-9C^3 + 2.1e-5C^2 - 0.035C + 26
2	0.3	886.2-1523	6-8	7.6e-6C^2 - 0.022C + 22
2	0.4	846.3-1175	6.5-8	-0.0045C + 12
2	0.5	990.2-1167	6.75-8	-0.0059C + 14
2	0.6	1232-1311	7-8	-0.0091C +18.85
2	0.7	1348-1467	7-8	-0.007C + 17

APPENDIX E. Simulink Diagram for Sliding Mode Reference H infinity Control:Part A

The simulink diagram for the sliding mode reference H infinity control can be divided into two parts: Part A: Control Law; Part B: Orifice Voltage Input. To have a good resolution for the control law. The simulink diagram for each part is presented separately.

Part A: Control Law

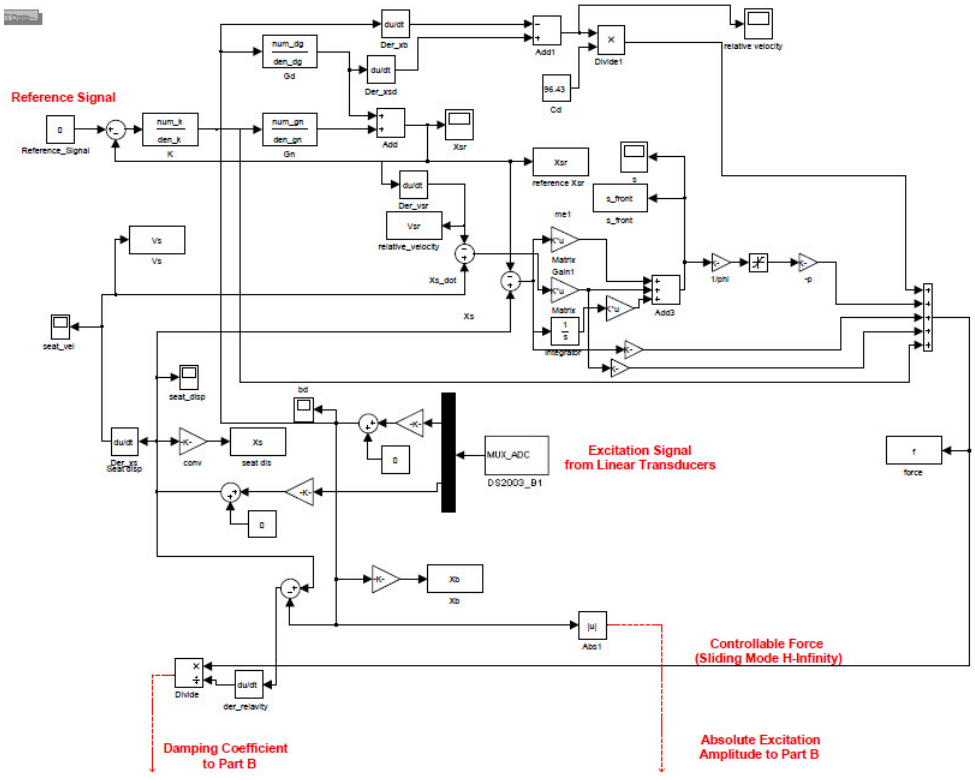

APPENDIX F. Simulink Diagram for Sliding Mode Reference H infinity Control: Part B

Part B: Orifice Voltage Input

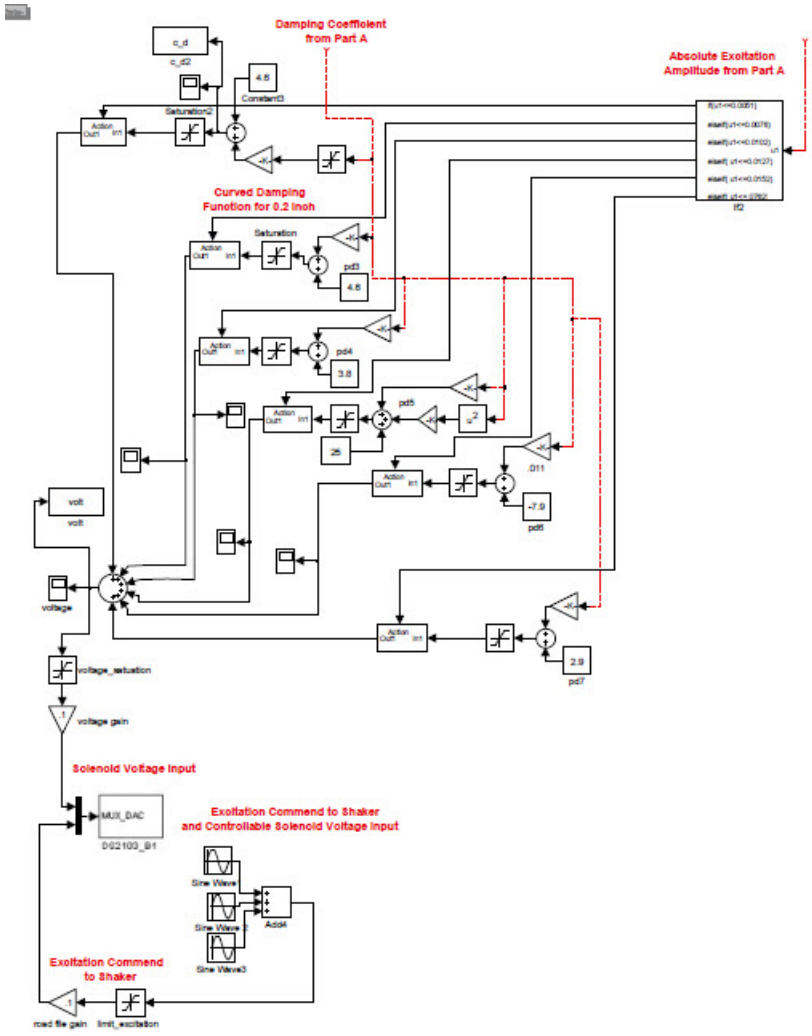

BIBLIOGRAPHY

[1] "http://en.wikipedia.org/wiki/Suspension(vehicle)"

[2] B. T. Fijalkowski, (2011). "Automotive mechatronics: operational and practical issues". Vol. 2, pp.257.

[3] "http://en.wikipedia.org/wiki/Leafspring".

[4] "http://www.motorera.com/history/hist08.html".

[5] Malin Presthus, (2002). "Derivation of air spring model parameters for train simulation". Master Thesis, Department of Applied Physics and Mechanical Engineering. Lulea University of Technology, Sweden, pp. 10.

[6] Lanchester FW, (1936). "Motor car suspension and independent springing". *Proc IMechE J Automobile Eng D1*, Vol. 30, pp. 668762.

[7] Margolis, D.L., (1982). "The response of active and semi-active suspensions to realistic feedback signals". *Vehicle System Dynamics*, Vol. 11, No. 3, pp. 267-282.

[8] R S Sharp, S A Hassan, (1986). "The relative performance capabilities of passive, active and semi-active Car suspension systems". *Proceedings of the Institution of Mechanical Engineers, Part D: Journal of Automobile Engineering*, Vol. 200, No. 3, pp. 219-228.

[9] J S Tang, (1996). "Passive and semi-active airspring suspensions for rail passenger vehicles - theory and practice". *Proceedings of the Institution of Mechanical Engineers, Part F: Journal of Rail and Rapid Transit*, Vol. 210, pp. 103-117.

[10] P. De Man, P.Lemerle, and etc., (2005). " An investigation of a semi-active suspension for a fork lift truck ". *Vehicle System Dynamics*, Vol. 43, No. 2, pp. 107-119.

[11] Federspiel-Labrosse, G.M., (1954). "Contribution a letude et au perfectionement de la suspension des vehicules". *J. de la SIA*, FISITA, pp. 427-436.

[12] Hedrick J.K., Wormely D.N. (1975). "Active suspension for ground support vehicles – a state-of-the-art review". *ASME-AMD*, Vol. 15 , pp. 21-40.

[13] Crolla, D.A. (1995). "Vehicle dynamics-theory into practice". *Proc. IMechE, Part D: Journal of Automobile Engineering*, Vol. 210, No.2, pp. 83-94.

[14] Bender, E.K., (1968). "Some fundamental limitations of active and passive suspension system". SAE Paper, Number: 680750

[15] Richer, E., and Hurmuzlu, Y., (2001). "A high performance pneumatic force actuator system part 1 -nonlinear mathematical model". *Journal of Dynamics Systems Measurement and Control*, Vol. 122 (3), pp. 416-425.

[16] Richer, E., and Hurmuzlu, Y., (2001). "A high performance pneumatic force actuator system part 2 -nonlinear controller design". *Journal of Dynamics Systems Measurement and Control*, Vol. 122 (3), pp. 426-434.

[17] Fialho, I.J. and Balas, G.J., (2000). "Design of nonlinear controllers for active vehicle suspensions using parameter-varying control synthesis". *Vehicle System Dynamics*, Vol. 33, pp.351-370.

[18] Hedrick, J.K., Rajamani, R., (2007). "Performance of active automotive suspensions with hydraulic actuators: theorey and experiment". *Proceedings of American Control Conference*, Vol. 14, pp.254-270.

[19] Anakwa, W. Jones, T., and etc., (2002). "Development and control of a prototype pneumatic active suspension system". *QIEEE Transactions on Education*, Vol. 45, No.1, pp.43-49.

[20] Smaoui,M., Brun, X. and Thomasset, D., (2008). "High-order sliding mode for an electropneumatic system: A robust differentiator-controller design". *International journal of robust and nonlinear control*, Vol. 18, pp.481-501.

[21] Toyama, S., Ikeda, F., and Sorimachi, Y., (2008). "A second-order sliding mode controller for active suspension system". *International conference on control,automation and systems*, pp.18-23.

[22] Lauwerys, C., Swevers, J., and Sas, P., (2004). "Robust linear control of an active suspension on a quarter car test-rig". *Control Engineering Practice*, Vol.13, pp.577-586.

[23] Yoshimura, T., Kume, A., Kurimoto, M. and Hino, J., (2001). "Construction of an active suspension system of a quarter car model using the concept of sliding mode control". *Journal of Sound and Vibration*, Vol.239, (2), pp.187-199.

[24] Kim, C. and Ro, P.I., (1998). "A sliding mode controller for vehicle active suspension systems with non-linearities". *Proceedings of the Institution of Mechanical Engineers, Part D: Journal of Automobile Engineering*, Vol.212, pp.79-92.

[25] Williams, R. A., (1994). "Electronically controlled automotive suspensions". *Computing and Control Egineering Journal*, Vol.5, No. 3, pp. 143-148.

[26] Shahriar, S., (2009). "Development and evaluation of a semi-active suspension system for full suspension tractors". PhD dissertation, Department of mechanical engineering, Berlin Institute of Technology.

[27] Crosby, M.J. and Karnopp, D.C. (1973). "The active damper-a new concept for shock and vibration control". *The Shock and Vibration Bulletin*, No.43, part 4, pp. 119-133.

[28] Yokoyama, M., Hedrick, J.K., and Toyama, (2001). "A model following sliding mode controller for semi-active suspension systems with MR dampers". *Proceedings of the American Control Conference*, pp.2652-2657.

[29] Bolandhemmat, H., Clark, C.M., and Golnaraghi, F., (2008). "Toward systematic approaches to design and implement vehicles semi-active control systems". *Industrial Electronics, IEEE International Symposium on* , pp.817-822.

[30] Henry, R.R. and Zeid,A.A., (1992). "A nonlinear, sub-optimal, observer-based control for semi-active suspension", *Proceedings of Transportation Systems.* Vol.44, pp.181-189.

[31] Ahmadian, M., Song, X., and Southward, S., (2004). "No-jerk skyhook control methods for semiactive suspensions", *Journal of vibration and acoustics*. Vol. 126, pp.581-584.

[32] Miller, L., (1988). "Tuning passive, semi-active, and fully active suspension systems". *Proceedings of the 27th IEEE Conference on Decision and Control*, Vol. 3, pp.2047 - 2053.

[33] Margolis, D., Nobles, C. M. (1991). "Semi-active heave and roll control for large off-road vehicles". *SAE Special Publications*, No. 892, pp. 25-34.

[34] Karnopp, D., Crosby, M. J., Harwood, R. A. (1974). "Vibration control using semi-active force generators". *ASME Journal of Engineering for Industry*, Vol. 96 (2), pp.619-626.

[35] Hong, K-S,Sohn, H-C, and Hedrick, J.K., (2002). "Modified skyhook control of semi-active suspensions: a new model,gain scheduling, and hardware-in-the-loop tuning". *Journal of Dynamic Systems,Measurement, and Control*, Vol. 124(1), pp.128-137.

[36] Song, X., Ahmadian, M. and etc, (2005). "An adaptive semiactive control algorithm for magnetorheological suspension systems". *Journal of vibration and acoustics*, Vol.127, pp.493-502.

[37] Kawabe, T., Isobe, O., and etc., (1998). "New semi-active suspension controller design using quasi linearization and frequency shaping". *Control Engineering Practice*, Vol.6, pp.1183-1191.

[38] Dixit,R.K. and Buckner, G.D., (2005). "Sliding mode observation and control for semiactive vehicle suspensions". *Vehicle System Dynamics*, Vol.43, pp.83-105.

[39] Niteo, A.J., Morales, A.L., Gonzalez, A., Chicharro, J.M., and Pintado, P., (2008). "An analytical model of pneumatic suspensions based on an experimental characterization". *Journal of Sound and Vibration*, Vol. 313, (1-2), pp. 290-307.

[40] Erin, C., Wilson, B. ,and Zapfe, J., (1998). "An improved model of a pneumatic vibration isolator: theory and experiment". *Journal of Sound and Vibration*, Vol. 218, (1), pp. 81-101.

[41] Berg., M., (1999). "A three-dimensional airspring model with friction and orifice damping". *Vehicle System Dynamics Supplement*, Vol.33, pp. 528-539.

[42] Chang, C. and Lu, Z.-H., (2008). "Dynamic model of an air spring and integration into a vehicle dynamics model". *Proceedings of the Institution of Mechanical Engineers, Part D: Journal of Automobile Engineering*, Vol. 222 (10), pp. 1813-1825.

[43] Deo, H. and Suh, N., (2006). "Pneumatic suspension system with independent control of damping, stiffness and ride-height". *Proceedings of ICAD 2006 4th International Conference of Axiomatic Design*, Vol. 22.

[44] Berg, M., (1998). "A non-linear rubber spring model for rail vehicle dynamics analysis". *Vehicle System Dynamics*, Vol. 30, pp. 197-212.

[45] Sayyaadi, H., and Shokouhi, N., (2009). "Improvement of passengers ride comfort in rail vehicles equipped with air springs". *World Academy of Science, Engineering and Technology*, Vol. 53, pp. 827-833.

[46] Fox, M.N., Roebuck, R.L. and Cebon, D., (2007). "Modelling rolling-lobe air springs". *International Journal of Heavy Vehicle Systems*, Vol. 14, pp. 254-270.

[47] Quaglia, G. and Guala, A., (2003). "Evaluation and validation of an air spring analytical model". *International Journal of Fluid Power*, Vol.4, No.2, pp. 43-54.

[48] Henderson, R.J., and Raine, J.K., (1998). "A two-degree-of-freedom ambulance stretcher suspension. Part 2: simulation of system performance with capillary and orifice pneumatic damping". *Proceedings of the Institution of Mechanical Engineers, Part D: Journal of Automobile Engineering*, (212)(n3D3), pp. 227-240.

[49] Popov, G. and Sankar, S., (1995). "Modelling and analysis of non-linear orifice type damping in vibration isolators". *Journal of Sound and Vibration*, Vol. 183, (5), pp. 751-764.

[50] Vaughan, N.D. and Gamble, J.B., (1996). "The modeling and simulation of a proportional solenoid valve". *Journal of Dynamic Systems,Measurements and Control*, Vol. 118, (1), pp. 120-125.

[51] Callen, H., (1985). " Thermodynamics and an introduction to thermostatistics ", Second Edition, p. 461.

[52] "http://en.wikipedia.org/wiki/Hagen".

[53] Shames, I., (1982). "Mechanics of fluids".

[54] (2004), "Mechanical vibration and shock – evaluation of human exposure to whole-body vibration – part 5: method for evaluation of vibration containing multiple shocks", ISO 2631-5.

[55] Skogestad, S and Postlethwaite, I, (2005). "Multivariable feedback control analysis and design (2nd edition)".

[56] Slotine, J and Li, W, (1991). "Applied nonlinear control".

[57] Christopher Edwards and Sarah K. Spurgeon, (1998). "Sliding Mode Control: Theorey and Applications".